

Optimisation of a-Si:H/ μ c-Si:H Tandem Solar Cell on Flexible Al Substrates

Use of Modelling for Cell Design
and Performance Predictions

E.M. Spaans



Optimisation of a-Si:H/ μ c-Si:H Tandem Solar Cell on Flexible Al Substrates

Use of Modelling for Cell Design and
Performance Predictions

by

E.M. Spaans

to obtain the degree
of Master of Science in Applied Physics
at the Delft University of Technology,
to be defended publicly on Wednesday June 10, 2020 at 9:00 AM.

Student number: 4429710
Thesis committee: Prof. Dr. A.H.M. Smets, TU Delft, PVMD supervisor
Dr. A.J. Houtepen, TU Delft, Applied Sciences supervisor
Dr. R. Santbergen, TU Delft, external supervisor
Dr. G. Limodio, TU Delft, daily supervisor

Cover image by Solar Magazine, December 2019 edition.
An electronic version of this thesis is available at <http://repository.tudelft.nl/>.

Abstract

The future of our energy supply cannot continue to depend on the use of exhaustible fossil fuels. The successful transition to a society powered by renewable energy sources is one of the major challenges our current generation faces. Renewable systems will only fully establish themselves if high conversion efficiencies can be obtained at a reasonable cost, in order to compete with conventional, carbon-based sources. With this in mind, photovoltaic solar energy can be a promising solution.

This study focuses on the investigation of the potential efficiency of a thin-film tandem solar cell, combining amorphous silicon and microcrystalline silicon for a high performance device. With the use of flexible, light substrates, inexpensive modules can be manufactured in a roll-to-roll configuration to produce high efficiency products for a large scale implementation in society. The semiconductor modelling software ASA was used to optimise the structure of the tandem, identifying the absorber layer thicknesses that maximise the efficiency. Moreover, the impact of possible optical variations in the design of the device on the performance were analysed.

To start, model parameters of single-junction amorphous silicon and microcrystalline silicon cells were calibrated to recreate the performance of such devices based on experimental data. By conducting a sensitivity analysis of the model parameters, this was effectively achieved. The single-junction models were combined in a tandem structure to forecast the operation of the multi-junction device.

It was found that the performance of the tandem was highly sensitive to the choice of refractive indices of the layers at the junction between the two subcells. A high mismatch between the refractive indices of these layers and the absorber layers of the subcells results in an increased reflection of light to the top cell. This is beneficial for the current production of this subcell, but is too detrimental for the operation of the bottom cell. By bringing the refractive indices closer together, an efficiency of 13.0 % was predicted. The inclusion of an encapsulation at the front of the cell boosts this efficiency to 13.7 %, at a top/bottom absorber layer thickness combination of 160 nm/0.6 μm .

The possibilities of enhancing the efficiency with an intermediate reflector were examined. The optical conditions for the ideal light distribution with such a reflector were computed to provide estimations of the potential increase in performance. For the best performing device, an increase of the initial efficiency of 13.0 % to 13.2 % was foreseen, at slightly thinner top cells and similar bottom cell thicknesses.

All in all, the predicted efficiencies of the amorphous silicon/microcrystalline silicon tandem solar cell evidences the potential of these devices for the production of cheap, highly efficient modules. The developed analysis of the ideal intermediate reflector can be generalised to other multi-junction solar cells to establish the potential efficiency increase such a layer brings along. This can help in the decision of whether the increase in performance justifies the added manufacturing complexity and costs.

Contents

Abstract	iii
List of Figures	vii
List of Tables	xi
Nomenclature	xiii
1 Introduction	1
1.1 PV in the energy transition	2
1.2 FlamingoPV	3
1.3 Thesis objectives and outline	3
2 Fundamentals	5
2.1 Working principle of a solar cell	5
2.1.1 Optics	6
2.1.2 Semiconductors	9
2.1.3 Layer build-up of a solar cell	12
2.1.4 Solar cell performance	14
2.1.5 Limitations	17
2.2 Thin-film silicon devices	19
2.2.1 Amorphous silicon	19
2.2.2 Microcrystalline silicon	21
2.2.3 $\mu\text{c-Si:H}$ vs a-Si:H	22
2.3 Tandem devices	23
2.3.1 Micromorph cell	24
3 Experimental details: device fabrication and characterisation	27
3.1 Deposition techniques	27
3.1.1 Plasma-Enhanced Chemical Vapour Deposition	27
3.1.2 Magnetron sputtering	29
3.1.3 Evaporation	29
3.2 Device fabrication	29
3.2.1 HyET Solar's R2R processing	29
3.2.2 Lab-scale processing	30
3.3 Characterisation techniques	33
3.3.1 Material characterisation: Raman spectroscopy	33
3.3.2 Performance characterisation: I-V characteristic and EQE	34

4 Thin-film modelling: ASA	37
4.1 Introduction	37
4.2 Description of the model	38
4.2.1 Optical modelling	38
4.2.2 Electrical modelling	38
4.3 Sample simulation and input file	41
4.4 Automating ASA: autASA	44
4.4.1 Directory structure	44
4.4.2 Code execution flowchart	45
4.4.3 Example: variation of the effective density of states	47
4.5 Sensitivity analysis	49
4.6 Calibration of the model	53
4.6.1 Validation of HyET a-Si:H single-junction solar cell	53
4.6.2 Validation of $\mu\text{c-Si:H}$ single-junction solar cell	58
5 Performance optimisation of micromorph cell using ASA	65
5.1 a-Si:H/ $\mu\text{c-Si:H}$ tandem model in ASA	65
5.1.1 Simulation structure	65
5.1.2 Device performance	66
5.1.3 Section appendix: simulation of each subcell's J_{sc}	69
5.2 Optical considerations at the TRJ layers	70
5.2.1 Sensitivity analysis of refractive indices	70
5.2.2 Intermediate reflector	76
5.3 Region of interest for micromorph R2R production	82
5.3.1 Texturing comparison	82
5.3.2 Encapsulated cell performance prediction	84
5.4 Further optical improvements	87
6 Preliminary experimental results	89
6.1 Amorphous silicon depositions	89
6.1.1 Raman spectra	89
6.1.2 Dark $I-V$ measurements	90
6.2 Multi-junction depositions	91
7 Conclusions and outlooks	93
7.1 Conclusions	93
7.2 Outlooks	94
Acknowledgements	97
A ASA .cas files	99
A.1 Reference	99
A.2 Calibrated a-Si:H cell	101
A.3 Calibrated $\mu\text{c-Si:H}$ cell	102
B ASA web automation code: autASA.py	105
C ASA parameter sensitivity	111

D Simulations: complex refractive indices	115
D.1 a-Si:H cell	115
D.2 μ c-Si:H cell	115
E EQE artefacts	117
F Texture comparison: micromorph cell performance parameters	119
Bibliography	121

List of Figures

1.1	Comparison of the worldwide energy consumption by source of the years 2000 and 2018. Data from [6].	2
2.1	Working principle of a solar cell. The painted areas represent possible states.	6
2.2	AM1.5 solar spectrum [17]. The conversion for the top x -axis is given by Equation (2.1), in units of <i>electronvolt</i> (eV).	7
2.3	Absorption coefficients of some materials used in PV. Adapted from [18].	8
2.4	Dispersion relation for a) direct and b) indirect band gap materials. Inspired by [8].	9
2.5	Visualisation of the reflection and transmission of a wave reaching the interface between two different media 1 and 2 and the relevant parameters.	9
2.6	2D representation of the structure of c-Si.	10
2.7	2D representation of the doping procedure in c-Si where a) a donor atom is introduced and b) an acceptor atom is introduced. Inspired by [15].	11
2.8	Top view of a pn junction. Inspired by [8].	11
2.9	Thermal equilibrium band diagrams of a pn junction a) before contact and b) after contact. Inspired by [15].	12
2.10	Sample structure of an a-Si solar cell. The layer thicknesses are not to scale.	13
2.11	Equivalent circuit model of a solar cell. Inspired by [8].	15
2.12	Sample $I - V$ and $P - V$ curve of a solar cell under illumination.	15
2.13	Sample EQE curve of a solar cell.	16
2.14	2D representation of the atomic structure of a-Si:H.	20
2.15	Density of electronic states N of a-Si:H as a function of energy E . DB: dangling bonds, VB: valence band, CB: conduction band. Inspired by [24].	20
2.16	Structural composition of $\mu\text{c-Si}$. Inspired by [44].	21
2.17	Absorption coefficients of a-Si:H and $\mu\text{c-Si:H}$. Adapted from [42].	23
2.18	Sample structure of a micromorph solar cell. ARC: anti-reflection coating, TCO: transparent conductive oxide, IR: intermediate reflector. The layer thicknesses are not to scale.	25
2.19	Illustration of the reflection and transmission of light a) without an IR and b) with an IR at a junction between materials A and B.	26
3.1	Sample AFM scan of a textured Al foil.	31
3.2	Raman spectra of crystalline, microcrystalline and amorphous silicon layers. The spectra are normalised such that the area under each curve is the same.	34
4.1	Simulation structure used as reference for the modelling of a-Si:H. The layer thicknesses are not to scale.	42

4.2	$J - V$ curve of the simulation of the reference a-Si:H cell.	42
4.3	EQE curve of the simulation of the reference a-Si:H cell.	43
4.4	Absorption per layer and total reflection as a function of photon wavelength of the simulation of the reference a-Si:H cell. The colours are the same for each layer in the structure of the cell in Figure 4.1.	44
4.5	Directory tree and necessary files to run autASA.	45
4.6	Flowchart of the automation routine implemented in <i>autASA.py</i>	46
4.7	$J - V$ curves of the simulations where N_C was varied for the intrinsic a-Si:H layer. The legend indicates the changed parameter in units of m^{-3}	48
4.8	EQE curves of the simulations where N_C was varied for the intrinsic a-Si:H layer. The legend indicates the changed parameter in units of m^{-3}	48
4.9	Simulation structure of an a-Si:H solar cell produced at HyET. The layer thicknesses are not to scale.	53
4.10	Typical performance of a HyET flexible cell and results of the default ASA simulation: a) $J - V$ curve and b) EQE.	54
4.11	Results of the band gap adjustment with respect to the reference ASA simulation.	55
4.12	Results of the V_{oc} adjustment with respect to ‘Change 1’.	55
4.13	Results of the EQE blue response adjustment with respect to ‘Change 2’.	56
4.14	Results of the FF adjustment with respect to ‘Change 3’.	56
4.15	Results of the J_{sc} adjustment with respect to ‘Change 4’.	57
4.16	Final results of the model calibration of the HyET a-Si:H cell.	57
4.17	Simulation structure of a μc -Si:H solar cell from [76]. The layer thicknesses are not to scale.	59
4.18	Results of the default ASA μc -Si:H simulation and the calibration goal from a cell in H. Tan et al [76]: a) $J - V$ curve and b) EQE. No target $J - V$ curve was provided.	60
4.19	Results of the V_{oc} adjustment with respect to the default simulation file in ASA.	60
4.20	Results of the FF adjustment with respect to ‘Change 1’.	61
4.21	Results of the J_{sc} adjustment with respect to ‘Change 2’.	61
4.22	Final results of the model calibration of the μc -Si:H cell.	62
5.1	Structure used for the simulation of a micromorph solar cell in ASA. The layer thicknesses are not to scale.	66
5.2	Simulated micromorph solar cell parameters for different absorber layer thicknesses of the calibrated a-Si:H and μc -Si:H single-junction cells.	67
5.3	Short-circuit current difference between the a-Si:H and μc -Si:H cell in a micromorph device ($\Delta J_{sc} = J_{sc,\mu c-Si} - J_{sc,a-Si}$) for different absorber layer thickness combinations.	68
5.4	Refractive indices n of the layers around the junction between the top and bottom cell. The order of the labels in the legend matches the order of the layers the incoming light passes through.	69
5.5	Short-circuit current densities of simulations of a micromorph cell and the currents delivered by each subcell as a function of the thickness of the top cell, with a constant bottom cell thickness of $1 \mu m$. The subcells’ J_{sc} was computed by only modelling the desired cell electrically.	70

5.6	Refractive indices n of the layers around the junction between the top and bottom cell of scenario 2. The order of the first four labels in the legend matches the order of the layers the incoming light passes through. The dashed line indicates the previously assigned refractive index values of the p -doped layer of the bottom cell.	71
5.7	Simulated micromorph solar cell parameters for different absorber layer thicknesses for scenario 2.	72
5.8	Short-circuit current difference for scenario 2 between the a-Si:H and $\mu\text{c-Si:H}$ cell in a micromorph device ($\Delta J_{\text{sc}} = J_{\text{sc},\mu\text{c-Si}} - J_{\text{sc},\text{a-Si}}$) for different absorber layer thickness combinations.	73
5.9	Refractive indices n of the layers around the junction between the top and bottom cell of scenario 3. The order of the first four labels in the legend matches the order of the layers the incoming light passes through. The dashed line indicates the previously assigned refractive index values of the n -doped layer of the top cell.	74
5.10	Simulated micromorph solar cell parameters for different absorber layer thicknesses for scenario 3.	75
5.11	Short-circuit current difference for scenario 3 between the a-Si:H and $\mu\text{c-Si:H}$ cell in a micromorph device ($\Delta J_{\text{sc}} = J_{\text{sc},\mu\text{c-Si}} - J_{\text{sc},\text{a-Si}}$) for different absorber layer thickness combinations.	76
5.12	Illustration of the inclusion of an IR at the TRJ of a micromorph device.	76
5.13	Angular intensity distribution of light used to account for the different incidence angles at the IR.	77
5.14	Reflectance as a function of the complex refractive index for two wavelengths. n_1, κ_1, n_3 and κ_3 are taken from scenario 2.	78
5.15	Complex refractive index values of the intermediate reflector that maximise the reflectance and transmittance as a function of wavelength. The refractive index data of the adjacent layers are plotted as a reference. The step-like behaviour is a consequence of the discretisation of the domains.	79
5.16	Refractive indices of an ideal IR with $\lambda_t = 500$ nm and the two layers conforming the TRJ. A finer discretisation of the n and κ domains was done to obtain a more continuous curve.	79
5.17	Short-circuit currents of a micromorph device in scenario 2 with different choices of IR.	80
5.18	Maximum efficiency in the simulated thickness range with the use of different ideal IRs as a function of λ_t . The dashed line represents the maximum efficiency when no IR is used in each scenario.	81
5.19	Absorptance profiles of the subcells in a micromorph device for different interface textures. Top/bottom cell thicknesses: 200 nm/1 μm	83
5.20	Comparison of the efficiencies as a function of the subcell thicknesses for the baseline texturing at HyET and the developed texture for FlamingoPV.	84
5.21	Structure of the front encapsulation used by HyET Solar. The layer thicknesses are not to scale.	84
5.22	Simulated encapsulated micromorph solar cell parameters for different absorber layer thicknesses.	85

5.23	Absorptance profiles (continuous lines) of the subcells in a micromorph device and total reflectance (dashed lines) for different interface textures. Top/bottom cell thickness: 200 nm/1 μm	86
5.24	A more realistic prediction of the efficiency of the encapsulated cell after considering lower short-circuit currents of the subcells.	86
5.25	Absorptance profiles (continuous lines) of the subcells in a micromorph device and total reflectance (dashed lines) for an ideal encapsulation with Ag as back reflector and the encapsulation used at HyET with AZO/Al as back reflector. Top/bottom cell thickness: 200 nm/1 μm	87
5.26	Efficiency prediction of a micromorph cell with an ideal encapsulation and Ag as back reflector.	88
6.1	Raman spectra of intrinsic a-Si:H with thicknesses of 250 nm and 500 nm. The vertical dotted line is placed at a Raman shift of 480 cm^{-1}	90
6.2	Dark $I - V$ characteristic of three <i>pin</i> a-Si:H cells.	90
6.3	Comparison of the measured shunt resistance of a-Si:H cells produced at HyET Solar and at Delft on a textured Al substrate.	91
6.4	SEM cross-section image of a micromorph tandem deposited on a textured Al foil substrate, taken by G. Limodio.	92
6.5	SEM cross-section image of an a-Si:H/ μc -Si:H/ μc -Si:H triple-junction deposited on a textured Al foil substrate, taken by G. Limodio.	92
D.1	Complex refractive indices of the materials used in the simulations of a-Si:H.	115
D.2	Complex refractive indices of the materials used in the simulations of μc -Si:H. The absorption index of glass is 0 over the full spectrum.	116
E.1	Simulated EQE of the a-Si:H cell in a micromorph device, measured with different fluxes of the 800 nm bias light. The legend indicates the photon flux density in units of $\text{m}^{-2}\text{s}^{-1}$	117
E.2	Failure of a simulated EQE of the a-Si:H cell in a micromorph device, measured with different fluxes of the 800 nm bias light. The legend indicates the photon flux density in units of $\text{m}^{-2}\text{s}^{-1}$	118
F.1	Comparison of the short-circuit currents as a function of the subcell thicknesses for the baseline texturing at HyET and the developed texture for FlamingoPV.	119
F.2	Comparison of the open-circuit voltages as a function of the subcell thicknesses for the baseline texturing at HyET and the developed texture for FlamingoPV.	120
F.3	Comparison of the fill factors as a function of the subcell thicknesses for the baseline texturing at HyET and the developed texture for FlamingoPV.	120

List of Tables

3.1	Summary of the deposition conditions of the layers used in the fabrication of a-Si:H and $\mu\text{c-Si:H}$ cells. The values are taken from the standard recipes defined for the AMIGO cluster tool. *: 2 % in H_2 . **:200 ppm in H_2	32
4.1	Performance parameters of the reference a-Si:H pin simulation.	43
4.2	Reference symbols used in Table 4.3 to indicate the degree to which the variation of a model parameter impacts the performance indicators of the solar cell.	50
4.3	Symbolic results of the sensitivity of the open-circuit voltage V_{oc} , short-circuit current density J_{sc} , fill factor FF , efficiency η , EQE for the range 300 nm to 550 nm (labelled as EQE_1) and for 550 nm to 800 nm (labelled as EQE_2) to the variation of model parameters in ASA simulations. The abbreviations are described in Nomenclature.	50
4.4	Performance parameters V_{oc} , J_{sc} , FF and η of a typical a-Si:H flexible solar cell produced by HyET Solar, along with the values of the default ASA simulation file.	54
4.5	Results of the model calibration of HyET's a-Si:H cell.	58
4.6	Overview of the changes of model parameters with respect to the default ASA simulation file to match the solar cell performance of a typical a-Si:H cell from HyET.	58
4.7	Performance parameters V_{oc} , J_{sc} , FF and η of the calibration goal of a cell described by H. Tan [76], along with the values of the default ASA simulation file.	59
4.8	Results of the model calibration of a $\mu\text{c-Si:H}$ cell from H. Tan et al [76].	62
4.9	Overview of the changes of model parameters with respect to the default ASA simulation file to match the solar cell performance of the $\mu\text{c-Si:H}$ cell.	63
5.1	Micromorph efficiency at a top/bottom cell thickness combination of 200 nm/2 μm for the considered scenarios.	74
5.2	Thicknesses at which the maximum efficiency for difference scenarios is obtained, considering different ideal IRs.	81
5.3	Parameters describing the baseline texturing at HyET and one developed within the FlamingoPV project.	82

C.1	Numerical results of the sensitivity of the open-circuit voltage V_{oc} , short-circuit current density J_{sc} , fill factor FF , efficiency η , EQE for the range 300 nm to 550 nm (labelled as EQE_1) and for 550 nm to 800 nm (labelled as EQE_2) to the variation of model parameters in ASA simulations. The abbreviations are described in Nomenclature.	111
-----	---	-----

Nomenclature

Symbol	Definition	Unit
D_n	electron diffusion coefficient	cm^2s^{-1}
D_p	hole diffusion coefficient	cm^2s^{-1}
E_g	band gap energy	eV
FF	fill factor	-
G_{opt}	optical generation rate	$\text{cm}^{-3}\text{s}^{-1}$
I_0	reverse bias saturation current	A
I_{MPP}	current at maximum power point	A
I_{ph}	photogenerated current	A
I_{sc}	short-circuit current	A
J_n	electron current density	$\text{Ccm}^{-2}\text{s}^{-1}$
J_p	hole current density	$\text{Ccm}^{-2}\text{s}^{-1}$
J_{sc}	short-circuit current density	Am^{-2}
N_C	effective density of states at the conduction band edge	cm^{-3}
N_V	effective density of states at the valence band edge	cm^{-3}
N_a	concentration of acceptor atoms	m^{-3}
N_a^i	concentration of free, ionised acceptor atoms	cm^{-3}
N_d	concentration of donor atoms	m^{-3}
N_d^i	concentration of free, ionised donor atoms	cm^{-3}
R	reflectance	-
R_{net}	net recombination-generation rate	$\text{cm}^{-3}\text{s}^{-1}$
R_{sh}	shunt resistance	Ω
R_s	series resistance	Ω
T	transmittance	-
T	temperature	K
V_{MPP}	voltage at maximum power point	V
V_{oc}	open-circuit voltage	V
X_c	crystalline fraction	-
χ	electron affinity	eV
ϵ	permittivity	$\text{CV}^{-1}\text{cm}^{-1}$
η	efficiency	%
κ	imaginary part of the complex index of refraction	-
λ	wavelength	m
λ_t	transition wavelength	m
μ_n	electron mobility	$\text{cm}^2\text{V}^{-1}\text{s}^{-1}$
μ_p	hole mobility	$\text{cm}^2\text{V}^{-1}\text{s}^{-1}$
ϕ	electric potential	V
ρ	space charge density	Ccm^{-3}
θ_1	incidence angle	$^\circ$

Symbol	Definition	Unit
θ_2	transmitted angle	°
\tilde{n}	complex index of refraction	-
d	thickness	m
n	free electron concentration	cm ⁻³
n	real part of the complex index of refraction	-
n_{loc}	concentration of localised electrons	cm ⁻³
p	free hole concentration	cm ⁻³
p_{loc}	concentration of localised holes	cm ⁻³
q	elementary charge	C
x_n	width of the depletion layer at the n -doped side of a pn junction	m
x_p	width of the depletion layer at the p -doped side of a pn junction	m
α	absorption coefficient	cm ⁻¹
$\mu\text{c-Si:H}$	hydrogenated microcrystalline silicon	
$\mu\text{c-Si:H(i)}$	intrinsic hydrogenated microcrystalline silicon	
$\mu\text{c-Si:H(n)}$	n -doped hydrogenated microcrystalline silicon	
$\mu\text{c-Si:H(p)}$	p -doped hydrogenated microcrystalline silicon	
a-Si:H	hydrogenated amorphous silicon	
a-Si:H(i)	intrinsic hydrogenated amorphous silicon	
a-Si:H(n)	n -doped hydrogenated amorphous silicon	
a-Si:H(p)	p -doped hydrogenated amorphous silicon	
ADF	Angular Distribution Function	
AFM	Atomic Force Microscopy	
AID	Angular Intensity Distribution	
APCVD	Atmospheric Pressure Chemical Vapour Deposition	
ARC	Anti-Reflection Coating	
ASA	Advanced Semiconductor Analysis	
autASA	automated ASA	
AZO	Aluminium-doped Zinc Oxide	
BIPV	Building-Integrated Photovoltaics	
c-Si	crystalline silicon	
c.neg	ASA parameter: hole capture rate in negatively charged tail states of the conduction band	m ³ s ⁻¹
c.neut	ASA parameter: electron (hole) capture rate in neutral tail states of the conduction (valence) band	m ³ s ⁻¹
c.pos	ASA parameter: electron capture rate in positively charged tail states of the valence band	m ³ s ⁻¹
ce.neut	ASA parameter: electron capture rate of neutral dangling bonds	m ³ s ⁻¹
ce.pos	ASA parameter: electron capture rate of positively charged dangling bonds	m ³ s ⁻¹
ch.neg	ASA parameter: hole capture rate of negatively charged dangling bonds	m ³ s ⁻¹
ch.neut	ASA parameter: hole capture rate of neutral dangling bonds	m ³ s ⁻¹
CVD	Chemical Vapour Deposition	
DOS	density of states	

Symbol	Definition	Unit
e.char	ASA parameter: characteristic energy that defines the exponential slope of the conduction or valence band tail	eV
e.range	ASA parameter: length of the conduction/valence band tail	eV
EQE	External Quantum Efficiency	
ETFE	Ethylene Tetrafluoroethylene	
ETL	Electron Transport Layer	
FlamingoPV	Flexible Lightweight Advanced Materials In Next Generation Of PV	
FTO	Fluorine-doped Tin Oxide	
HTL	Hole Transport Layer	
HyET	High yield Energy Technologies	
IR	Intermediate Reflector	
ITO	Indium Tin Oxide	
LCOE	Levelized Cost of Electricity	
MPP	Maximum Power Point	
MST	Modulated Surface Texture	
n	ASA parameter: concentration of dangling bonds	m^{-3}
n.emob	ASA parameter: density of states at the conduction or valence band edge	$m^{-3}eV^{-1}$
PECVD	Plasma-Enhanced Chemical Vapour Deposition	
PV	Photovoltaics	
PVD	Physical Vapour Deposition	
PVMD	Photovoltaic Materials and Devices	
R2R	Roll-To-Roll	
RF	Radio-Frequency	
SEM	Scanning Electron Microscope	
STC	Standard Test Conditions	
SWE	Staebler-Wronski Effect	
TCO	Transparent Conductive Oxide	
TRJ	Tunnel-Recombination Junction	
VHF	Very-High Frequency	

1

Introduction

Since the start of the industrial revolution in the second half of the 18th century, carbon emissions from the burning of fossil fuels have increased the concentration of carbon dioxide (CO₂) in the atmosphere [1]. CO₂ is the main contributor to the greenhouse effect [2], given that it efficiently traps the radiation emitted by the Earth. This causes the temperature of the Earth to rise and triggers the well-known phenomenon of global warming. With studies indicating that warming effects were already present as early as around the 1830s [3], we are currently living on a planet that is approximately 1 °C warmer than it was before the industrial revolution [4].

This rise in temperature poses a serious threat not only for the existence of human beings, but for nature in general. Moreover, fossil fuels are exhaustible at the rates at which it is being consumed at the moment, making a transition to another source of energy eventually inevitable. For this reason, a global collaboration is needed to effectively tackle this problem. A milestone in the right direction was the Paris Agreement of 2015, which challenges countries to limit the rise in temperature to 2 °C and preferably 1.5 °C compared to pre-industrial levels [5]. To achieve this, it is encouraged to become carbon neutral by the mid-21st century.

In this framework, *energy transition* becomes an important movement, which aims at shifting from fossil fuels to renewable energy systems to reduce the carbon emissions. From 2000 to 2018, the fraction of energy produced from renewable sources (mainly wind, solar and hydroelectric) for the worldwide energy consumption increased from 6.9 % to 10.9 %, as seen in Figure 1.1.

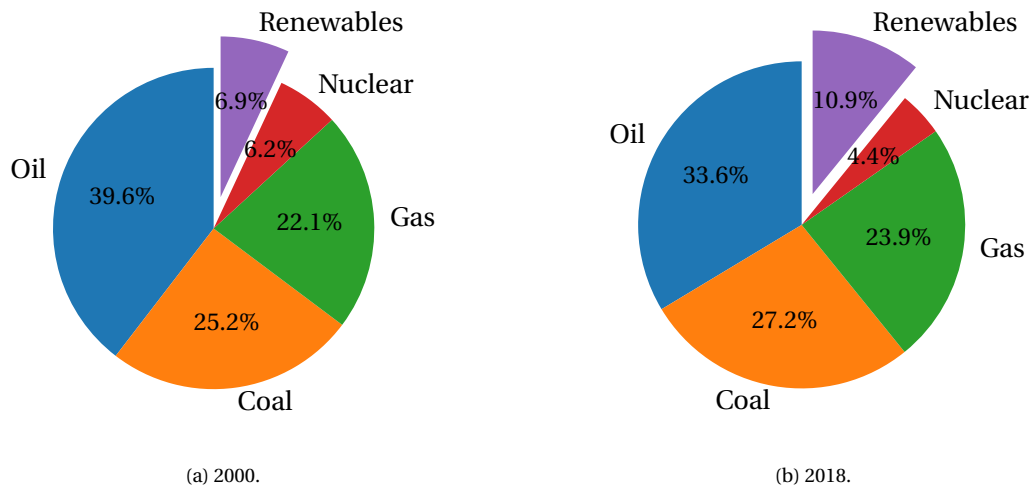


Figure 1.1: Comparison of the worldwide energy consumption by source of the years 2000 and 2018. Data from [6].

However, oil, coal and gas remain our main sources of energy, mainly due to economical and efficiency reasons. Technological advancements have worked towards improving the energy conversion and costs related to renewable energy sources, placing wind and solar energy in a competitive position against fossil-fuelled systems [7]. The next section addresses the importance of solar photovoltaics (PV) in this energy transition.

1.1. PV in the energy transition

The solar energy reaching the Earth is about 10^4 times the worldwide energy consumption [8], making it an appealing form of energy for the transition to renewable energy systems. When considering the global average total installation costs of a solar PV plant, it has dropped almost a factor 4 from 2010 to 2018, reaching a global levelized cost of electricity (LCOE) of 0.085 \$/kWh [7]. This means it can already compete with the 0.062 \$/kWh LCOE of fossil fuels [7].

Crystalline silicon technologies dominate the PV market, holding around 95% of the global shares. This has to do with the higher efficiencies of commercial modules when compared to thin-film silicon (15-21% vs 7-10%) [9], the relative low costs and the commercial status [10]. Despite this, thin-film silicon presents numerous advantages which makes it an attractive alternative to crystalline silicon.

Thin-film silicon technologies are one of the most promising options to reduce the costs of PV [11], given the use of abundant materials and ease of processing. By using thicknesses of around two orders of magnitude less than conventional crystalline silicon technologies, the production costs can be greatly reduced. Moreover, the energy payback time is estimated to be in the order of one year, at least a factor 2 lower than crystalline silicon modules [11]. Some processing techniques also allow exploiting the flexibility of thin-film silicon products, making it highly suitable for building-integrated photovoltaics (BIPV) [9].

For thin-film silicon to consolidate its position in the market, module efficiencies need to be further improved. The innovations of the FlamingoPV project aim to achieve this.

1.2. FlamingoPV

This thesis is developed within the framework of the FlamingoPV project, which stands for *Flexible Lightweight Advanced Materials In Next Generation Of PV*. It is a joint project between Delft University of Technology and HyET Solar, a company from the HyET Group. Situated in Arnhem, The Netherlands, HyET Solar strives for the production of inexpensive, light and flexible solar modules with a high energy yield. This is achieved with the use of thin-film silicon technologies (amorphous and microcrystalline silicon).

In the core of HyET Solar's roll-to-roll manufacturing process is the use of a temporary Al substrate on which the several layers of the solar module are deposited. Laser scribing allows for a monolithic interconnection of the cells conforming a module. After transferring the layers of the module to a permanent carrier, the temporary Al substrate is removed. A final encapsulation protects the module for an extended lifetime. All in all, this results in the production of modules with a thickness under 0.5 mm, a surface density of 0.6 kg m^{-2} and an energy payback time of under a year [12], using only abundant and non-toxic materials.

FlamingoPV aims to achieve five deliverables [13]:

1. Lab-scale flexible amorphous silicon/microcrystalline silicon tandem cell (5 cm^2) and module ($5 \times 5 \text{ cm}^2$) with 13 % stabilised efficiency.
2. Roll-to-roll produced modules sized $30 \times 30 \text{ cm}^2$ of 12 % aperture area stabilised efficiency with 80 % production yield.
3. Over 35 years proven lifetime of modules, with less than 20 % performance degradation.
4. Design of microcrystalline PECVD tool with CAPEX smaller than $0.2 \text{ €}/W_p$.
5. Lab-scale flexible amorphous silicon/microcrystalline silicon/microcrystalline silicon cell (5 cm^2) and module ($5 \times 5 \text{ cm}^2$) with 14 % stabilised efficiency.

The combination of these deliverables will result in PV products that can compete with crystalline silicon technologies for large scale projects and BIPV.

1.3. Thesis objectives and outline

Among the several deliverables that FlamingoPV encompasses, this work is focused on the first one: the development of a lab-scale (5 cm^2) tandem solar cell (amorphous silicon/microcrystalline silicon) with a stabilised efficiency of 13 %. Optimisation of the cell structure is indispensable to reach a design that maximises the energy conversion in such a multi-layer architecture. To this end, opto-electrical simulations are a valuable tool not only in the search for an optimal design, but also in the prediction of the performance under different conditions.

This study has the following objectives:

1. *Understand the impact of semiconductor model parameters on the performance of a solar cell:* this will provide insights into the calibration of the model to match experimental data and provide reliable predictions.

2. *Investigate the optical conditions that provide a proper light distribution in an amorphous silicon/microcrystalline silicon tandem device:* by considering the effect of the optical properties of the layers at the junction between the two cells, an evaluation of the best conditions is given. Moreover, estimations of the maximum efficiency gain with the introduction of an intermediate reflector are provided.
3. *Determine the absorber layer thicknesses in an amorphous silicon/microcrystalline silicon tandem device that maximise the conversion efficiency:* by using calibrated single-junction models, the conditions under which the performance of a tandem device is optimised are presented.

This thesis will guide the reader through the steps undertaken to reach these objectives. To start, Chapter 2 introduces the fundamentals in the fields of optics and semiconductor devices, explaining the working principle of a solar cell. Thin-film silicon devices, which are the focus of this work, are also presented. Chapter 3 deals with the experimental processes that take place in the manufacturing of the solar cells, along with the techniques used to characterise the devices. Then, Chapter 4 describes the semiconductor modelling software ASA and its use for the calibration of the physical parameters to match experimental data. A sensitivity analysis performed with an automated routine provides insights into the parameter dependence of the performance of a cell. Chapter 5 combines these findings for the optimisation of the absorber layer thicknesses to maximise the performance of the tandem device. Here, several structure scenarios are considered and an ideal intermediate reflector is designed to allow the estimation of the maximum efficiency increase that can be achieved with such a layer. Moreover, Chapter 6 provides preliminary results regarding the deposition of single- and multi-junction thin-film silicon cells. Chapter 7 finalises with the conclusions of this work, together with recommendations on future research directions regarding this area of study.

2

Fundamentals

Fundamental concepts from the field of physics, which are indispensable for the understanding of the operation of a photovoltaic device, are introduced in this chapter. Section 2.1 considers the working principle of a solar cell, discussing the optical and electrical concepts involved, the structure of a solar cell and how to assess its performance, along with the inherent limitations of such devices. Then, Section 2.2 reviews thin-film technologies, specifically the properties of two materials relevant to this work: amorphous and microcrystalline silicon. Finally, Section 2.3 closes the chapter by introducing tandem solar cells and the use of amorphous and microcrystalline silicon in such multi-junction devices.

2.1. Working principle of a solar cell

The phenomenon that describes the working principle of a solar cell is called the *photo-voltaic effect*, in which the exposure of a material to light allows the excitation of electrons. This permits the creation of a voltage or electric current [14], which can be used to perform useful work when connected to an external circuit. The impinging light must have sufficient energy to excite the electron to an allowed state, after which it must be guided to a collection point to be used outside of the generating material.

An excited electron leaves behind a void at its initial position, which is commonly described as a positively charged elementary particle called *hole*. Holes need to be extracted from the material in a similar manner (but opposite direction) as electrons. The basic working principle of a solar cell just described can be visualised in Figure 2.1.

The lower painted areas in Figure 2.1 are known as the valence band, and the upper ones the conduction band. The difference between these two bands is called the band gap E_g . The details of the generation, separation and collection of electrons and holes during the operation of a solar cell, as well as the performance and limitations of these devices, are described in the following sections.

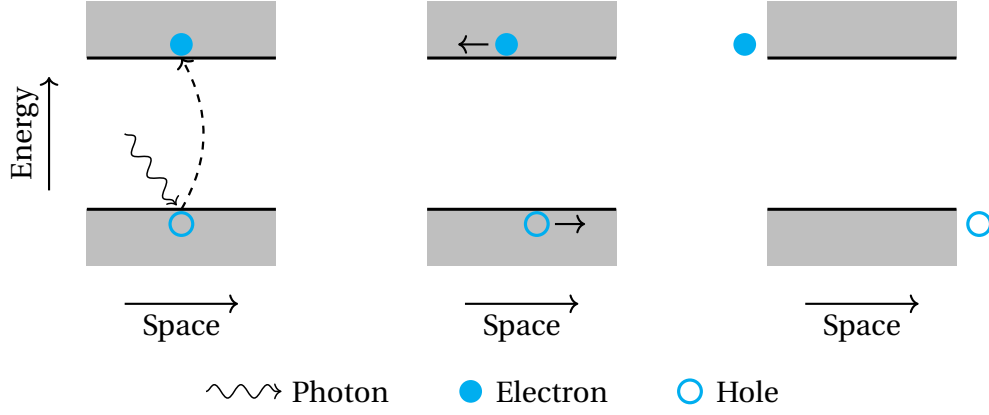


Figure 2.1: Working principle of a solar cell. The painted areas represent possible states.

2.1.1. Optics

A proper starting point for the description of optics in the field of photovoltaics (PV) is the concept of a *photon*. Planck introduced this concept in 1900 [15], and suggested to consider light as a group of discrete particles with specific energies. The energy E of a photon is given by

$$E = h\nu = h\frac{c}{\lambda}, \quad (2.1)$$

where h is Planck's constant, c is the speed of light in vacuum, and ν and λ are the photon frequency and wavelength, respectively. The distribution of photons for a given light source can be described by Planck's law when considering a black body at a specific temperature T [16]. In the case of the Sun, the emission deviates slightly from this assumption. Moreover, the spectrum changes as it crosses the atmosphere before reaching the surface of the Earth. It is exactly this modified spectrum that acts as the energy source for solar devices. To this end, the AM1.5 solar spectrum has been defined as a reference of the solar radiation reaching the surface of the Earth. This spectrum is plotted in Figure 2.2.

The presence of gaps in the spectrum is notable. This is a consequence of the absorption that takes place in the atmosphere, mainly due to CO_2 , H_2O , O_2 and O_3 [16]. The remaining light is what is left for solar devices to absorb. This absorption is dependent on the material and the energy of photons reaching it. Figure 2.3 shows the absorption coefficients α of common materials used for solar devices.

There is a clear difference between the selected materials, which has to do with many material-specific properties such as the atom arrangement and the band gap. Depending on the material and its thickness (which increases the probability of being absorbed), an incoming photon might have enough energy to be absorbed and thereby create an electron-hole pair, as described in Figure 2.1.

Photogeneration

Photogeneration is the most important electron-hole pair generation process in a solar cell [14]. The optical generation rate can be computed by considering the absorption coefficient α . To this end, *Lambert-Beer's law* is used to describe the decay of photon flux Φ as light penetrates a distance x through a material. This is given in Equation (2.2), assuming no reflection at the interface:

$$\Phi(\lambda, x) = \Phi(\lambda, 0)e^{-\alpha(\lambda)x}, \quad (2.2)$$

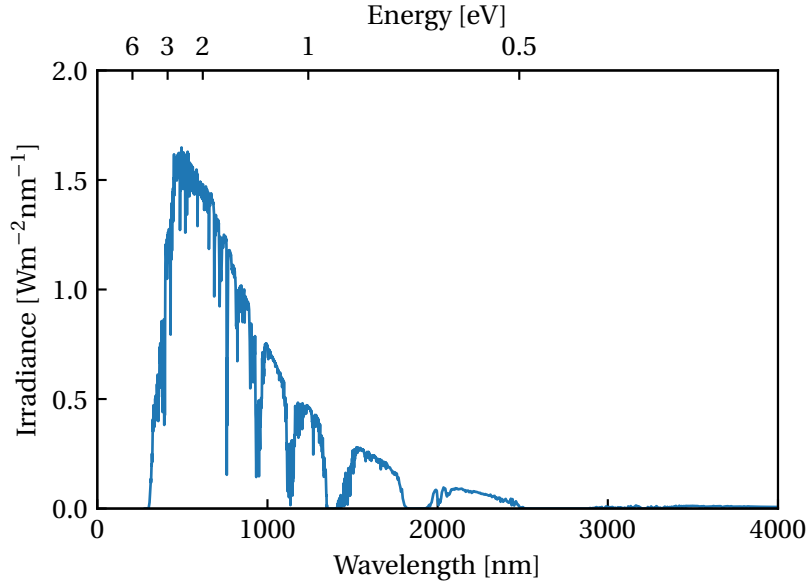


Figure 2.2: AM1.5 solar spectrum [17]. The conversion for the top x -axis is given by Equation (2.1), in units of *electronvolt* (eV).

with $\Phi(\lambda, x)$ the photon flux as a function of wavelength and position. $\Phi(\lambda, 0)$ can be computed from the irradiance spectrum $I_{e\lambda}$ shown in Figure 2.2, by dividing the irradiance by the photon energy at that wavelength, which is given by Equation (2.1):

$$\Phi(\lambda, 0) = I_{e\lambda} \frac{\lambda}{hc}. \quad (2.3)$$

With this, the photogeneration rate can then be computed by multiplying the absorption by the photon flux [14]:

$$G(\lambda, x) = \alpha(\lambda)\Phi(\lambda, 0)e^{-\alpha(\lambda)x}. \quad (2.4)$$

To compute the generation rate over a range of wavelengths, or up to a specified depth in a material, Equation (2.4) can be integrated within the relevant scope.

Direct and indirect absorption

The absorption effectiveness, reflected in the magnitude of the absorption coefficient α , depends on the nature of the electron-hole pair excitation. Two types of band gaps can be identified, with either *direct* or *indirect* excitations. The allowed energy states are a function of the wavevector \mathbf{k} , commonly known as the *dispersion relation*. The dispersion relation of direct and indirect band gap materials is shown in Figure 2.4.

As seen in the dispersion relations, direct band gap materials are characterised by the alignment with respect to the wavevector of the maximum of the valence band and the minimum of the conduction band. In contrast, these points are shifted in the wavevector space for indirect band gap materials. For the direct case, the absorption of a photon with sufficient energy is enough to excite an electron into the conduction band, thereby creating an electron-hole pair. By contrast, an indirect transition also requires a change in momentum for the excited electron.

Due to conservation of momentum, the electron needs to interact with the lattice of the material in order for this change in momentum to happen. This interaction occurs

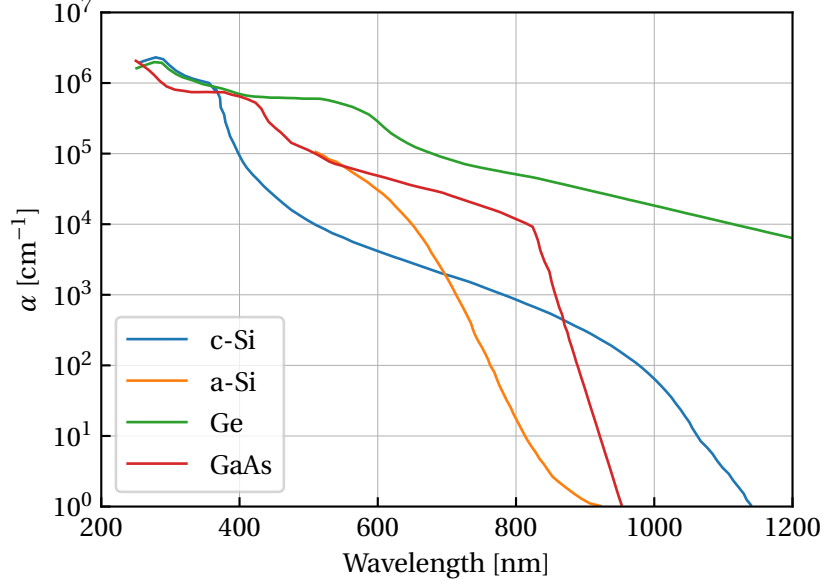


Figure 2.3: Absorption coefficients of some materials used in PV. Adapted from [18].

as a lattice vibration, which is called a *phonon*. Given the fact that an indirect transition requires the participation of both a photon and a phonon, the absorption coefficient for such materials is often significantly lower than for direct transition materials [8].

Reflection at an interface

The optical properties of a material can be described by the complex index of refraction, which is given by Equation (2.5).

$$\tilde{n} = n + i\kappa, \quad (2.5)$$

where n is the index of refraction and κ is the absorption index, which is related to the absorption coefficient plotted in Figure 2.3 by Equation (2.6) [8].

$$\kappa = \frac{\alpha\lambda}{4\pi}. \quad (2.6)$$

At the interface between two media, there is an abrupt change of these properties, which causes some of the light to reflect or transmit. A sample diagram is shown in Figure 2.5. By matching the conditions at each side of the interface for the electric and magnetic waves, we can arrive at reflection and transmission amplitudes of the incoming wave. These are called the Fresnel coefficients. The reflection coefficients for parallel (\parallel) and perpendicular (\perp) electric field polarisation with respect to the plane of incidence are given by Equations (2.7).

$$R_{\parallel} = \left| \frac{\tilde{n}_1 \cos(\theta_2) - \tilde{n}_2 \cos(\theta_1)}{\tilde{n}_1 \cos(\theta_2) + \tilde{n}_2 \cos(\theta_1)} \right|^2, \quad (2.7a)$$

$$R_{\perp} = \left| \frac{\tilde{n}_1 \cos(\theta_1) - \tilde{n}_2 \cos(\theta_2)}{\tilde{n}_1 \cos(\theta_1) + \tilde{n}_2 \cos(\theta_2)} \right|^2, \quad (2.7b)$$

where \tilde{n}_1 and \tilde{n}_2 are the complex refractive indices of media 1 and 2 and θ_1 and θ_2 the incoming and transmitted angles. The average of R_{\parallel} and R_{\perp} is the reflection coefficient for

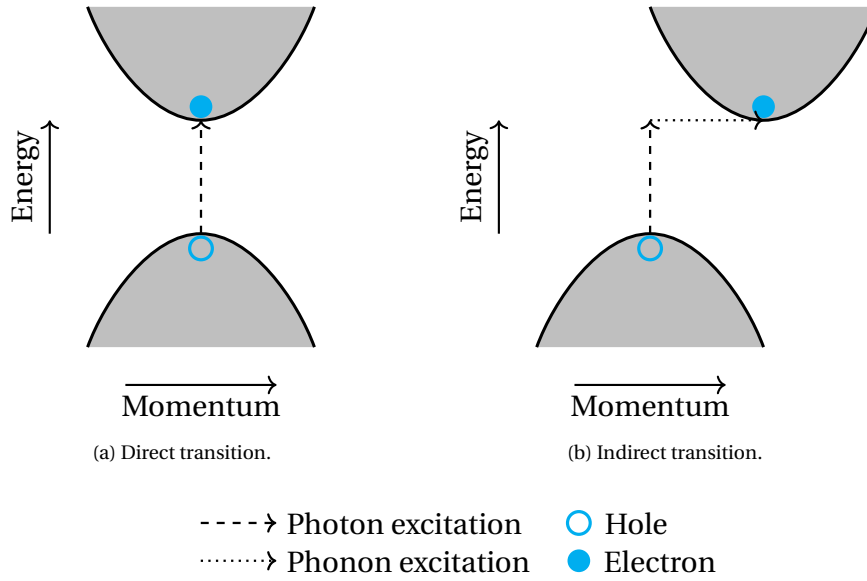


Figure 2.4: Dispersion relation for a) direct and b) indirect band gap materials. Inspired by [8].

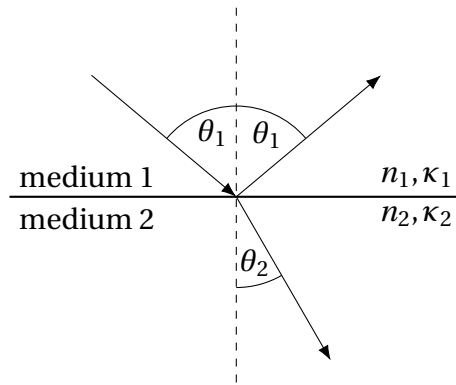


Figure 2.5: Visualisation of the reflection and transmission of a wave reaching the interface between two different media 1 and 2 and the relevant parameters.

unpolarised light, R . Snell's law needs to be used to compute the angle θ_2 :

$$\tilde{n}_1 \sin(\theta_1) = \tilde{n}_2 \sin(\theta_2). \tag{2.8}$$

Fresnel equations are only valid when medium 1 is non-absorptive ($\kappa_1 = 0$), whereas this condition is relaxed for medium 2. If both media are absorptive, then Equations (2.7) become approximative [19], but still result in more accurate coefficients when compared to the case when the absorption index is neglected [20].

2.1.2. Semiconductors

An introduction to the fundamentals of solar cells is impossible without a description of semiconductor physics. *Semiconductors* are materials which have a relatively low band gap E_g (typically less than 4 eV [21]), such that the conduction properties can be controlled. Under low excitations, it can pass from being an insulating material to a conducting one. For the remaining of this chapter, the concepts of semiconductor physics will be explained using the example of crystalline silicon (c-Si).

Band gap formation

Before the formation of a c-Si structure, each Si atom has quantised levels at which its electrons can be excited. When c-Si is formed, the Si atoms will arrange themselves in a so-called *diamond* structure, which allows the atoms to covalently bind with its four neighbours [8]. This periodic arrangement of covalent bonds results in an interaction between the possible states the electrons can be in, resulting in a quasi-continuous distribution of allowed states in the conduction and valence band [15]. In the case of c-Si, the band gap corresponds to 1.12 eV. A 2D spatial representation of the arrangement of Si atoms in their crystalline structure can be seen in Figure 2.6.

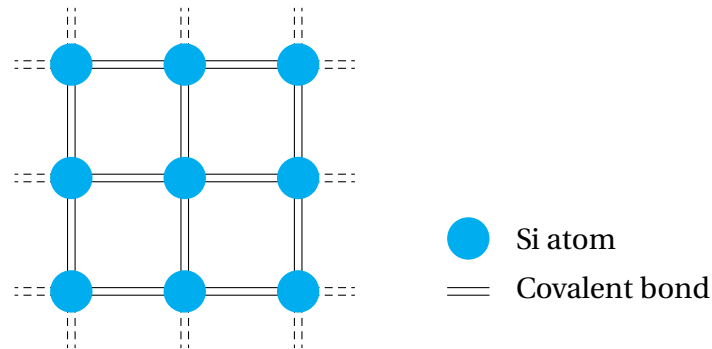


Figure 2.6: 2D representation of the structure of c-Si.

Doping

Pure c-Si is called *intrinsic*, since the number of impurities in the material is very limited. This may seem favourable in terms of material purity and homogeneity. However, the ability to introduce impurities in the periodic structure of crystals is essential for the functioning of semiconductor devices, and is one of its main features [8]. The insertion of impurities, also called *dopant* atoms, allows the control of the electron and hole concentrations, and transforms it into an *extrinsic* material. The principle of doping can be seen in Figure 2.7.

Two cases can be identified:

- a) *Donor*: an element with more valence electrons than Si is introduced in the lattice, which results in free electrons (not bound to an atom). Phosphorus is typically used as donor element.
- b) *Acceptor*: the introduction of an atom with less valence electrons than Si leaves an empty electron bond, which can be seen as a hole. Boron is typically used as an acceptor element.

An *n*-type semiconductor has a dominance of donor atoms over acceptor atoms, and vice versa for a *p*-type semiconductor. By modifying the doping concentration, the conductivity can be altered [8]. Depending on the doping, a so-called *Fermi energy* E_F can be defined. This is the electrochemical potential of the electrons [8], also defined as the highest occupied energy level. For intrinsic materials, this energy level lies in the middle of the gap. For *p*-doped materials, the energy level is shifted down towards the valence band, whereas a shift to the conduction band is seen for *n*-doped materials.

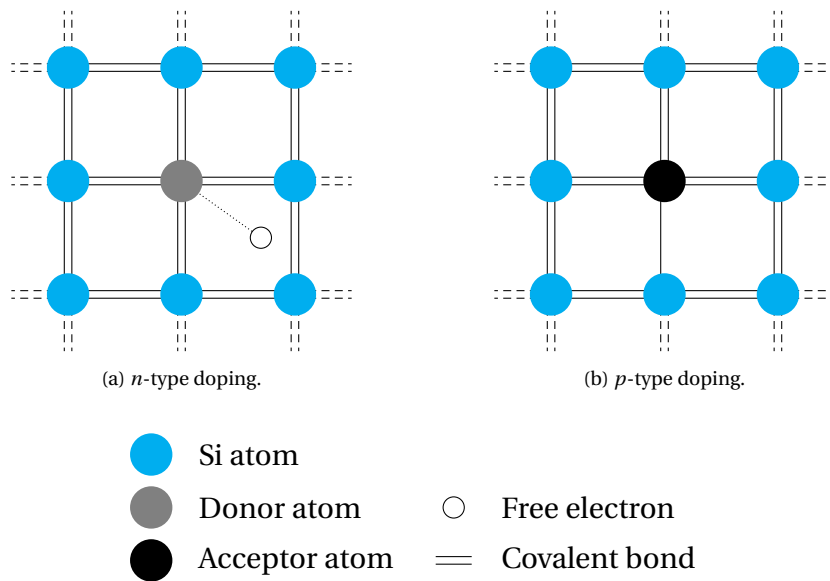


Figure 2.7: 2D representation of the doping procedure in c-Si where a) a donor atom is introduced and b) an acceptor atom is introduced. Inspired by [15].

pn junctions

Interesting things happens when *p*-type and *n*-type semiconductors are put in contact with each other. This can be visualised in Figure 2.8.

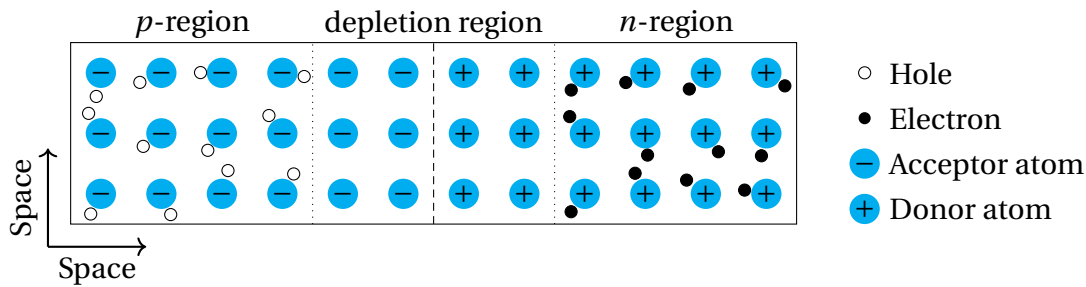


Figure 2.8: Top view of a pn junction. Inspired by [8].

Due to a density gradient at the cross-over between the *p*- and the *n*-type material, free electrons from the *n*-region will diffuse into the *p*-region, and the same holds for holes from the *p*- into the *n*-region [15]. Since the free charge carriers are leaving the initially neutral atoms, there is a positive charge build-up at the *n* side and a negative one at the *p* side (in the region near the interface). This results in an electric field pointing from the *n* side to the *p* side. This transport process continues until there is a balance between the diffusion (due to concentration gradient) and drift (due to the electric field) forces, assuming no external forces are acting on the junction. In the end, there is a region near the interface with a net charge, called the *depletion region*. This region creates a somewhat selective membrane for charge transport, which allows the separation of charges depicted in Figure 2.1.

The width of the depletion region at each side of the interface is dependent on the concentration of both donor and acceptor atoms. Assuming the electric field vanishes abruptly at the termination of the depletion region, Equation (2.9) can be found [15].

$$N_a x_p = N_d x_n, \tag{2.9}$$

where N_a and N_d are the concentration of acceptor and donor atoms, respectively, and x_p and x_n are the width of the depletion region at the p and n side of the junction, respectively. Therefore, a higher concentration of dopant atoms at one side of the junction is compensated by an increase of the distance the electric field penetrates into the other side of the junction. The equilibration process when a pn junction is formed can also be analysed from a band diagram perspective. This can be seen in Figure 2.9.

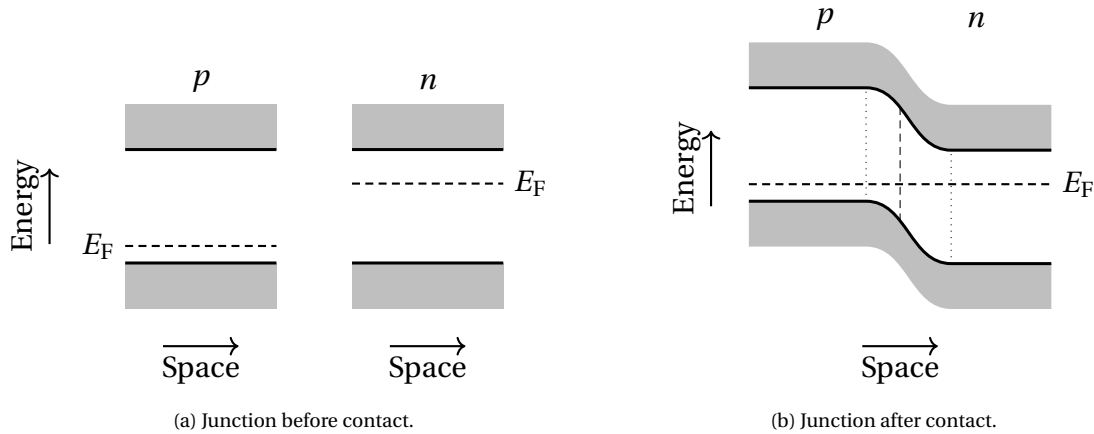


Figure 2.9: Thermal equilibrium band diagrams of a pn junction a) before contact and b) after contact. Inspired by [15].

In a band diagram, the energy levels as a function of space are plotted. In Figure 2.9a, the valence and conduction band energies are constant in space. The Fermi level of the p -doped side has been shifted downwards with respect to the intrinsic level, and upwards for the n -doped side. The fact that the shift at the n -doped side from the middle of the gap is less with respect to the p -doped side means that the concentration of donor atoms N_d at the right side is less than the concentration of acceptor atoms N_a at the left side.

When put into contact, diffusion of electrons and holes will happen in the depletion region. When thermal equilibrium is reached, which can be evidenced by the constant Fermi level as a function of space, the band diagram in Figure 2.9b is obtained. The movement of free charge carriers has created a potential barrier that develops across the depletion region. This phenomenon is called *band bending*, given the notorious effect it has on the energy of the bands. This barrier extends more into the n -doped side, as computed in Equation (2.9) with $N_d < N_a$.

Metal-semiconductor junction

In order to connect the solar device to an external circuit, we need extract the charge carriers from the device, which is the process depicted at the right in Figure 2.1. This is normally done with a low resistance metal-semiconductor junction, commonly called an *ohmic contact*. Such a contact allows good conduction in both directions between the two materials. The contact is improved as the doping level of the semiconductor increases, when tunnelling will dominate the dominant transport mechanism [15].

2.1.3. Layer build-up of a solar cell

Combining the knowledge from the previous subsection, it is useful now to look at the complete picture of a solar cell. To this end, a typical *amorphous silicon* (a-Si) cell is de-

composed into its layers and subsequently analysed. The structure of such a cell is shown in Figure 2.10.

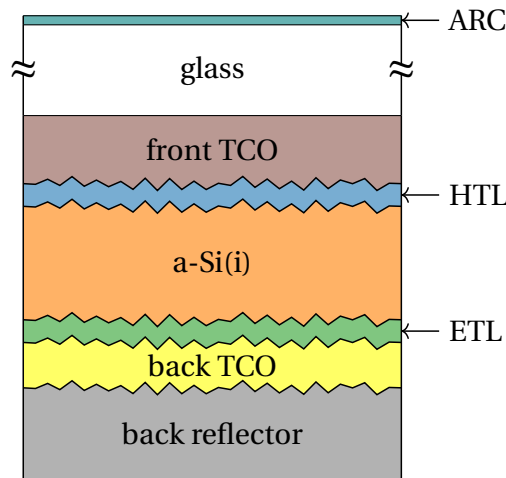


Figure 2.10: Sample structure of an a-Si solar cell. The layer thicknesses are not to scale.

This cell is an example of a *pin* (or *superstrate*) configuration, which stands for the order of the deposited layers ($p \rightarrow i \rightarrow n$). The role of each layer is analysed from top to bottom:

1. *ARC*: anti-reflection coating. Due to a mismatch of the optical constants of the top of the cell and the outside medium, reflection will take place according to the Fresnel relations given in Equations (2.7). This partial reflection is undesired, since it decreases the amount of light reaching the active layers. To solve this, different materials can be used to minimise the reflection, ranging from single-layer coatings (for instance using SiO_2 or TiO_2 [22]) to multi-layer coatings (for instance, combinations of SiO_2 and TiO_2 to reach an average reflectance of around 4% for an air-silicon interface [23]).
2. *glass*: it offers physical support for the deposition of the other layers. Moreover, it serves as a protection against outdoor weather conditions.
3. *front TCO*: front transparent conductive oxide. This is the front contact of the solar cell, so it must be highly conductive. In addition to this, it must be highly transparent to avoid light being absorbed before it reaches the active layers. Typical materials are aluminium-doped zinc oxide ZnO:Al (AZO), fluor-doped tin oxide $\text{SnO}_2:\text{F}$ (FTO) and indium tin oxide, which is a combination of In_2O_3 and SnO_2 (ITO) [8].
4. *HTL*: hole transport layer, normally p -doped amorphous silicon. The insertion of this layer aids in the collection of holes by generating an electric field pointing from the i -layer to the p -layer, repelling electrons from passing to the front TCO.
5. *a-Si(i)*: intrinsic amorphous silicon. Also called the *absorber layer*, this is where the photons are absorbed to generate electron-hole pairs.
6. *ETL*: electron transport layer, normally n -doped amorphous silicon. Serves the same role as the p -layer but for electrons: generates an electric field directed towards the i -layer to block the holes and allow electrons to reach the back TCO.

7. *back TCO*: back transparent conductive oxide. This layer is often inserted to enhance reflection of unabsorbed photons reaching the back of the cell and to guide the electrons to the back reflector. Typical materials are similar to the ones mentioned for the front TCO: AZO and ITO [24].
8. *back reflector*: back contact of the solar device. Here, the electrons are collected. A highly reflective material such as Al or Ag is chosen to reflect the remaining photons back to the active layers.

With this structure, the front TCO and back reflector are the positive and negative contacts of the cell, respectively. Some of the interfaces between layers in Figure 2.10 are not flat. This texturing is used for two reasons:

- a) Decrease reflection: light that reflects at an angle has the possibility of encountering the interface again.
- b) Increase the average path of photons: light that is refracted is scattered over a range of angles, such that the distance it travels across the materials increases.

2.1.4. Solar cell performance

Two of the most common indicators to judge the performance of a solar cell are the current-voltage characteristic ($I - V$ curve) and the external quantum efficiency (EQE). These are explained next.

$I - V$ curve

A common way of identifying a diode (pn junction) is with its current-voltage characteristic, which follows the exponential relationship in Equation (2.10) known as the Shockley diode equation [8]:

$$I = I_0 \left[e^{\frac{qV}{nk_B T}} - 1 \right], \quad (2.10)$$

with I the current, I_0 the reverse bias saturation current, q the elementary charge, V the voltage, n the ideality factor, k_B the Boltzmann constant and T the temperature. n is normally a value between 1 and 2 and is determined by the type of recombination that it dominant in the used material. When exposing a diode to light, Equation (2.10) receives an additional term due to the photogenerated current: I_{ph} . A solar cell can be modelled as a circuit with these two components, with additional resistances as a consequence of non-ideal operation. The one-diode equivalent circuit of a solar cell is shown in Figure 2.11.

The inclusion of a series resistance R_s accounts for contact resistances with the semiconductor when extracting the current. Moreover, the shunt resistance R_{sh} takes into account manufacturing defects, which could provide alternative paths for the current of the device [25]. Taking all the components in Figure 2.11, the resulting current-voltage relationship of a solar device results in the implicit relation given by Equation (2.11).

$$I = I_{\text{ph}} - I_0 \left[e^{\frac{q(V+IR_s)}{nk_B T}} - 1 \right] - \frac{V + IR_s}{R_{\text{sh}}}. \quad (2.11)$$

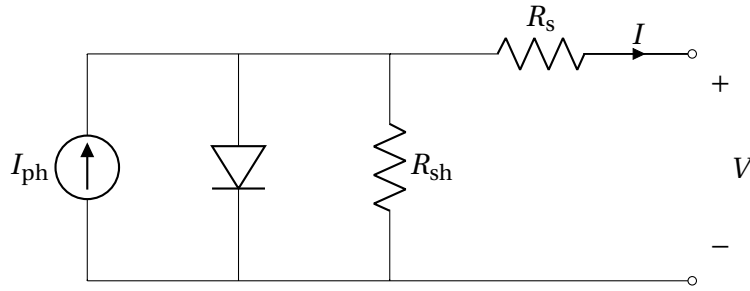
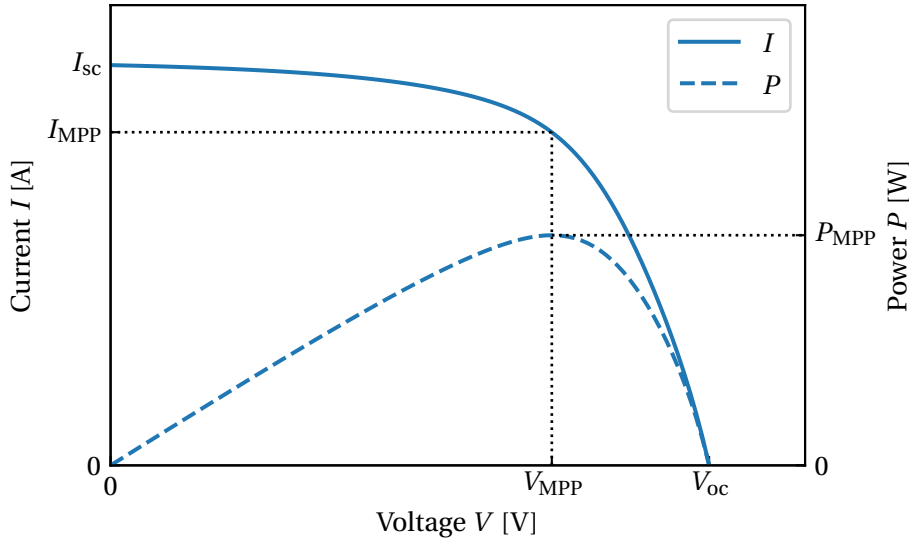


Figure 2.11: Equivalent circuit model of a solar cell. Inspired by [8].

Figure 2.12: Sample $I - V$ and $P - V$ curve of a solar cell under illumination.

This relationship gives the possible $I - V$ combinations at which a solar cell can operate. For each combination, the power P delivered is simply $I \cdot V$, expressed in W. Figure 2.12 plots both the current and power as function of voltage for an illuminated solar cell.

Commonly used performance indicators of a solar cell have been marked in Figure 2.12. To start, the open-circuit voltage V_{oc} . This is the voltage delivered when the terminals of the device are connected via an infinite resistance. Then, the short-circuit current I_{sc} , which is the current produced by the device when the terminals are connected to each other. The V_{oc} and I_{sc} is the maximum voltage and current a solar cell can deliver, respectively. However, at both these points the power of the device equals zero, since either the current or voltage is zero. For operation points in between these extremes, a maximum power point MPP can be found, which represents the operation at which the largest amount power is extracted. For this reason, it is the condition at which solar modules are often forced to operate in.

With the definitions explained above, a new parameter can be defined: the fill factor FF :

$$FF = \frac{V_{MPP} I_{MPP}}{V_{oc} I_{sc}}. \quad (2.12)$$

From a geometrical point of view, the FF is an indication of how much the shape of the

$I - V$ curve deviates from a rectangle marked by the points (V_{oc}, I_{sc}) .

The most important parameter of a solar cell is its efficiency, η , which quantifies the maximum fraction of incoming power the device is able to transform to electricity. This is given by Equation (2.13).

$$\eta = \frac{V_{MPP} I_{MPP}}{P_{in}} = \frac{V_{oc} I_{sc} FF}{P_{in}}, \quad (2.13)$$

with P_{in} the power impinging on the cell. The reference for this power is the AM1.5 solar spectrum, which corresponds to a power density of 1000 W m^{-2} . This power is expressed per unit area, such that its product with the area of the device gives the input power. On a final note, instead of using I_{sc} , the short-circuit current *density* J_{sc} (in A m^{-2}) of a solar cell is often used for an area-independent quantification of the current under short-circuit conditions.

External Quantum Efficiency

The external quantum efficiency (EQE) of a solar cell is the ratio between the number of collected electron-hole pairs and the number of incident photons at a specific wavelength. It gives an indication of the contribution of each part of the spectrum to the current produced by the device. Figure 2.13 gives an example of an EQE plot.

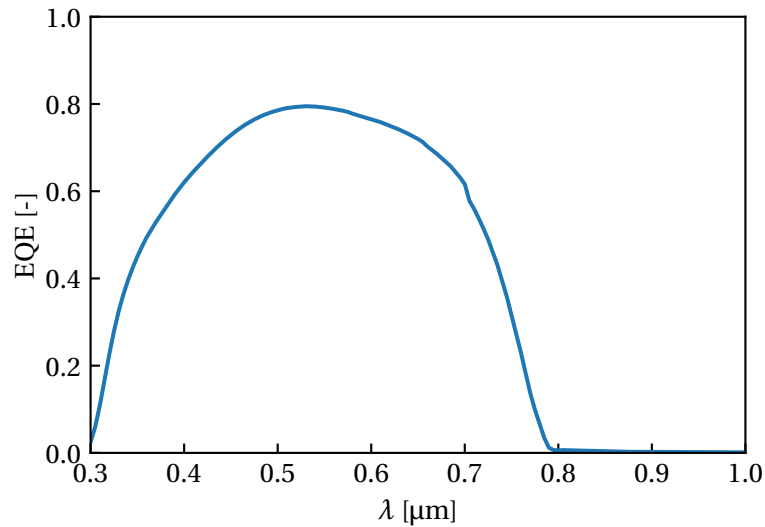


Figure 2.13: Sample EQE curve of a solar cell.

When measured under short-circuit conditions, the integration of the EQE with the corresponding photon flux results in the short-circuit current I_{sc} :

$$I_{sc} = q \int_0^{\infty} \text{EQE}(\lambda) \Phi(\lambda) d\lambda, \quad (2.14)$$

with Φ the photon flux, commonly defined with the AM1.5 spectrum. The upper boundary of the integral is often substituted with the wavelength corresponding to the band gap of the semiconductor device, since the EQE is zero above this value.

2.1.5. Limitations

There are a number of inherent properties of solar cells that limit their efficiency, which is why we cannot convert a large part of the incoming energy in the photons to electrical energy. This subsection will describe the most important contributions that prevent solar cells from being ideal.

Limited photon energy

As presented in Figure 2.1, semiconductors can be characterised by a band gap energy E_g . When we look at the spectrum of the sun, there are many photons that have a lower energy than E_g , and can therefore not provide an electron with enough energy to be excited to the conduction band. The energy carried by these non-absorbed photons is therefore not converted into electrical energy. As the energy of the band gap increases, so does the number of photons that cannot be absorbed. For instance, if we consider c-Si at a band gap of 1.12 eV, around 20% of the photons are lost due to this phenomenon. For a-Si at a band gap of 1.7 eV, the losses amount to around 50%.

Thermalisation

For the photons that have an energy higher than E_g , there is also a loss mechanism involved. When a photon with such an energy is absorbed, an electron is excited above the edge of the conduction band. This process is possible because there is a quasi-continuum of states above this edge, as seen in Figure 2.1. Given the high energy state of the excited electron, it can easily undergo interactions with the atoms of the material, losing energy to phonons (lattice vibrations). This causes its energy to quickly drop from above the conduction band to the edge, where it is more stable. This loss of energy is called *thermalisation*, given the fact that the chemical energy is lost to thermal energy in the material. The process described above also holds for holes formed below the edge of the valence band, making them quickly thermalise to the edge of this band. Typically, this phenomenon takes place in a time in the order of femtoseconds to picoseconds [14], significantly faster than the time it takes to extract excited electrons and holes.

Bulk recombination

Even after thermalisation has taken place, there is still a way generated electron-hole pairs can be lost, and this is called *recombination*. There are three types of recombination happening in the bulk of a material:

1. *Radiative*: also called *band-to-band* recombination, it is more dominant in direct band gap semiconductors [8]. This recombination happens when an excited electron in the conduction band recombines with a hole in the valence band, effectively annihilating an electron-hole pair. As a result, a photon with the band gap energy E_g is emitted, which easily escapes the material due to the weak absorption at this energy. The rate of recombination is proportional to the concentration of electrons and holes in the conduction and valence band, respectively, and is typically written as [8]

$$R_r = \beta(np - n_0p_0), \quad (2.15)$$

where n and p are the total electron and hole concentrations, respectively, and where the subscript 0 indicated thermal equilibrium concentrations. The radiative recombination coefficient β is dependent on the material [14].

2. *Shockley-Read-Hall*: it is a non-radiative type of recombination, and happens due to the presence of defects in the material. As a consequence of these impurities, localised energy states, called *trap states*, become available in the forbidden gap between the conduction and valence band. These can act as *recombination centres*, facilitating the capture of electrons and holes. In general, the energy is lost to phonons in the material. Depending on the nature of the trap state, it will capture either electrons or holes, but in a wide sense it depends on the electron and hole concentrations, electron and hole capture cross sections and the concentration of trapping centres. This is the most dominant recombination process in typical semiconductor operations [8].
3. *Auger*: dominant in indirect band gap or highly doped semiconductors, this recombination process involves three particles. After the electron and hole have recombined, the energy is transferred to a third particle, either a hole or an electron. The excitation energy of the third particle is quickly dissipated as phonons to the lattice of the materials, which then results in heat. Depending on whether the material is heavily *n*-type or *p*-type doped, the excitation of the third particle will mostly occur to an electron or a hole, respectively. The sum of these two recombinations determines the total Auger recombination rate [8]:

$$R_A = R_{eeh} + R_{ehh} = C_n n^2 p + C_p n p^2, \quad (2.16)$$

where C_n and C_p are proportionality constants for the occurrence of electron-electron-hole (eeh) or electron-hole-hole interactions (ehh), respectively.

Surface recombination

Besides bulk recombination, *surface recombination* often plays an important roll in limiting the efficiency of solar devices. Unlike bulk recombination, which happens in the interior of a material, surface recombination is the phenomenon that happens at the surface of a material. Due to the termination of the material structure present in the bulk, there are many unpaired valence electrons, which results in the so-called *dangling bonds*. These act as effective recombination places for the arriving carriers from the bulk. For pure semiconductors, surface recombination may dominate over bulk recombination [8].

Light utilisation

Ideally, a solar cell would absorb all of the incoming light with enough energy in the proper layer (*intrinsic* layer in Figure 2.10). Nevertheless, this is not possible due to the following reasons:

1. *Reflection*: a mismatch between the refractive indices, as described in Section 2.1.1, can partially reflect the incoming wave. As there are many interfaces before the light reaches the desired absorption layer, the effect is enhanced.
2. *Incomplete absorption*: the absorption is determined by the absorption coefficient α and can be modelled by Lambert-Beer's law, as mentioned in Section 2.1.1. Given the exponential decay, one would need an infinitely thick material to absorb all the photons with enough energy, regardless of the absorption coefficient. The finite thickness of real solar cell devices therefore limits this complete absorption.

3. *Parasitic absorption*: only the electron-hole pairs generated in the desired layer can be separated and collected. However, absorption also takes place in the layers of the device located before in the path of the light. This absorbed part of the spectrum is therefore not available for the desired absorber layer, which is why this phenomenon is called *parasitic absorption*.

2.2. Thin-film silicon devices

Typical c-Si solar cells, which are classified under *first generation* solar cells, have absorber layers of over 100 μm . This has to do with the fact that its band gap is indirect [26], which results in a low absorption coefficient and the need of a thick layer to absorb enough photons. For direct band gap transitions, a much thinner absorber layer is sufficient, which brings us to the *second generation* solar cells: thin-film (TF). With thicknesses up to tens of micrometres [27], the amount of material needed is much less, and the production throughput is enhanced. However, the electrical properties also change drastically and need to be described for a proper understanding of such devices. The focus of this work lies in thin-film silicon devices, specifically on *amorphous* silicon (a-Si) and *microcrystalline* silicon ($\mu\text{c-Si}$).

2.2.1. Amorphous silicon

The first a-Si layers were deposited in 1969 [28], where a variation of the material properties with temperature was observed. With the ability of doping this amorphous structure in 1975 [29], the first a-Si solar cell was created in 1976 [30], which had an initial efficiency of 2%. The current world record is held by AIST from 2015 [31], developing a 1 cm^2 cell with a stabilised efficiency of 10.2%. This was achieved with the following set of parameters: $J_{\text{sc}} = 16.36 \text{ mA cm}^{-2}$, $V_{\text{oc}} = 0.896 \text{ V}$ and $\text{FF} = 0.698$ [32]. The material properties of a-Si are described next.

Atomic structure

The arrangement of silicon atoms in an amorphous network differs from the structure present in the crystalline phase. Unlike c-Si, there is a wide distribution of bond lengths and angles. For this reason, short-range order is present, but it is not possible to talk about long-range order [33]. The disorder present in the material gives rise to silicon bonds that have not been saturated due to the absence of another Si atom in the neighbourhood. This gives rise to a so-called *dangling bond*, and effectively acts as a recombination centre.

The electronic properties of the material just described would be unsuitable for electronic applications [24], which is where hydrogen comes into play. By introducing hydrogen in the atomic structure, the unsaturated bonds can be linked to a hydrogen atom, removing a possible recombination centre [33]. It is said then that the *unpassivated* dangling bond is now *passivated*. This allows dangling bond densities to be reduced from values of 10^{19} cm^{-3} to around 10^{16} cm^{-3} [27]. A 2D representation of the atomic structure the described material, denoted *hydrogenated* a-Si (a-Si:H), can be seen in Figure 2.14. a-Si and a-Si:H are often used interchangeably.

Density of states

Due to the local order present in a-Si:H, we can speak of a valence and a conduction band, as in the case of c-Si. However, the edges of these bands are not very well defined, and

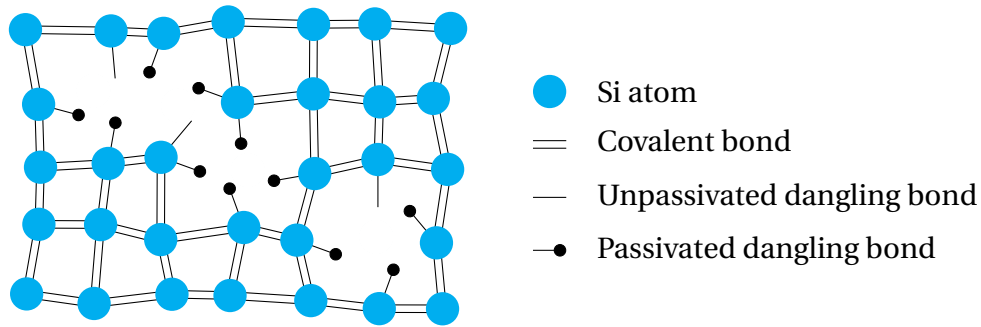


Figure 2.14: 2D representation of the atomic structure of a-Si:H.

this has to do with the disorder present in the material. This gives rise to tail states that extend into the normally forbidden gap of c-Si, at both the valence and conduction band edges [24]. Moreover, the presence of dangling bonds introduces electronic states around the centre of the gap [34]. All these available states can be visualised in Figure 2.15.

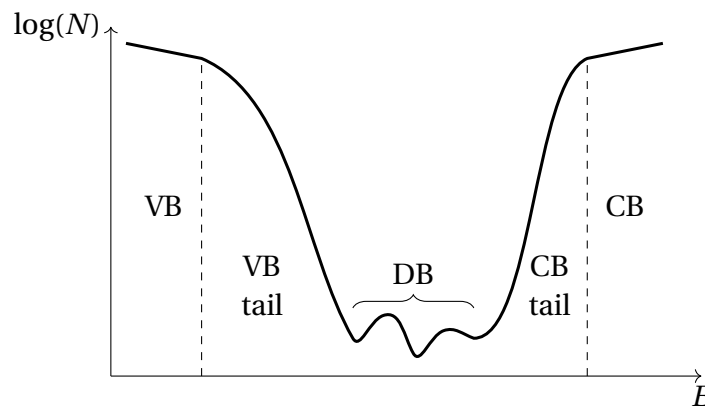


Figure 2.15: Density of electronic states N of a-Si:H as a function of energy E . DB: dangling bonds, VB: valence band, CB: conduction band. Inspired by [24].

The states below the valence band edge and above the conduction band edge in terms of energy are non-localised, which means that holes in the former and electrons in the latter behave as free charge carriers [24]. This labels these states as *extended states*. Carriers in the states between these edges have a localised nature and are given the name *localised states*. In the case of a-Si:H we cannot speak of a band gap given the continuity of states as a function of energy. Instead, the term *mobility gap* (E_{mob}) is used, which separates the localised and extended states [35], and is shown in Figure 2.15.

E_{mob} is highly dependent on the deposition conditions: a decrease in temperature and increase of hydrogen in the silicon network both result in the increment of the mobility gap value [34]. This has to do with the influence of the deposition parameters on the growth of the material, which will be further explained in Section 3.1.1.

Staebler-Wronski effect

In 1977, Staebler and Wronski observed the decrease of photoconductivity and dark conductivity after a long exposure of a-Si:H to light [36]. This effect, called the *Staebler-Wronski effect* (SWE) was later attributed to the creation of dangling bonds, which act as recombination centres and therefore decrease the mobility of the charge carriers. However, the effect

is reversible, such that the initial state of the material can approximately be obtained after annealing at temperatures of 150 °C to 200 °C [37]. This passivates the bonds that were broken during the exposure to light. The SWE reduces the efficiency of a-Si:H solar cells to about 85 % of its initial efficiency, and the degradation stops after about 10^3 hours of exposure [8]. This is the reason the efficiencies of a-Si:H cells are denoted as *initial* or *stabilised*, depending on whether the cell has undergone the mentioned period under light exposure.

The SWE can be decreased by introducing more hydrogen during the deposition of the material or by increasing the deposition temperature [38], as long as the material remains amorphous and does not change to a more crystalline phase. Moreover, by decreasing the absorber layer thickness, the electric field is enhanced, which allows for a better extraction of charge carriers despite the mobility reduction the SWE brings along [39].

2.2.2. Microcrystalline silicon

In 1967, the first layers of microcrystalline silicon ($\mu\text{c-Si}$), also called nanocrystalline silicon (nc-Si), were described [40]. For many years, there was a disbelief that such a material would be suitable as an absorber layer in a solar cell. The first successful $\mu\text{c-Si}$ absorber layer, which could be used in a solar cell, was produced in 1990 [41]. In 1994, the first $\mu\text{c-Si}$ solar cells were created, with an efficiency of 4.6 % for a 5 mm² device [42]. The current world record is, like for a-Si:H, held by AIST from 2018 [31]. With $J_{\text{sc}} = 28.74 \text{ mAcm}^{-2}$, $V_{\text{oc}} = 0.550 \text{ V}$ and $\text{FF} = 0.750$, an efficiency of 11.9 % was obtained on a 1 cm² cell [43]. As a material, $\mu\text{c-Si}$ differs in a lot of ways from a-Si. This is introduced below.

Atomic structure

Microcrystalline silicon can be seen as an intermediate phase between the highly-ordered c-Si material and the disordered a-Si phase. It is generally considered as being composed by crystalline grains located in a matrix of amorphous tissue, with occasional voids (gaps where no material is present). These crystalline grains have sizes ranging from a few nanometres to microns [34]. The exact composition of the material will depend on the deposition parameters, but a general visualisation can be seen in Figure 2.16.

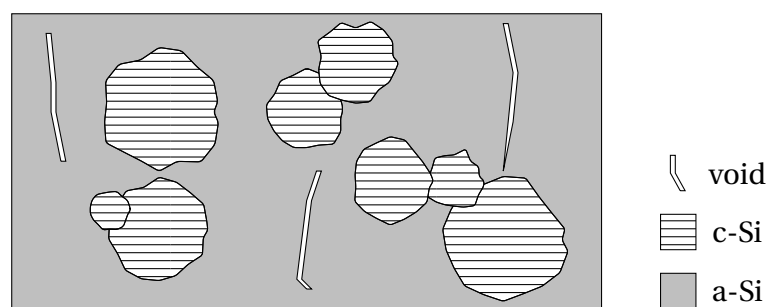


Figure 2.16: Structural composition of $\mu\text{c-Si}$. Inspired by [44].

As with a-Si, hydrogen is an important component during the deposition for the passivation of dangling bonds in the amorphous tissue, which is why the material is often called *hydrogenated* $\mu\text{c-Si}$ ($\mu\text{c-Si:H}$). But more importantly, it is crucial during the growth process to actually obtain a microcrystalline structure [34], since the reduction of the hydrogen content during the deposition may give rise to a continuous amorphous material instead.

Density of states

The density of states of $\mu\text{c-Si:H}$ has not, in general, been considered as a superposition of its phases (c-Si and a-Si:H) [34]. However, given the fact that it is a material with structural defects, states in-between the conduction and valence band can be expected. Dangling bonds will primarily provide these states, since it is believed that tail states cannot be present in the extent as it is with a-Si:H due to their incompatibility within the crystalline grains. Unlike a-Si:H, a proper description of the DOS is not yet available [34].

Material growth

To increase light absorption in $\mu\text{c-Si:H}$, the material is often grown on textured substrates. For a-Si:H, the material growth on common textures allows for a high J_{sc} , while maintaining a proper V_{oc} and FF . However, the V_{oc} and FF seem to deteriorate when $\mu\text{c-Si:H}$ is grown on similar substrates [45], and this is attributed to the effect of cracks/voids that arise during the deposition. Given that $\mu\text{c-Si:H}$ has a lower optical absorption than a-Si:H, the absorber layers need to be grown thicker, such that good control of the material quality as it is being deposited is needed. Instead of V-shaped craters, the smoother U-craters of the texture seem to be favourable for a crack-free material [46].

Besides the crack formation in $\mu\text{c-Si:H}$, it is also important to avoid the formation of pure a-Si:H. This happens often in the first layers of the deposition, and is commonly known as the *incubation zone*. This can have detrimental effects for the performance of solar cells [34], and can be avoided by adjusting the deposition parameters for the first nanometres of $\mu\text{c-Si:H}$.

2.2.3. $\mu\text{c-Si:H}$ vs a-Si:H

In this section, the most important characteristics of $\mu\text{c-Si:H}$ and a-Si will be considered, in order to highlight the individual features of each material.

Optical properties

The optical absorption as a function of energy is presented in Figure 2.17. From the figure, it is evident how a-Si:H has an enhanced optical absorption for high energy photons, but fails to reach the absorption of $\mu\text{c-Si:H}$ for energies lower than around 1.75 eV. This has to do with the presence of a crystalline phase in $\mu\text{c-Si:H}$, which have a lower absorption due to the indirect band gap. The absorption of a-Si:H drops quickly as the energy decreases due to the relatively large band gap of the material, whereas $\mu\text{c-Si:H}$ is still able to absorb more photons. From an optical perspective, $\mu\text{c-Si:H}$ absorber layers need to be made around 10 times thicker to be able to absorb low energy photons.

Electrical properties

The level of disorder present in a-Si:H is much higher than in $\mu\text{c-Si:H}$, which can locally present highly ordered, crystalline structures. For this reason, intrinsic $\mu\text{c-Si:H}$ presents better conduction properties, with dark conductivities of around 10^{-6} Scm^{-1} , compared to around 10^{-9} Scm^{-1} for intrinsic a-Si:H [47]. This enhances the charge transport properties. Moreover, doped $\mu\text{c-Si:H}$ layers also present noticeably higher conductivities when compared to a-Si:H [34], which is why they are often found in doped layers of a-Si:H cells. Both $\mu\text{c-Si:H}$ and a-Si:H cells still need to rely on drift for the carrier collection at the front and back side, which is why they both follow the *pin* or *nip* structure.

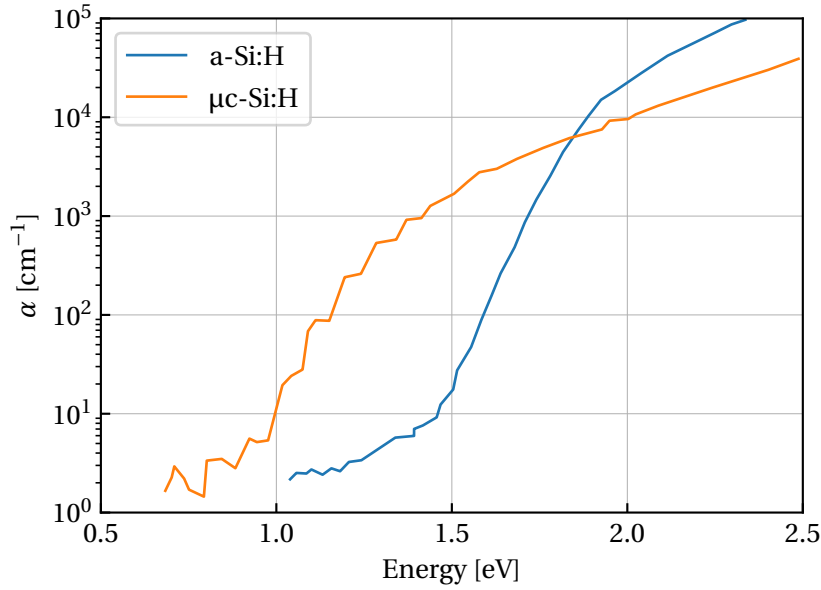


Figure 2.17: Absorption coefficients of a-Si:H and $\mu\text{c-Si:H}$. Adapted from [42].

Stability

As discussed above, the performance of a-Si:H solar cells is compromised after a long exposure to light. This effect does not seem to affect $\mu\text{c-Si:H}$, as firstly observed in 1994 [42]. Despite this advantage, the growth control is more crucial for $\mu\text{c-Si:H}$ than for a-Si:H. Growing thick layers of $\mu\text{c-Si:H}$ without electrical deterioration is a challenge, specially when aiming for high deposition rates [48].

2.3. Tandem devices

Multi-junction solar cells use multiple semiconductor materials simultaneously for an improved light utilization. In the case of *tandem* devices, two solar cells are stacked on top of each other, allowing the impinging light to pass through each cell successively. Preferably, the top and bottom materials have a different band gap [34]. By allowing light to strike the higher band gap material first, the high energy photons are partially absorbed in this subcell, at the same time allowing the photons with an energy below this band gap to pass through. This part of the light spectrum is then available for the second subcell with a lower band gap absorber layer, which is located at the bottom.

The impact of the arrangement of solar cells in a tandem structure on the performance of the device is important to understand its benefits. Effectively, the operation of a tandem solar cell resembles the connection of two solar cells in series. This means that, ideally, the V_{oc} of the tandem corresponds to the sum of the individual open circuit voltages of each subcell:

$$V_{\text{oc}}^{\text{tand}} = V_{\text{oc}}^{\text{top}} + V_{\text{oc}}^{\text{bot}}. \quad (2.17)$$

Moreover, the J_{sc} is limited by the lowest short circuit current of the top and bottom subcells:

$$J_{\text{sc}}^{\text{tand}} = \min(J_{\text{sc}}^{\text{top}}, J_{\text{sc}}^{\text{bot}}). \quad (2.18)$$

If one of the subcells produces a higher current than the other one, this will be lost in the

other subcell, thereby not fully taking advantage of the current produced in the stack. For this reason, it is of utmost important that the subcells produce the same current, a condition that is referred to as *current matching*. Finally, the computation of FF is a difficult task. It is generally said to be located in between the FF of each subcell when the current is matched, and is higher than both when this is not the case [34].

Based on the description of tandem cells provided above, two main advantages over single-junction devices can be identified:

1. *Better spectral utilisation*: the energy of highly energetic photons is exploited by the larger band gap material, such that the generated electron-hole pairs can be extracted at a high voltage difference. If compared to a single-junction, lower band gap material, these high energy electron-hole pairs would quickly thermalise and lose its energy as heat, as described in Section 2.1.5.
2. *Decrease in resistive losses*: as the current delivered by a tandem is lower than single-junction devices because the light spectrum is shared, the ohmic losses decrease as the current is extracted from the cell through the TCO and metal contacts [34]. By delivering power at a higher voltage, less energy is lost to heat.

There are many possible combinations of materials for the creation of tandem solar cells, but certain choices of band gap values can ensure better performances. Increasing the band gap of one of the subcells could ensure a higher combined V_{oc} , but will at the same time produce a lower J_{sc} . This could limit the J_{sc} of the total device, as described above. When considering the case of ideal absorption and current matching between both cells, the combination of a-Si:H as top and μc -Si:H as bottom cell in a tandem device is the optimal band gap combination [49]. This tandem is described in the next section.

2.3.1. Micromorph cell

Micromorph tandem solar cells use a-Si:H and μc -Si:H as top and bottom cells, respectively. In 1994, the same year the first successful μc -Si:H solar cell was created, the same group reported the first a-Si:H/ μc -Si:H device, with an initial efficiency of 9.1 % [50]. This tandem was given the name micromorph (*microcrystalline and amorphous*). The current world record is, again, held by AIST [31]. In 2015, they were able to produce a 1 cm^2 cell with a stabilised efficiency of 12.7 %, given $J_{sc} = 13.45\text{ mAcm}^{-2}$, $V_{oc} = 1.342\text{ V}$ and $FF = 0.702$ [51].

The micromorph cell is considered to be one of the most promising concepts when considering both costs and efficiency [52]. The abundance of silicon and the relatively low processing temperatures greatly reduces the costs. Moreover, a-Si:H and μc -Si:H can be deposited with the same equipment, by varying the deposition conditions. Nonetheless, the presence of a-Si:H still makes it prone to light-induced degradation. Furthermore, careful attention needs to be paid to the layer depositions to ensure uniformity and a proper layer build-up given the high sensitivity of the efficiency to the layers' properties and thicknesses.

Structure

Figure 2.18 presents the structure of a micromorph solar cell. The front and back part of the cell are the same as the example presented in Figure 2.10, and serve the same purpose as described in that section. The difference lies in the absorber layers of the cell. Light passes first through the top a-Si:H cell, after which it has a second opportunity to be absorbed in

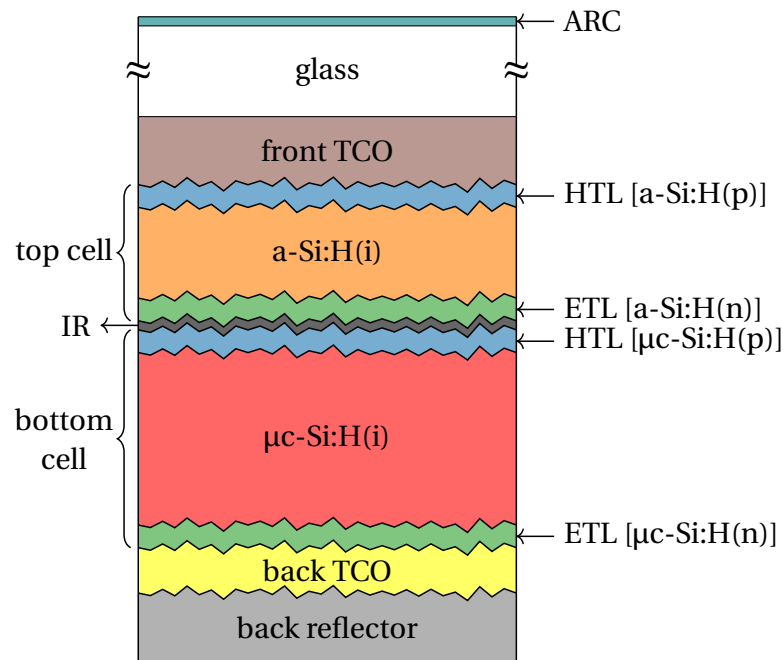


Figure 2.18: Sample structure of a micromorph solar cell. ARC: anti-reflection coating, TCO: transparent conductive oxide, IR: intermediate reflector. The layer thicknesses are not to scale.

the bottom $\mu\text{c-Si:H}$ cell. In the single-junction, the electrons that arrived at the n -doped a-Si:H were directly collected by the back TCO and back reflector, to be used in an external circuit. In the tandem, we see that it is actually the electrons of the $\mu\text{c-Si:H}$ that are being absorbed in these back layers. In the same way, the holes that are being collected from the cell are the ones generated in the top cell and arriving at the p -doped a-Si:H. Two more aspects are worth looking into: the *tunnel-recombination junction* and the *intermediate reflector*.

Tunnel-recombination junction

At the junction between the n -doped a-Si:H and the p -doped $\mu\text{c-Si:H}$, the so-called *tunnel-recombination junction* (TRJ) takes place. It must allow the transport of electrons from the n -doped side and holes from the p -doped side towards each other. At the junction, it should provide a proper environment for these charge carriers to recombine, thereby allowing the flow of current throughout the cell. This can be achieved with a high concentration of states at the interface [24], such that recombination is enhanced, as explained in Section 2.1.5.

The charge carrier transport near the junction is enhanced by the process of *tunnelling*, which allows a particle to overcome a sufficiently low potential barrier. This allows charge carriers to recombine even if they are in the neighbourhood of the interface of the junction. The tunnelling process is improved with a high doping concentration and thin doped layers [24], which effectively lowers the barrier that electrons and holes need to tunnel through. Finally, the reduction in thickness is also important to limit the parasitic absorption across the junction.

This junction has received special attention in multi-junction devices because a proper construction is needed to avoid a drop in the performance of the cell. Several studies report

that the substitution of the n -doped a-Si:H by n -doped $\mu\text{c-Si:H}$ in the TRJ is desirable [53, 54], since $\mu\text{c-Si:H}$ can be more easily doped and presents better electrical properties. As an alternative, the use of a double n - or p -doped layer at the TRJ can have a positive impact. Studies report both the use of double n [55] and p [56] doped layers. Finally, an oxidation process at the interface can help in boosting the number of recombination centres [53].

Intermediate reflector

When comparing the structure of the micromorph cell in Figure 2.18 to the structure of a-Si:H in Figure 2.10, it is notable that the a-Si:H subcell in the tandem case does not have a back reflector to allow light to pass through the top cell again. In turn, this light is allowed to pass through to the bottom $\mu\text{c-Si:H}$ cell. Effectively, this means a reduction of the current produced by the top cell when compared to the single-junction case. This could be counteracted by increasing the thickness of the intrinsic a-Si:H layer, but this has a detrimental effect for the V_{oc} , as the recombination would increase. In order to solve this, a thin layer called *intermediate reflector* (IR) can be introduced to provide a suitable optical environment for the reflection of some of the light, while still allowing the rest to go through to the bottom cell.

Figure 2.19 illustrates the principle of the use of an IR.

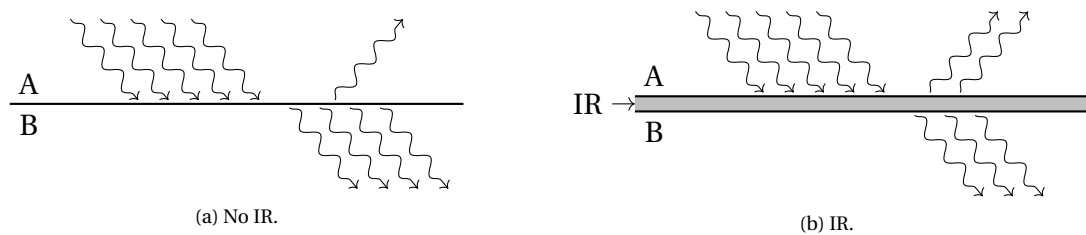


Figure 2.19: Illustration of the reflection and transmission of light a) without an IR and b) with an IR at a junction between materials A and B.

Without an IR, some of the light will be reflected and some transmitted, depending on the optical values of the materials at the junction (see Section 2.1.1). By choosing a material with suitable optical properties, the reflection of some light can be increased to allow the top cell to generate more current at the same thickness. In some cases, the thickness of the intrinsic a-Si:H can even be decreased if sufficient light is absorbed, thereby decreasing the impact of the SWE by enhancing the collection of charge carriers [39]. This can result in an improved current matching for the micromorph cell, since it is the top cell which often limits the total current of the device.

The first use of an IR reported ZnO as a suitable material [57]. Using silicon oxide has also been reported as an adequate IR material [58], which could reduce the thickness of the intrinsic a-Si:H by 40 % [59].

3

Experimental details: device fabrication and characterisation

This chapter focuses on the experimental aspects regarding the manufacturing and characterisation of thin-film silicon devices. To this end, Section 3.1 introduces the deposition processes used for the fabrication of cells, along with insights on the relevant physical and chemical mechanisms taking part. Then, Section 3.2 describes both the roll-to-roll fabrication process used at HyET and the adaptation to a lab-scale setting. Finally, common characterisation techniques are explained in Section 3.3.

3.1. Deposition techniques

Several deposition techniques are used for the fabrication of thin-film devices: PECVD, magnetron sputtering and evaporation. In this section, the physical principles of each deposition technique are introduced and explained.

3.1.1. Plasma-Enhanced Chemical Vapour Deposition

Plasma-Enhanced Chemical Vapour Deposition (PECVD) is often used in the PV field for the deposition of thin-films, given several advantages such as a high quality material depositions at relatively low temperatures [60]. Moreover, it presents the ability of changing the target material properties over a wide range by adjusting the deposition parameters, thereby being able to produce both doped and undoped a-Si:H and $\mu\text{c-Si:H}$ films.

The first thing to consider is the concept of a plasma. A plasma is an ionised gas that is electrically neutral on a macroscopic scale [60]. For PECVD processing, the ionisation is often caused by the action of an electric field provided by capacitively coupled plates, which provides enough energy to free electrons from the atoms forming the gas, commonly known as the precursor gas. This action creates new free electrons, ions and radicals, which preserves the plasma state.

The bulk of the plasma is neutral, but at the boundaries there is a space charge region called sheath boundary [60]. This causes the majority of the electrons to stay confined within the plasma, whereas positive ions reaching the boundary are accelerated away from the plasma. Moreover, neutral radicals are allowed to diffuse through this boundary towards the substrate where the thin film is to be deposited.

For the deposition of a-Si:H and $\mu\text{c-Si:H}$, a combination of SiH_4 and H_2 is used as precursor gases. These molecules are dissociated in the plasma, thereby allowing the creation of several possible Si_aH_b radicals. Chemical reactions within these radicals and the precursor gases determine the generation and annihilation rates of each species, which ultimately defines the steady state concentration of each molecule [61]. In this sense, short-lifetime species such as SiH_2 and SiH have a low concentration in the plasma, and can be distinguished from long-lifetime species like SiH_3 , having one of the highest concentrations of all radicals [61].

Growth of a-Si:H

SiH_3 is the main radical responsible for the growth of a-Si:H. As the SiH_3 diffuses and reaches the substrate, some of the incoming radicals are reflected back towards the plasma. Others interact with the surface of the film in two possible ways: with H at the surface of the film (detaching the H from the surface and creating SiH_4 , thereby leaving a dangling bond) or with a Si dangling bond (such that the radical is attached to the surface given the formed Si-Si bond, resulting in film growth) [61].

Growth of $\mu\text{c-Si:H}$

Along with SiH_3 , H is important for the formation of $\mu\text{c-Si:H}$ films. This is why the input flow of SiH_4 is diluted with hydrogen by adding the precursor gas H_2 . The atomic hydrogen is generated by the plasma and diffuses to the surface of the substrate to attach itself to dangling bonds. This causes the surface to be almost free of dangling bonds. This action, plus the local heating due to exothermic reactions involving hydrogen, is thought to improve the diffusion of SiH_3 to an energetically favourable location, which leads to more ordered structures. These ordered structures serve as nucleation sites for the epitaxial-like film growth that forms the $\mu\text{c-Si:H}$ material [61].

Impact of deposition parameters

Deposition parameters such as the temperature, pressure, power, gas flow rate and composition of the gas all influence the type and quality of the material being deposited. By increasing the power delivered to the capacitively charged plates, a higher electric field is experienced by the plasma. This increases the dissociation rate of the gas, which could lead to higher deposition rates. However, it also leads to a higher ion bombardment, which can damage the structure of the thin film. This can be fixed by increasing the excitation frequency of the plasma, given that the sheath boundary is then decreased and the ion acceleration is reduced [33].

The temperature of the substrate has an influence on the reaction rates at the surface of the film. It influences, among other things, the concentration of defects in the material, as it can result in a variation of the number of dangling bonds to which the SiH_3 can adhere to [61]. An increase in the pressure results in more inelastic collisions between the components of the plasma, which reduces the energy of the ions reaching the substrate. This influences both the optical and electrical parameters of the film [60]. Finally, the concentration of the gases present in the plasma and the different reaction rates will determine the abundance of ions and radicals, which regulate the type of material that is being deposited.

3.1.2. Magnetron sputtering

Magnetron sputtering is one of the most used techniques for the deposition of TCOs such as indium tin oxide (ITO) and aluminium-doped zinc oxide (AZO) because of the relatively high deposition rates and ease of upscaling [60]. Unlike PECVD, sputtering is a type of physical vapour deposition (PVD), since no chemical reactions are involved. The technique is based on the transfer of the required material from the ‘target’ to the substrate by striking it with ions.

This is done by ionizing a gas between two electrodes which provide a sufficiently high electric field, resulting in the creation of a plasma. The ionised particles of the gas (often argon) are then accelerated towards the electrode where the target material is located. The bombardment of ions causes some of the target molecules to be knocked out, after which they reach the surface of the substrate to form the required film.

The *magnetron* sputtering technique includes the addition of a magnetic field between the substrate and the target. This causes the electrons to move in spirals in the plasma, which increases their travelled path and therefore the number of argon atoms that will be ionised [61]. The result is an increase in the deposition rate. As with PECVD, careful attention needs to be paid to the deposition parameters. Ion bombardment at too high energies can lead to a deterioration of the electrical properties of the film [62].

3.1.3. Evaporation

Evaporation is another type of PVD process, in which a target metal is heated above its melting point. Therefore, it turns to a gaseous phase and eventually condenses on the surface of the substrate [8], forming a coating. The heating of the metal can be done thermally or by an electron beam. In the former case, a high current is passed through a resistor to reach the desired temperature. In the latter, an electron beam is emitted and focused using a magnetic field in order to hit the target metal, causing its temperature to rise.

3.2. Device fabrication

In this section, the fabrication of the solar devices is described. The large scale module production done by HyET Solar is explained, along with a downscaling adaptation for the production of cells in a lab environment.

3.2.1. HyET Solar’s R2R processing

At HyET Solar, the production of flexible, thin-film silicon modules is done with a so-called *roll-to-roll* (R2R) manufacturing process. An aluminium roll is used as a temporary carrier on which the active layers are placed, which unrolls at the start of the deposition machines at a constant rate. The roll is 1.4 m wide and is typically several hundred meters long. This is advantageous in terms of processing homogeneity and the possibility of easily scaling up the length of the rolls [63]. The details of the manufacturing process, taken from [63], are described next.

1. *Al foil texturing*: a wet-etching process in diluted NaOH is performed to create crater-like structures that will lead to an enhancement in the light scattering. After the etching, the residues on the Al foil are cleaned in an acidic bath of diluted H₃PO₄ followed by a brush.

2. *Front TCO deposition:* fluorine-doped tin oxide (FTO) $\text{SnO}_2:\text{F}$ is deposited by atmospheric pressure chemical vapour deposition (APCVD) on the textured Al foil for its use as a front TCO. The use of the Al carrier allows a deposition temperature of about 500°C , at which a 700 nm thick layer of high-quality material is deposited.
3. *Silicon deposition:* the doped and intrinsic silicon layers are deposited by plasma-enhanced chemical vapour deposition (PECVD) in a superstrate structure at an RF frequency of 13.56 MHz and a temperature of 200°C . The deposition machine consecutively deposits a *p*-doped, intrinsic and *n*-doped a-Si:H, such that the active layer stack is complete after one pass in the machine. In the case of a tandem product, a second pass is necessary.
4. *Interconnection:* with the use of laser scribing, the cells conforming a module are monolithically interconnected. This involves a scribe penetrating through the FTO and a-Si:H layers, after which it is filled with an isolating glue to separate the adjacent cells electrically. A second scribe goes only through the a-Si:H layers and will connect the *n*- and *p*-doped layers of adjacent cells during the deposition of the back contact, which will ensure a series interconnection. Finally, a lift-off ink is deposited next to the latter scribe. This will help in breaking the connection of the back contacts of the different cells.
5. *Back contact deposition:* a back contact of AZO/Al is deposited by sputtering, with typical thicknesses of 80 nm and 300 nm, respectively. This back contact fills the unfilled laser scribe and covers the lift-off ink, both described in the previous step. After dipping the back contact in a solvent and brushing, the rough structure at the lift-off ink causes it to detach from the cell, thereby removing the back contact at this site and discontinuing the back contact to ensure the cells are isolated.
6. *Permanent carrier:* in this step, the stack of layers is transferred to the permanent carrier of the module. This material, a polymer, ensures the flexibility is maintained and provides an encapsulation from the back.
7. *Removal of Al substrate:* with a similar wet-etching procedure as for the texturing of Al in the first step, this layer is now completely etched away, since this is the side of the module where light will enter. A visual inspection ensures all the Al from the foil has been removed.
8. *Encapsulation:* in this final step, the modules are cut to size and encapsulated from the front side. After adding the electrical connectors, the product is ready.

With this procedure, both a-Si:H and a-Si:H/ μc -Si:H can be produced. The final modules are composed of 28 cells, each with an area of $591 \times 1 \text{ cm}^2$ [64, 65].

3.2.2. Lab-scale processing

The R2R processing at HyET Solar described in Section 3.2.1 is scaled down to a lab setting for its application in the TU Delft facilities. Al foil samples of $10 \times 10 \text{ cm}^2$ are provided by HyET Solar, which are cut from the same roll used in their production. Some processing steps are adapted to accommodate for the available equipment at the Else Kooi Laboratory (EKL). These are described next.

Temporary Al substrate texturing

Wet-etching is a widely used technique for the texturing of solar cell substrates, which increases the light capture and enhances scattering. Either alkaline [66] or acidic solutions [67] are used for this purpose, thereby roughening the surface where the layers of the cell will be deposited. The idea is that the surface morphology is adapted by all layers to create a scattering effect at each material interface.

As with the R2R production, an alkaline solution is used for the texturing of the $10 \times 10 \text{ cm}^2$ Al foils. In this case, a potassium hydroxide (KOH) solution is used. The resulting morphology is highly dependent on the temperature of the etching bath, the concentration of the solvent and the etching time. The optimisation of these parameters was performed by D. Rajagopal [68] within the framework of FlamingoPV. The best texturing was chosen such that light is scattered efficiently, while at the same time ensuring proper growth conditions for the silicon layers.

This was achieved by etching the Al foils for 2 minutes at a temperature of 70°C in a 10 % solution of KOH diluted in water. After this step, the foils were cleaned in a 1 % diluted in water phosphoric acid (H_3PO_4) solution, at the same temperature. This was needed for the removal of the etching residues. Finally, the substrates are dried with a N_2 gun.

To give an indication of the surface morphology, a recreation of an AFM scan of an Al foil textured with the conditions described above is shown in Figure 3.1. Such a texturing results in a *root mean square* (RMS) roughness of about 418 nm and a correlation length of $5.235 \mu\text{m}$. The resulting modulated surface texture (MST) provides a suitable growth both for a-Si:H and $\mu\text{c-Si:H}$ layers.

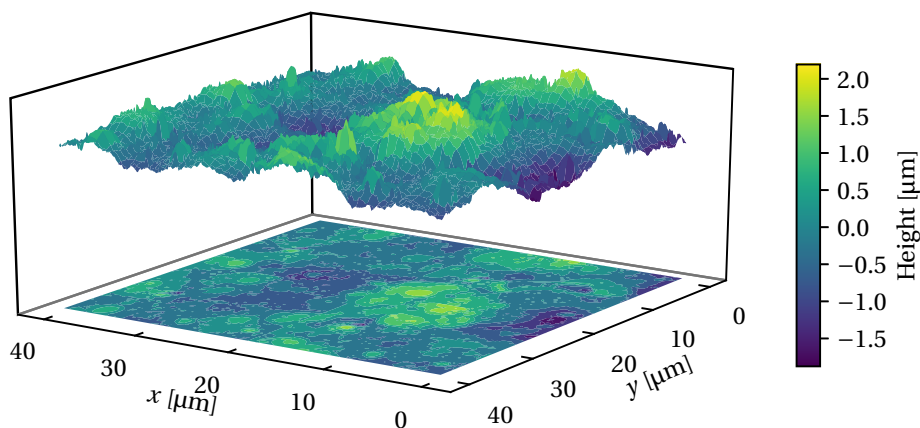


Figure 3.1: Sample AFM scan of a textured Al foil.

Layer depositions

Prior to the layer depositions, the textured foils are cleaned in consecutive ultrasonic baths of acetone and isopropyl alcohol (IPA) for 10 minutes each. After proper drying with a N_2 gun, the foils are ready for deposition.

A multi-chamber cluster tool named *AMIGO* is used for the deposition of the front TCO and silicon layers. It is composed by six deposition process chambers (DPC). The first five are for thin-film processing by PECVD, whereas the last one is used for sputtering deposition of AZO. The DPCs are connected by a cylindrical transfer chamber (TC) located in the

middle, which is equipped with a robot arm for the transfer of the deposition substrates. All the DPCs and the TC are pumped down to vacuum. Finally, a load lock chamber (LLC) allows the interaction with the outside for the addition of new substrate holders or the removal of finished depositions, with a total of 5 slots.

The first layer to be deposited is the front TCO which, unlike the R2R production at HyET Solar, is formed of AZO. To this end, the magnetron sputtering chamber DPC6 is used, powered by a radio-frequency (RF) generator at 13.56 MHz. The deposition of doped and undoped a-Si:H layers is also at RF, whereas very-high frequency (VHF) is used for the $\mu\text{c-Si:H}$ layers at 40.68 MHz. DPC1 is used for *p*-doped materials by adding diborane (B_2H_6) as one of the precursor gases, DPC2 for *n*-doped materials by adding phosphine (PH_3) and DPC3 and DPC4 for intrinsic a-Si:H and $\mu\text{c-Si:H}$, respectively.

The area of the electrodes is $12 \times 12 \text{ cm}^2$. The grounded electrode is the top one, on which the substrate is placed. The gas inlet is mounted at the bottom electrode, which has multiple holes closely packed for a uniform gas injection and a stable plasma over the whole surface of the electrode. For the layer depositions, the standard recipes were used. The most important parameters for each layer are defined in Table 3.1.

Table 3.1: Summary of the deposition conditions of the layers used in the fabrication of a-Si:H and $\mu\text{c-Si:H}$ cells. The values are taken from the standard recipes defined for the AMIGO cluster tool. *: 2 % in H_2 . **:200 ppm in H_2 .

Layer	Power [W]	Pressure [mbar]	T [°C]	Gas	Flow rate [sccm]
AZO	300	2.6	300	Ar	20
a-SiC:H(p)	12	2.2	300	SiH ₄ CH ₄ B ₂ H ₆ * H ₂	0.8 2.3 20 170
a-Si:H(i)	2.8	0.7	300	SiH ₄	40
a-SiO _x :H(n)	11	1.6	300	SiH ₄ PH ₃ H ₂ CO ₂	1 1.2 100 2
$\mu\text{c-SiO}_x\text{:H(p)}$	12	2.2	300	SiH ₄ B ₂ H ₆ ** CO ₂ H ₂	0.8 10 1.6 170
$\mu\text{c-Si:H(i)}$	40	4	180	SiH ₄ H ₂	3.5 120
$\mu\text{c-SiO}_x\text{:H(n)}$	11	1.5	300	SiH ₄ PH ₃ H ₂ CO ₂	1 1.2 100 1.6

Back reflector

The back contact/reflector is deposited by means of electron-beam evaporation using a PROVAC PRO500. The metal to be evaporated is located at the bottom and multiple cells can be placed on a rotating disc at the top, ensuring a homogeneous deposition. With this procedure, 300 nm of Al is deposited to serve both as a back contact and a reflector.

Post-processing

After all the layers of the solar cell have been deposited, some processing is needed before the device performance can be tested. These steps are performed at the lab facilities of HyET Solar. In the same way as the roll-to-roll processing is done, the cell needs to be transferred to a permanent carrier. This is done by gluing a polymer with epoxy to the back contact in a heated press. Then, a partial etching of the temporary Al foil is done. Around 80 % of the total thickness is etched in a NaOH solution at 70 °C, in order to leave some of the Al for the busbars. After this, a thermal annealing step at 170 °C for 20 minutes is needed to release mechanical stresses in the cell. Following this, etching-resistant tape is placed at the stripes of the busbars and the final 20 % of Al is etched away in the same NaOH bath. The final result is a set of 4 cells, each with an area of $5 \times 1 \text{ cm}^2$.

3.3. Characterisation techniques**3.3.1. Material characterisation: Raman spectroscopy**

Raman spectroscopy is an optical characterisation technique used to investigate the structure and chemical composition of a material [69]. When illuminating a material with light, most of the incident photons will scatter elastically (Rayleigh scattering), which means the frequency of the photons after scattering is unchanged. A very small fraction of the photons will scatter inelastically (Raman scattering), such that a shift in the energy of the photon occurs after the interaction. This is a consequence of the exchange of energy between the incoming photon and molecular vibrations of the material, known as phonons. The amount of energy exchanged with the phonon depends on the vibration frequency of the molecular bond [69].

By analysing the intensity of the scattered spectra for different energy shifts, an indication of the relative abundance of vibration modes of different frequencies is obtained. These vibration modes can be compared to known frequencies of molecular bonds, thereby revealing the chemical structure of the material. The frequency of the shifted energy is often expressed in terms of the wavenumber (in units of cm^{-1}).

In this work, this technique is used to give an indication of the crystallinity of a deposited silicon sample. Crystalline silicon, being a highly ordered material, presents a sharp Raman peak at a shift of 521 cm^{-1} . On the other hand, a disordered amorphous silicon material has a wide range of bond angles, lengths and energies, resulting in a broader spectrum with a main mode centred at 480 cm^{-1} [70]. The intensity of each peak is proportional to the concentration of the material in the sample. Figure 3.2 depicts the normalised spectrum of an amorphous, a microcrystalline and a crystalline silicon layer.

The fraction of crystalline material can be computed with Equation (3.1):

$$X_c = \frac{I_c}{I_c + \gamma I_a}, \quad (3.1)$$

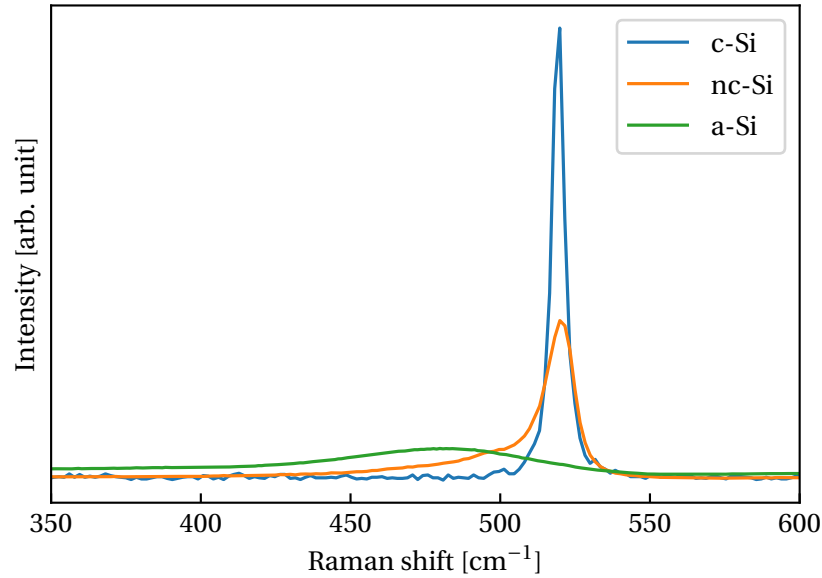


Figure 3.2: Raman spectra of crystalline, microcrystalline and amorphous silicon layers. The spectra are normalised such that the area under each curve is the same.

with X_c the crystalline fraction, I_c and I_a the intensities of the scattering peaks of crystalline and amorphous silicon, respectively, and γ the ratio of cross sections between crystalline and amorphous silicon. The latter quantifies the difference in probability for a scattering event between the different materials and is often set to 0.8 [71]. The intensities of the scattering peaks for crystalline and amorphous material are often quantified by integrating fitted Gaussian curves centred at 521 cm^{-1} and 480 cm^{-1} , respectively. In Figure 3.2, the depicted microcrystalline spectrum corresponds to a crystallinity of around 80 %.

3.3.2. Performance characterisation: I-V characteristic and EQE

The $I - V$ characteristic of a solar cell is usually measured under Standard Test Conditions (STC): AM1.5 spectrum (1000 W m^{-2}) at a constant device temperature of $25 \text{ }^\circ\text{C}$. A solar simulator is used to approximate the required light spectrum, which is often achieved by superimposing a halogen and a xenon lamp and the use of appropriate filters. Before a measurement, the spectrum is calibrated with reference solar cells in order to ensure a consistent spectrum. Then, the current at different voltage biases is measured. This gives the so-called $I - V$ curve, from which performance indicators of the solar cell can be retrieved, as explained in Section 2.1.4.

The external quantum efficiency is measured by considering the impact of photons at a specific wavelength on the current delivered by the cell. This is done by using a monochromator to filter photons in a narrow band from a broad spectrum light, such as the one produced by a xenon lamp [8]. This monochromatic light is chopped with a certain frequency, after which it is shone on the cell. The small perturbation in the current of this chopped light is measured with a lock-in amplifier, such that the contribution to the current from this signal is isolated. Moreover, the photon flux of the monochromatic light is measured with a calibrated photodiode. The ratio between the current and the flux, scaled with the inverse elementary charge $1/q$, is the EQE. Often, white light is superimposed to

the monochromatic light to ensure a similar cell operation as under STC, which has an impact on the charge carrier occupation distribution [34].

When measuring the EQE of a tandem device, the response of each subcell is not directly measured as in the single-junction case. This has to do with the fact that the total current of the device is limited by the lowest current of the two subcells. Therefore, if the response of subcell 1 is to be measured, it must be ensured that this is the cell with the lowest current, such that it will dominate the response of the total device. This is often achieved by applying a bias light to subcell 2. The wavelength of this light is chosen such that it only triggers a response in subcell 2, and produces a current that is higher than the one in subcell 1. The same principle holds when measuring the EQE of subcell 2.

4

Thin-film modelling: ASA

This chapter introduces the thin-film semiconductor modelling performed with ASA. Section 4.1 starts with an introduction of the simulation package, followed by a description of the optical and electrical modelling in Section 4.2. Then, Section 4.3 illustrates the possibilities within ASA with a sample simulation file and its output. An automation routine for the optimisation of simulation uploading to the ASA web interface, given the name *autASA*, is presented in Section 4.4. Finally, a sensitivity analysis of the solar cell performance on the model parameters is carried out in Section 4.5, followed by its use in the calibration of the model for reference a-Si:H and $\mu\text{c-Si:H}$ solar cells.

4.1. Introduction

The modelling of solar cells has proven to be an essential tool in the field [72]. By describing the optical and electrical properties of a solar device in a model, accurate predictions can be made, along with the analysis of aspects that could be improved to further increase the performance. The insights obtained with a simulation can then be used as a starting point for the actual fabrication of a solar device. Modelling is specially useful when attempting to match the currents of different subcells in a multi-junction device [39], which would otherwise be an expensive and time-consuming experimental task. Moreover, the impact of the change of model parameters can readily be observed, and the results of the simulations can provide insights into non-measurable quantities.

Advanced Semiconductor Analysis (ASA) is a simulation program developed for the modelling of amorphous and crystalline semiconductors [73], from Delft University of Technology. Its opto-electronic simulation capabilities allows for the numerical computation of both the optical and electrical components, which are necessary for the prediction of the operation of a solar cell. It is a 1D steady-state device solver, which includes a complete description of the DOS as a function of energy, optical models for the calculation of the absorption profile with textured interfaces and a model for the tunnel-recombination junction [73], among others.

Given the completeness of ASA for thin-film simulations, it is used in this work for the modelling of single-junction a-Si:H and $\mu\text{c-Si:H}$ cells, along with the inclusion of both materials in a micromorph device. The physical models and the use of ASA for this work are described next.

4.2. Description of the model

4.2.1. Optical modelling

In order to simulate the absorption of light in a solar device, advanced optical models are needed. This becomes increasingly difficult with the introduction of textured interfaces to increase the optical path length, which is a fundamental requirement for thin-film devices. To this end, the optical properties of the layers forming the solar device and the morphology of the interfaces should be included for an accurate description of the optical model [73].

As a first approximation, the equations presented in Section 2.1.1 can be used to compute the photo absorption, making use of Lambert-Beer's law for the absorption in a layer and Fresnel's coefficients for the behaviour of light at an interface. This model is available in ASA, but does not take into account the texturing of interfaces, which is why the more advanced optical absorption model *GenPro3* is used. Building up from *GenPro1* and *GenPro2*, *GenPro3* introduces a semi-coherent treatment of light [73].

When light reaches a textured surface, its reflected and transmitted parts will decompose in a *specular* and a *diffuse* component, depending on the morphology of the interface. The specular component is the non-scattered one, which will continue the path of the incoming light. This type of transmitted or reflected light is considered to be *coherent* given that the phase of the wave is maintained, such that interference effects may appear. On the other hand, the diffuse component appears as a consequence of the scattering of light from the angled planes that form the rough texture, transmitting and reflecting light over a wide range of angles. This light is treated as *incoherent* and cannot form interference fringes.

In *GenPro3*, the specular and diffuse component of light are treated as described above. The fraction of incoming light that is scattered is called *haze*, which is computed both for the reflected and transmitted light. This is done using the scalar scattering theory, which describes light with a complex scalar field [73]. The angular intensity distribution (AID) is also computed using this approach.

For the characterisation of the interface textures of the fabricated cells, AFM scans are used. A typical profile can be seen in Section 3.2.2. The height functions of the AFM scan are provided to *GenPro3*, with which it is able to compute the haze and angular distribution functions. Based on this, absorption profiles as a function of wavelength and position can be computed. By integrating with the desired light spectrum, the optical generation rate G_{opt} can be calculated.

4.2.2. Electrical modelling

Given the steady-state, one-dimensional treatment used in ASA, the semiconductor equations that describe the physical phenomena during the operation of a solar cell can be simplified. Starting from the Poisson equation, the continuity equation for electrons and holes and their respective current densities, the assumptions made lead to the following set of

equations [73]:

$$-\rho = \frac{d}{dx} \left(\epsilon \frac{d\phi}{dx} \right), \quad (4.1)$$

$$0 = \frac{1}{q} \frac{dJ_n}{dx} + G_{\text{opt}} - R_{\text{net}}, \quad (4.2)$$

$$0 = -\frac{1}{q} \frac{dJ_p}{dx} + G_{\text{opt}} - R_{\text{net}}, \quad (4.3)$$

$$J_n = qD_n \frac{dn}{dx} + \mu_n n \left[-q \frac{d\phi}{dx} - \frac{d\chi}{dx} - \frac{k_B T}{N_C} \frac{dN_C}{dx} \right], \quad (4.4)$$

$$J_p = -qD_p \frac{dp}{dx} + \mu_p p \left[-q \frac{d\phi}{dx} - \frac{d(\chi + E_g)}{dx} + \frac{k_B T}{N_V} \frac{dN_V}{dx} \right], \quad (4.5)$$

with ρ [Ccm^{-3}] the space charge density, ϵ [$\text{CV}^{-1}\text{cm}^{-1}$] the permittivity, ϕ [V] the electric potential, q the elementary charge ($1.602 \cdot 10^{-19}$ C), J_n and J_p [$\text{Ccm}^{-2}\text{s}^{-1}$] the electron and hole current density, respectively, G_{opt} [$\text{cm}^{-3}\text{s}^{-1}$] the optical generation rate, R_{net} [$\text{cm}^{-3}\text{s}^{-1}$] the net recombination-generation rate, D_n and D_p [cm^2s^{-1}] the electron and hole diffusion coefficient, respectively, n and p [cm^{-3}] the free electron and hole concentrations, respectively, μ_n and μ_p [$\text{cm}^2\text{V}^{-1}\text{s}^{-1}$] the electron and hole mobility, respectively, χ [eV] the electron affinity, k_B the Boltzmann constant ($8.617 \cdot 10^{-5}$ eVK $^{-1}$), T [K] the temperature, N_C and N_V [cm^{-3}] the effective density of states in the conduction and valence band, respectively, and E_g [eV] the band gap energy.

Physical interpretation of model equations

Equation (4.1) represents Gauss' law, one of Maxwell's equations. It accounts for the impact of a given space charge density distribution ρ on the formation of an electric potential ϕ . For an amorphous material, ρ can be written as

$$\rho = q \left(p - n + p_{\text{loc}} - n_{\text{loc}} + N_d^i - N_a^i \right), \quad (4.6)$$

with p_{loc} and n_{loc} the concentration of localised holes and electrons, respectively, and N_d^i and N_a^i the concentration of free, ionised donor and acceptor atoms, respectively, all in cm^{-3} [74]. In contrast to crystalline silicon, not all dopant atoms are ionised at room temperature. N_d^i has a positive sign because, if the electron of a donor atom has been ionised, it leaves behind an atom that has a net positive charge. The same analysis explains the negative sign for N_a^i .

Equations (4.2) and (4.3) quantify the conservation of electrons and holes in a steady-state condition. By considering a differential, one dimensional volume, any difference between the optical generation rate and the net recombination-generation rate in this volume is compensated by an inflow or outflow of electrons or holes, represented by the current densities J_n and J_p , respectively. This ensures that the number of electrons and holes is constant with time, allowing for a steady state operation.

The physical phenomena that can result in a movement of electrons or holes, thereby generating current densities J_n and J_p , are described in Equations (4.4) and (4.5). The first term in the right-hand-side of these equations represents a diffusion current, allowing for the transport of charge carriers when a concentration difference is present in the spatial

dimension x . The second term, on the other hand, accounts for the drift current as a consequence of the spatial electrical properties.

In the square brackets, the terms represent the presence of an electric field described by the spatial variation of the potential ϕ , a band edge energy misalignment and a difference of the effective density of states at the band edges for the respective transport bands. In the case of electrons, the misalignment of the conduction band is quantified by the variation of the electron affinity χ , whereas the band gap energy E_G is also included for the holes to account for an added difference in valence band edge energies this may cause. All these terms are proportional to the concentration of charge carriers and their mobilities, represented in the pre-factor of the square brackets.

Density of states

To accurately describe the availability of electronic states in amorphous silicon, ASA uses the so called *DOS model*, which takes into account the quasi-continuous density of states present in a-Si:H. This was shown in Figure 2.15. In order to model the extended states, the conduction and valence band are described as a parabolic function of energy, as typically done with c-Si. The localised states have two components: the band tails and the dangling bonds. The band tails are modelled with an exponentially decaying function, each with its characteristic energy. Given that a dangling bond can have either a positive, negative or neutral charge state, it can be seen as the superposition of a donor-like and an acceptor-like state [74]. This is modelled as two Gaussian distributions of equal width in the gap, whose centres are separated by the so-called *correlation energy*.

It is assumed that the mobility of the localised states is zero [74], such that all electron transport occurs above the conduction band edge and hole transport below the valence band edge.

Recombination

Unlike c-Si, the defects in the gap of an a-Si semiconductor are continuous, which gives a continuous recombination rate as a function of energy. Assuming the localised states are non-interacting, the contribution of all recombinations centres can be obtained by integrating over the energy of the gap states [73].

The conduction and valence band tail states can be interpreted as single-level states, which are neutral or either negative or positive, respectively, for each tail. These charge states can be achieved by the emission or capture of electrons or holes. Given that each energy level can be considered a trap state for charge carriers, the theory of Shockley-Read-Hall recombination can be used, which was presented in Section 2.1.5. Therefore, the recombination rate for the tail states is proportional to the emission and capture coefficients of electrons and holes, their concentrations and the number of states available at the studied energy. After discretisation, the total contribution of these states is found by adding over the rates over the discretised energy levels, obtaining the total recombinations rates R_{VB} and R_{CB} . Moreover, the concentration of electrons and holes in the conduction and valence band tails, respectively, is computed by considering the Fermi-Dirac distribution at each energy level, thereby obtaining the localised charge concentrations n_{loc}^{CB} and p_{loc}^{VB} .

The approach is different for the computation of the recombination rate in the dangling bonds, given that each state can have three possible energy levels. Here, the Sah and Shockley multilevel statistics need to be used [74]. Similarly to the Shockley-Read-Hall case,

emission and capture rates of electrons and holes are considered, this time with respect to two energy levels (represented by the two Gaussian distributions in the DOS described above). Occupation functions are formulated for the three energy states and the total contribution is computed by summing over the discrete energy states. This provides us with the recombination rate of the dangling bonds R_{DB} , and the concentration of electrons and holes in these states: $n_{\text{loc}}^{\text{DB}}$ and $p_{\text{loc}}^{\text{DB}}$, respectively.

The net recombination-generation rate R_{net} present in Equations (4.2) and (4.3) is computed by adding the contributions of both tail states and the dangling bond states [73]:

$$R_{\text{net}} = R_{\text{VB}} + R_{\text{CB}} + R_{\text{DB}}. \quad (4.7)$$

In a similar way, the localised charge concentrations p_{loc} and n_{loc} in Equation (4.6) are given by

$$p_{\text{loc}} = p_{\text{loc}}^{\text{VB}} + p_{\text{loc}}^{\text{DB}}, \quad (4.8)$$

$$n_{\text{loc}} = n_{\text{loc}}^{\text{CB}} + n_{\text{loc}}^{\text{DB}}. \quad (4.9)$$

Tunnel-recombination junction

For junctions at the boundary of two cells in the modelling of a tandem device, the so-called *Delft model* is used. This uses the *trap-assisted tunnelling* model at such junctions, which is based the Shockley-Read-Hall recombination formula and enhances the concentration of charge carriers in the presence of high electric fields [73], thereby favouring recombination. Moreover, at regions of high electric field, charges are allowed to tunnel through localised states by defining an effective mobility [73]. In the normal model, these states would otherwise have a zero mobility given their local nature. This model is only active for the layers comprising the tunnel-recombination junction: n -doped a-Si:H and p -doped $\mu\text{c-Si:H}$.

Solving the model

The electrical description of the modelling in ASA has been described above. To solve Equations (4.1)-(4.6), ASA solves for the electric potential ϕ and the free carrier concentrations n and p [73]. The boundary conditions for this set of coupled differential equations need to be given at the front and back of the electrical stack of layers. To this end, ideal ohmic contacts are chosen. This assumes a perfect collection of charge carriers by setting an infinite surface recombination at the boundaries and a neutral charge [73]. Finally, finite difference models are implemented for the numerical computation of the solution. For more information on the numerical solution methods, consult the ASA manual [73].

4.3. Sample simulation and input file

In order to illustrate the functionalities of ASA, a sample input file is considered, along with the most important results of the simulation of a *pin* a-Si:H single-junction cell. The electrical and optical parameters are defined in a *.cas* file. Specific characterisation of materials can be included by providing *.in* input files during the simulation, such as to indicate the complex refractive indices of the materials or the texture of an interface. In this section, the *.cas* file presented in Appendix A.1 is run in ASA. This is the default amorphous silicon simulation file for ASA.

Simulation structure

The structure of the cell can be seen in Figure 4.1.

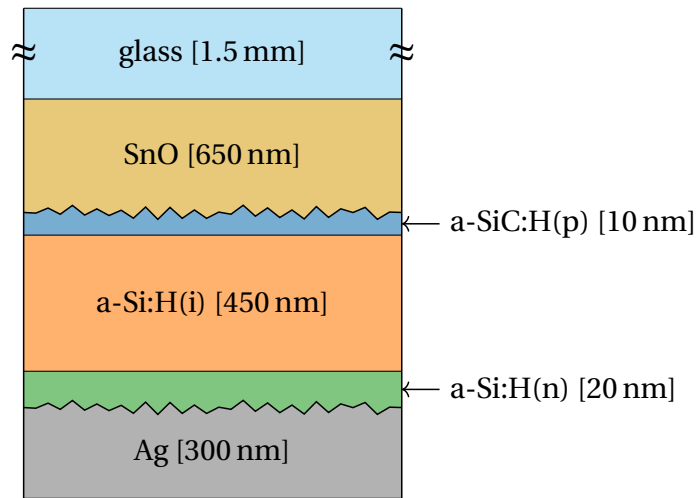


Figure 4.1: Simulation structure used as reference for the modelling of a-Si:H. The layer thicknesses are not to scale.

The interfaces that are textured in this default example are indicated in the figure. The front layers (glass and SnO) and back layer (Ag) are modelled only optically, whereas the three silicon layers are modelled opto-electrically. This is a common approach and will be used throughout this work.

$J - V$ curve

As a first characterisation of the cell, a $J - V$ plot can be made. This plot is shown in Figure 4.2.

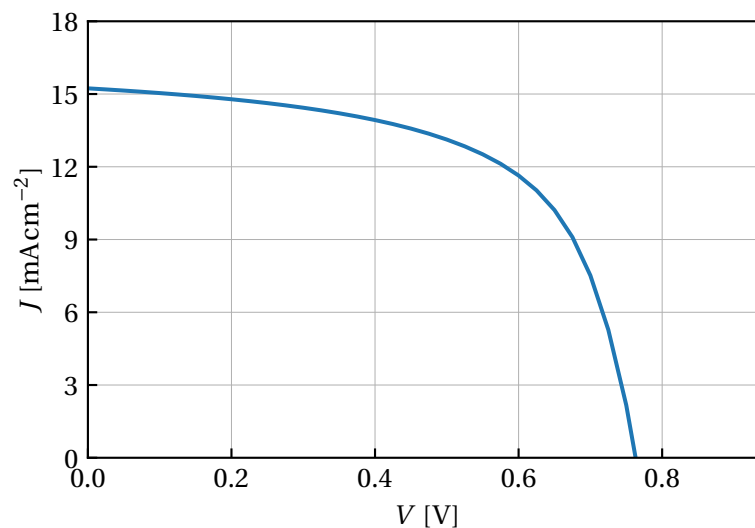


Figure 4.2: $J - V$ curve of the simulation of the reference a-Si:H cell.

From this curve, the different operating conditions of the cell can be examined. Important performance values like the V_{oc} and the J_{sc} can be extracted from the x - and y -axis

intercepts, respectively. Moreover, the maximum power point, as defined in Section 2.1.4, can be determined, along with the fill factor FF and the efficiency η . All these values are summarised in Table 4.1.

Table 4.1: Performance parameters of the reference a-Si:H pin simulation.

Simulation	V_{oc}	V_{MPP}	J_{sc}	J_{MPP}	P_{MPP}	FF	η
	[V]		[mAcm^{-2}]		Wm^{-2}	[-]	[%]
a-Si:H	0.763	0.591	15.23	11.83	69.91	0.60	6.99

EQE

In order to check the response of the cell for different photon wavelengths, an EQE curve can be constructed, as seen in Figure 4.3.

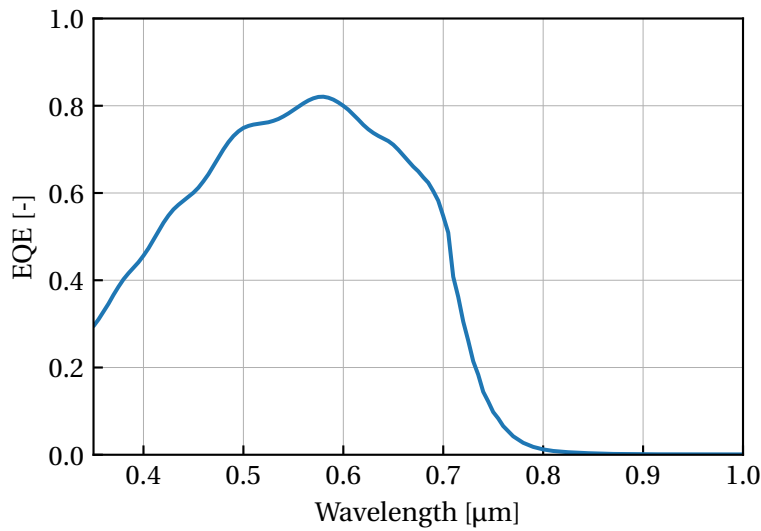


Figure 4.3: EQE curve of the simulation of the reference a-Si:H cell.

The presence of interference fringes is slightly noticeable, and has to do with the texturing of the interfaces. As many of the interfaces have not been textured, the specular component of light still plays a role, which due to its coherence is susceptible to interference effects. The highest response is seen to be at around 580 nm. In order to analyse the optical reasons for the decreased response outside this range, a plot of the absorption per layer can be made, as seen next.

Absorption per layer and total reflection

Figure 4.4 shows the absorption per layer and the total reflection of the device as a function of photon wavelength.

For low wavelengths, there is a high absorption in the layers where light has passed before reaching the intrinsic a-Si:H layer, specially the a-SiC:H(p) layer. This energy is lost as parasitic absorption. For higher wavelengths, this parasitic absorption also takes place, specially in the SnO and the Ag back reflector. As a consequence of the band gap of a-Si:H,

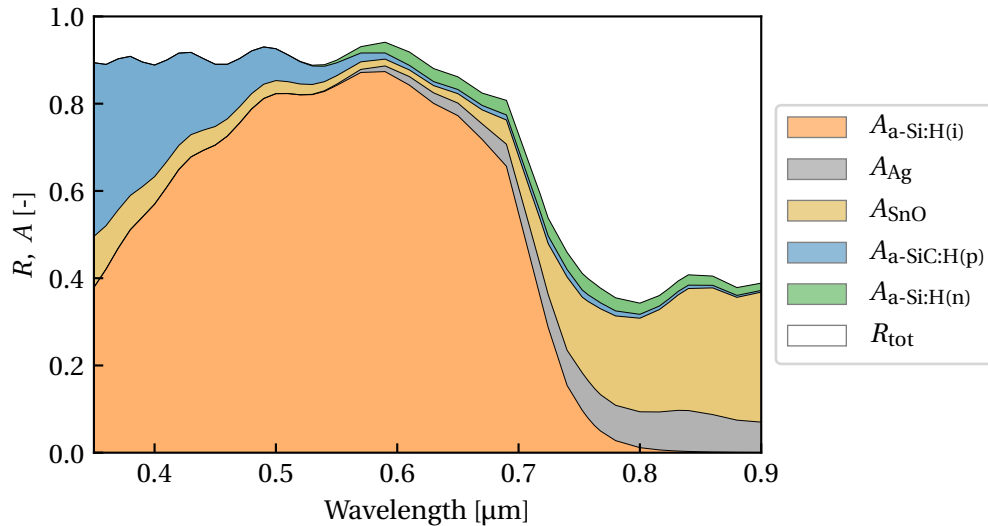


Figure 4.4: Absorption per layer and total reflection as a function of photon wavelength of the simulation of the reference a-Si:H cell. The colours are the same for each layer in the structure of the cell in Figure 4.1.

no more light is absorbed beyond a certain wavelength, and remains largely available for other layers to be absorbed, as can be seen beyond 800 nm. Finally, all light that is not absorbed is reflected, given the nearly zero transmittance of the back reflector. This total reflection is a consequence of the refractive index mismatches along the different layers of the stack, which causes some of the incoming light to return.

4.4. Automating ASA: autASA

Having considered the capabilities of the modelling of solar cells in Section 4.3, the optimisation of a cell can now be considered. This is normally done by running a large number of simulations where parameters are changed independently. Then, the impact of the variation of each parameter on the performance of the device can be analysed and understood, giving the user an indication of the ideal parameters to be used in an experimental framework. For this work, the web interface of ASA was used to access the modelling software. The process of running a vast number of simulations in such an environment is time-consuming and often error-prone.

Given the extensive number of simulations that needed to be run for this work, an automation routine was implemented in Python to speed up the upload and analysis of the results of simulations in the web interface of ASA. The main features and working principles of this routine, given the name *autASA*, are explained next.

4.4.1. Directory structure

The directory structure for the use of *autASA* is shown in Figure 4.5.

Directories

- *cas*: all the simulation files describing the optical and electrical characterisation of the cells are placed in this directory. All files must have a *.cas* extension.

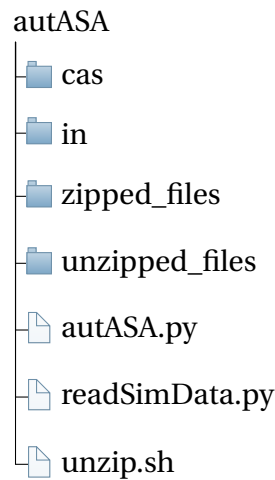


Figure 4.5: Directory tree and necessary files to run autASA.

- *in*: the input files necessary to run the simulations are placed in this directory, such as complex refractive indices of materials or interface texturing profiles. This set of input files should be the union of the input files required by the files in the *cas* directory. All files must have a *.in* extension.
- *zipped_files*: directory where the results of the simulations will be downloaded into in a zipped format from the web interface of ASA.
- *unzipped_files*: directory where the files from the folder *zipped_files* will be unzipped into. Each simulation file in the *cas* directory will have a corresponding folder with the same name as the input file, where the output of the simulation is placed.

Files

- *autASA.py*: main python code that runs the automation routine. It makes use of *Selenium Python* to access the functionalities of *Selenium WebDriver*, which is a framework able to interact with a browser and send a series of commands without having to manually control the actions.
- *unzip.sh*: bash code called within *autASA.py* to unzip the files in the *zipped_files* directory into the *unzipped_files* folder, ensuring the proper unzipped directory names are chosen.
- *readSimData.py*: python code used to process the unzipped output of the simulations. It is called within *autASA.py*, and is given a keyword in order to indicate the desired parameter to be plotted.

4.4.2. Code execution flowchart

The logical structure of the automation routine implemented in *autASA.py* is described in the flowchart of Figure 4.6.

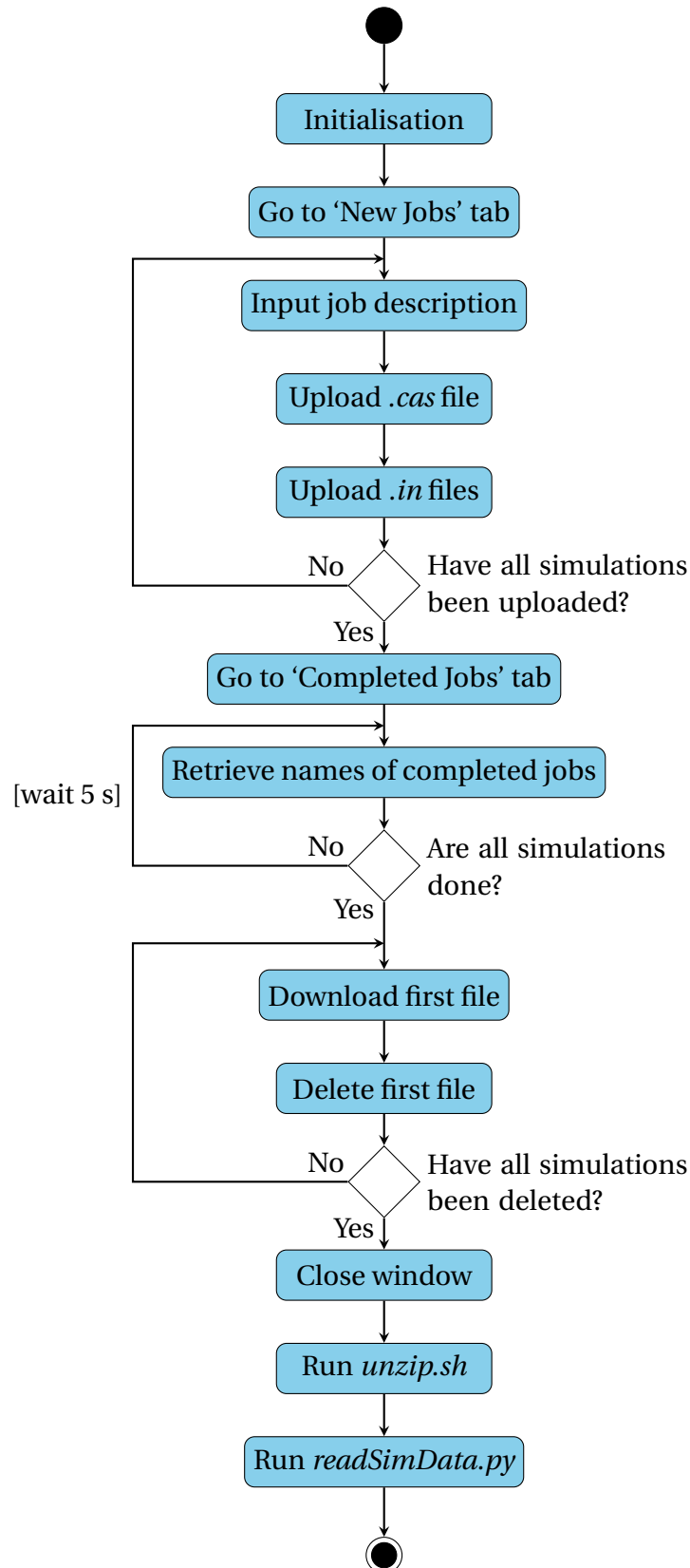


Figure 4.6: Flowchart of the automation routine implemented in *autASA.py*.

Some of the actions mentioned in the blocks of Figure 4.6 are described below.

- *Initialisation*: this step involves starting the webdriver (Chrome) and accessing the url `https://asa.ewi.tudelft.nl/login`. The login details should be defined in `autASA.py` in order to access the simulation program. Once the user is logged in, the program deletes all old simulations in the ‘Completed Jobs’ tab.
- *Input job description*: the job description is retrieved from the `cas` file basename (without the `.cas` extension). This, along with the upload of the `.cas` and `.in` files, is done for each file in the `cas` directory.
- *Retrieve names of completed jobs*: this action is done by looping through all the rows in the table that is generated in the ‘Completed Jobs’ tab. The set of all completed job descriptions is compared to the set of files uploaded at the beginning in order to determine if all the simulations are done.
- *Run readSimData.py*: when running this script, the user is asked to input the desired parameter to be plotted of the recently downloaded simulations. The options are V_{oc} , V_{MPP} , J_{sc} , J_{MPP} , P_{MPP} , FF and efficiency. Moreover, the EQE and $J - V$ curves can be displayed.

With the above algorithm, it takes about 3 s for the browser to open and to log in, 3 s for a job to upload and about 2.5 s for a job to be downloaded and deleted. All these times include the loading time of the internet browser. The post-processing of the data, including the unzipping and the plotting of results, occurs nearly instantly. As a reference, the code written for `autASA.py` is included in Appendix B.

4.4.3. Example: variation of the effective density of states

In this section, the use of `autASA` and the post-processing of the data will be illustrated with an example of 4 simulations where the effective density of states at the edge of the conduction band, N_C , was varied for the intrinsic a-Si:H layer. The plot of the $J - V$ curves and EQE are shown in Figures 4.7 and 4.8.

With `autASA`, the impact of the change of this parameter could be quickly computed and plotted. The results agree with what one could physically expect of a cell that undergoes this change. An increase of N_C for the intrinsic a-Si:H layer results in a higher free electron concentration, such that the current delivered by the cell is enhanced. This effect is the greatest for electrons generated by the absorption of short wavelength photons, as seen in Figure 4.8. On the other hand, the increase of charge carriers leads to a higher recombination, which is evidenced in the decrease of V_{oc} .

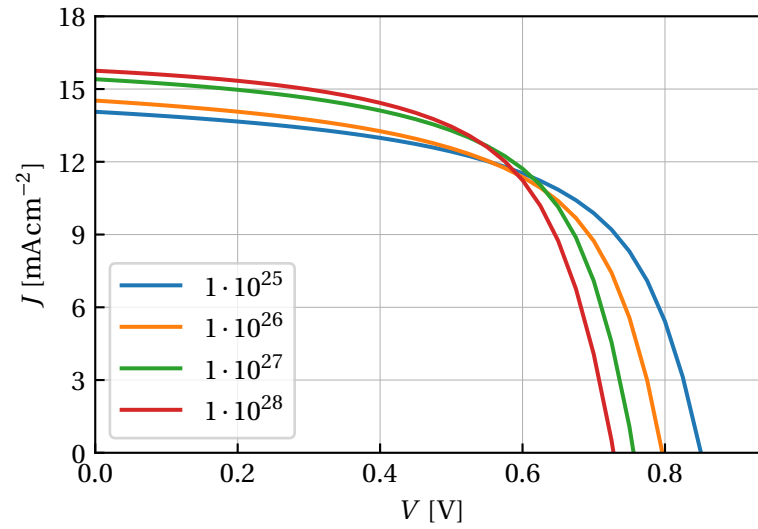


Figure 4.7: $J - V$ curves of the simulations where N_C was varied for the intrinsic a-Si:H layer. The legend indicates the changed parameter in units of m^{-3} .

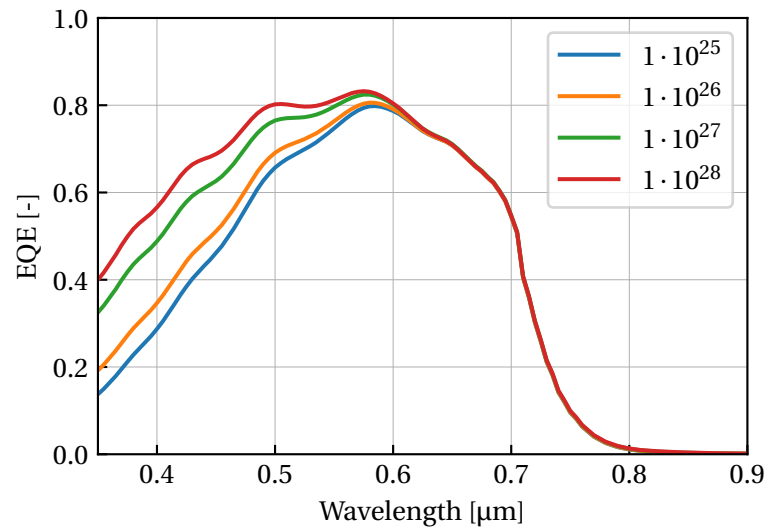


Figure 4.8: EQE curves of the simulations where N_C was varied for the intrinsic a-Si:H layer. The legend indicates the changed parameter in units of m^{-3} .

4.5. Sensitivity analysis

Although the impact of the change of a specific model parameter in one of the layers of a solar cell can often be predicted qualitatively, the exact dependence of the operation of the device given this change is generally not known *a priori*. This makes it difficult to give a quantitative indication of the change.

When considering the use of simulations for the prediction and optimisation of the performance of a solar cell, it is of great importance to obtain a model that correctly describes the system. The description of the layers defined in ASA include a large number of parameters, specially in the definition of the density of states of the localised states. For a single opto-electrical layer, around 30 parameters need to be defined. This imposes a challenge when trying to match the results of a simulation with experimental data of the modelled device.

In this work, the mentioned matching between simulated results and experimental work was pursued. To this end, knowledge about the impact of the variation of optical and electrical parameters on the performance of the simulated cell was needed. This includes parameters such as the V_{oc} , J_{sc} , FF and η , but also the response of the device for short- and long wavelengths quantified in the EQE. To this end, simulations were performed in which single parameters were varied in a certain range $[a, b]$, where after the difference in the mentioned parameters was computed. The parameters were varied in a range of typical values it could attain, guided by the default value set in ASA, the value in the reference simulation *cas* file analysed in Section 4.3, other studies where ASA was used [75] and physical insights.

The difference was calculated in relative terms, as indicated in Equation (4.10).

$$\Delta X = \frac{X_b - X_a}{X_a}, \quad (4.10)$$

with ΔX the relative difference of parameter X and X_a and X_b the value of X for the results of the simulation when inputting the lower and upper value in the varied range, respectively. In this case, $X \in \{V_{oc}, J_{sc}, FF, \eta\}$. For the spectral response, a distinction was made between the impact on short- and long-wavelength photons. This was quantified by integrating the EQE from 300 nm to 550 nm and from 550 nm to 800 nm. Again, a relative comparison was done for the variation of a parameter in a range $[a, b]$ to obtain useful information about the difference, as seen in Equation (4.11).

$$\Delta EQE|_x^y = \frac{\int_x^y EQE_b(\lambda) d\lambda - \int_x^y EQE_a(\lambda) d\lambda}{\int_x^y EQE_a(\lambda) d\lambda}, \quad (4.11)$$

where $(x, y) \in \{(300 \text{ nm}, 550 \text{ nm}), (550 \text{ nm}, 800 \text{ nm})\}$. In this way, the impact of changing parameters in the simulations on the EQE can be known for the higher and lower range of the spectrum independently.

This analysis led to an overview of the sensitivity of the model parameters on the performance of the simulated solar cell. The results are gathered in Table 4.3. The reference simulation file was not the default *.cas* file from ASA introduced in Section 4.3, but one introduced later in Section 4.6.1. The structure of the cell can be seen in Figure 4.9 and was used because it reflects the optical properties of the system that will be analysed in this

work. In order to have a clear overview of the results, the relative differences in the parameters for each variation range were grouped depending on the impact: negligible, low, moderate and high. The symbols that are assigned to each group are summarised in Table 4.2. For a reference to the actual relative percentage differences, the reader is referred to Table C.1 in Appendix C.

Table 4.2: Reference symbols used in Table 4.3 to indicate the degree to which the variation of a model parameter impacts the performance indicators of the solar cell.

Impact	Relative difference range [%]	Symbol
Negligible	(-1, 1)	~
Low	(-5, -1]	-
	[1, 5)	+
Moderate	(-15, -5]	--
	[5, 15)	++
High	≤ -15	---
	≥ 15	+++

Table 4.3: Symbolic results of the sensitivity of the open-circuit voltage V_{oc} , short-circuit current density J_{sc} , fill factor FF , efficiency η , EQE for the range 300 nm to 550 nm (labelled as EQE₁) and for 550 nm to 800 nm (labelled as EQE₂) to the variation of model parameters in ASA simulations. The abbreviations are described in Nomenclature.

Parameter	Variation range	Unit	Relative difference Δ					
			V_{oc}	J_{sc}	FF	η	EQE ₁	EQE ₂
Layer thickness		nm						
Front TCO	[500-900]		~	-	~	-	--	-
Front AZO	[0-5]		~	~	~	~	~	~
	[5-50]		~	-	~	-	-	-
a-Si:H(p)	[5-25]		~	--	--	--	---	-
a-Si:H(i)	[150-450]		-	++	--	--	--	+++
a-Si:H(n)	[5-25]		~	-	~	-	~	-
Back AZO	[0-5]		~	++	~	++	~	++
	[5-100]		~	~	~	~	~	-
Back reflector	[100-500]		~	~	~	~	~	~
Band gap		eV						
a-Si:H(p)	[1.8-2.0]		++	+	+	++	++	+
	[2.0-2.2]		~	+	--	--	++	~
a-Si:H(i)	[1.6-1.9]		+++	-	++	+++	--	-
a-Si:H(n)	[1.6-1.9]		~	+	~	+	~	+
Mobility		$m^2 V^{-1} s^{-1}$						
Electron								
a-Si:H(p)	$[1 \cdot 10^{-4} - 1 \cdot 10^{-2}]$		-	~	~	~	++	+

Table 4.3: Symbolic results of the sensitivity of the open-circuit voltage V_{oc} , short-circuit current density J_{sc} , fill factor FF , efficiency η , EQE for the range 300 nm to 550 nm (labelled as EQE₁) and for 550 nm to 800 nm (labelled as EQE₂) to the variation of model parameters in ASA simulations. The abbreviations are described in Nomenclature.

Parameter	Variation range	Unit	Relative difference Δ						
			V_{oc}	J_{sc}	FF	η	EQE ₁	EQE ₂	
a-Si:H(i)	$[1 \cdot 10^{-4} - 2 \cdot 10^{-3}]$		~	++	++	+++	+++	++	
	$[2 \cdot 10^{-3} - 1 \cdot 10^{-2}]$		~	+	+	+	+	~	
a-Si:H(n)	$[1 \cdot 10^{-4} - 1 \cdot 10^{-2}]$		~	~	~	~	~	~	
Hole									
a-Si:H(p)	$[1 \cdot 10^{-5} - 1 \cdot 10^{-4}]$		~	~	+++	+++	-	+	
	$[1 \cdot 10^{-4} - 1 \cdot 10^{-3}]$		~	~	+	+	-	~	
a-Si:H(i)	$[1 \cdot 10^{-5} - 1 \cdot 10^{-3}]$		-	++	+++	+++	+	+++	
a-Si:H(n)	$[1 \cdot 10^{-5} - 1 \cdot 10^{-3}]$		~	~	~	~	~	~	
Activation energy		eV							
a-Si:H(p)	[0.1-0.45]		~	~	-	-	-	~	
	[0.45-0.6]		--	-	---	---	~	-	
a-Si:H(n)	[0.1-0.3]		~	~	-	-	~	~	
	[0.3-0.6]		--	-	---	---	-	-	
DOS ext.		m^{-3}							
N_C									
a-Si:H(p)	$[1 \cdot 10^{25} - 1 \cdot 10^{28}]$		-	--	~	--	--	-	
a-Si:H(i)	$[1 \cdot 10^{25} - 1 \cdot 10^{28}]$		--	++	-	--	+++	+	
a-Si:H(n)	$[1 \cdot 10^{25} - 1 \cdot 10^{28}]$		~	~	~	~	~	~	
N_V									
a-Si:H(p)	$[5 \cdot 10^{25} - 5 \cdot 10^{26}]$		~	~	+++	+++	-	+	
	$[5 \cdot 10^{26} - 1 \cdot 10^{28}]$		~	~	++	++	-	~	
a-Si:H(i)	$[1 \cdot 10^{25} - 1 \cdot 10^{28}]$		--	+	++	--	-	++	
a-Si:H(n)	$[1 \cdot 10^{25} - 1 \cdot 10^{28}]$		~	-	~	-	~	-	
DOS loc.									
CB tail									
e.char		eV							
a-Si:H(p)	[0.01-0.1]		~	~	~	~	~	~	
a-Si:H(i)	[0.01-0.06]		-	~	~	-	~	~	
	[0.06-0.1]		-	--	--	---	---	--	
a-Si:H(n)	[0.01-0.1]		~	~	~	~	~	~	
n.emob		$m^{-3} eV^{-1}$							
a-Si:H(p)	$[1 \cdot 10^{26} - 1 \cdot 10^{29}]$		~	~	~	~	~	~	
a-Si:H(i)	$[1 \cdot 10^{26} - 1 \cdot 10^{29}]$		-	~	~	~	~	~	
a-Si:H(n)	$[1 \cdot 10^{26} - 1 \cdot 10^{29}]$		~	~	~	~	~	~	
c.neut (all)	$[1 \cdot 10^{-16} - 1 \cdot 10^{-13}]$	$m^{-3} s^{-1}$	~	~	~	~	~	~	
c.neg (all)	$[1 \cdot 10^{-16} - 1 \cdot 10^{-13}]$	$m^{-3} s^{-1}$	~	~	~	~	~	~	
e.range (all)	[0.1-1]	eV	~	~	~	~	~	~	
VB tail									

Table 4.3: Symbolic results of the sensitivity of the open-circuit voltage V_{oc} , short-circuit current density J_{sc} , fill factor FF , efficiency η , EQE for the range 300 nm to 550 nm (labelled as EQE₁) and for 550 nm to 800 nm (labelled as EQE₂) to the variation of model parameters in ASA simulations. The abbreviations are described in Nomenclature.

Parameter	Variation range	Unit	Relative difference Δ					
			V_{oc}	J_{sc}	FF	η	EQE ₁	EQE ₂
e.char		eV						
a-Si:H(p)	[0.01-0.1]		~	~	+	+	~	~
a-Si:H(i)	[0.01-0.05]		~	+	-	-	++	~
	[0.05-0.1]		~	---	---	---	---	---
a-Si:H(n)	[0.01-0.1]		~	~	~	~	~	~
n.emob		$m^{-3} eV^{-1}$						
a-Si:H(p)	$[1 \cdot 10^{26} - 1 \cdot 10^{29}]$		~	~	+	+	~	~
a-Si:H(i)	$[1 \cdot 10^{26} - 1 \cdot 10^{27}]$		~	~	~	+	+	~
	$[1 \cdot 10^{27} - 1 \cdot 10^{29}]$		+	-	---	---	++	---
a-Si:H(n)	$[1 \cdot 10^{26} - 1 \cdot 10^{29}]$		~	~	~	~	~	~
c.neut (all)	$[1 \cdot 10^{-16} - 1 \cdot 10^{-13}]$	$m^{-3} s^{-1}$	~	~	~	~	~	~
c.pos (all)	$[1 \cdot 10^{-16} - 1 \cdot 10^{-13}]$	$m^{-3} s^{-1}$	-	~	~	-	-	~
e.range (all)	[0.1-1]	eV	~	+	-	~	++	~
Dangling bonds								
n		m^{-3}						
a-Si:H(p)	$[1 \cdot 10^{21} - 1 \cdot 10^{24}]$		~	~	~	~	-	~
	$[1 \cdot 10^{24} - 1 \cdot 10^{26}]$		~	-	~	---	---	-
a-Si:H(i)	$[1 \cdot 10^{18} - 1 \cdot 10^{21}]$		-	~	---	---	~	~
	$[1 \cdot 10^{21} - 1 \cdot 10^{22}]$		---	-	---	---	-	-
	$[1 \cdot 10^{22} - 1 \cdot 10^{23}]$		---	---	---	---	---	---
a-Si:H(n)	$[1 \cdot 10^{21} - 1 \cdot 10^{26}]$		~	-	~	-	~	-
ce.neut (all)	$[1 \cdot 10^{-16} - 1 \cdot 10^{-13}]$	$m^{-3} s^{-1}$	---	-	---	---	-	-
ce.pos (all)	$[1 \cdot 10^{-16} - 1 \cdot 10^{-13}]$	$m^{-3} s^{-1}$	---	-	-	---	-	~
ch.neut (all)	$[1 \cdot 10^{-16} - 1 \cdot 10^{-13}]$	$m^{-3} s^{-1}$	---	-	---	---	-	-
ch.neg (all)	$[1 \cdot 10^{-16} - 1 \cdot 10^{-13}]$	$m^{-3} s^{-1}$	---	-	---	---	~	-

For every change in the model parameters in Table 4.3, all the other values in the simulation file were left unaltered. For those rows where no unit is present, the parameter assumes the same unit as the row above.

In many cases, it was observed that the rate of change of several performance indicators did not change uniformly in a certain range, showing an asymptotic behaviour. It also happened that a uniform increase was followed by a decrease in performance indicators, or vice versa. In all these cases, the variation range of the parameter was split into different parts to observe the contrasting behaviour of the performance indicators. Examples can be seen in the activation energy of the doped layers of a-Si:H and the concentration of dangling bonds in a-Si:H(i).

It is worth mentioning that this sensitivity analysis only includes the variation of parameters separately and does not treat the impact of simultaneous parameter changes. Moreover, some of these independent variations are not a perfect indication of reality, since it

is in many cases impossible to change a unique parameter. For instance, it is known that the change in band gap of the absorber layer in an a-Si:H cell has an impact on the complex refractive index of the material, given the way light will interact differently with this layer. However, this is not included in the simulations performed. Despite these limitations, the results give a clear indication of the impact of the simulation parameters on the operation of the solar cell. This becomes important when calibrating the model in order to match experimental data. The model parameters can then be adjusted accordingly with the information contained in Table 4.3.

4.6. Calibration of the model

In order to use ASA for the prediction and optimisation of the performance of a micro-morph cell, it is important to have a properly calibrated model. Given the use of two cells stacked on top of each other, it becomes difficult to predict the impact of the model parameters of one subcell on the performance of the total device. For this reason, the model parameters for an a-Si:H and a $\mu\text{c-Si:H}$ cell were calibrated independently. The sensitivity data presented in Table 4.3 is used to choose which parameters need adjustment. The quality of the calibration will be evaluated with the resemblance between simulated and experimental performance indicators: V_{oc} , J_{sc} , FF , η and the EQE. All this information can be obtained by comparing the $J - V$ and EQE curves of the results.

Once this calibration is completed, the two separately adjusted models can be combined to arrive at a reference simulation file for the micromorph device. Only then can optimisation of the device performance start. This is discussed later in Chapter 5. To start, the model calibrations for the a-Si:H and $\mu\text{c-Si:H}$ cells are described next, along with the experimental data taken as a reference for this calibration.

4.6.1. Validation of HyET a-Si:H single-junction solar cell

Reference cell

The structure of the reference a-Si:H cell produced at HyET is shown in Figure 4.9.

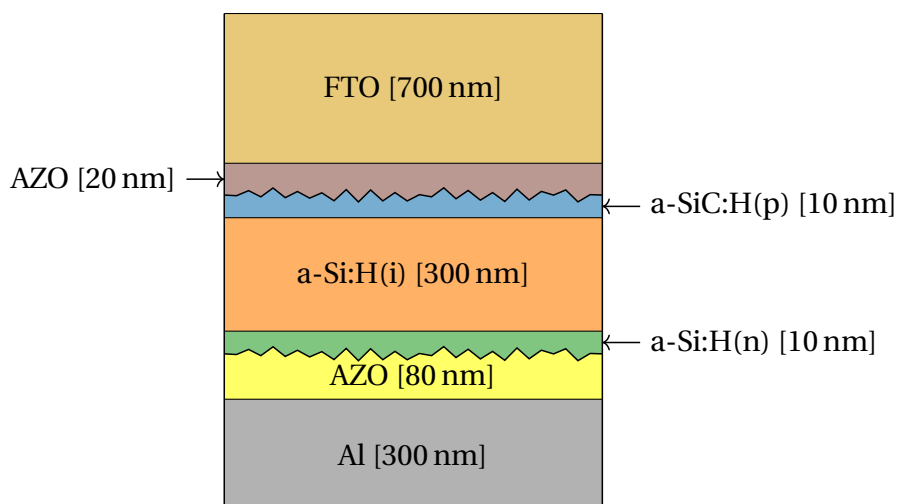


Figure 4.9: Simulation structure of an a-Si:H solar cell produced at HyET. The layer thicknesses are not to scale.

The complex refractive indices of the materials used in the simulation are plotted in

Appendix D.1. The experimental data used to calibrate the model of the a-Si:H cell was obtained from HyET Solar. Typical $J - V$ and EQE curves of their roll-to-roll manufactured device were used. The same deposition conditions can be expected for a micromorph device, with the addition of some extra layers for the $\mu\text{c-Si:H}$ cell. For this reason, it serves as valid reference measurements for the calibration of the model.

The $J - V$ and EQE curves are presented in Figure 4.10, along with the performance of the device in Table 4.4. The optical structure of the cell shown in Figure 4.9 was implemented in ASA, using the electrical parameters of the default simulation file. These results are also included for reference.

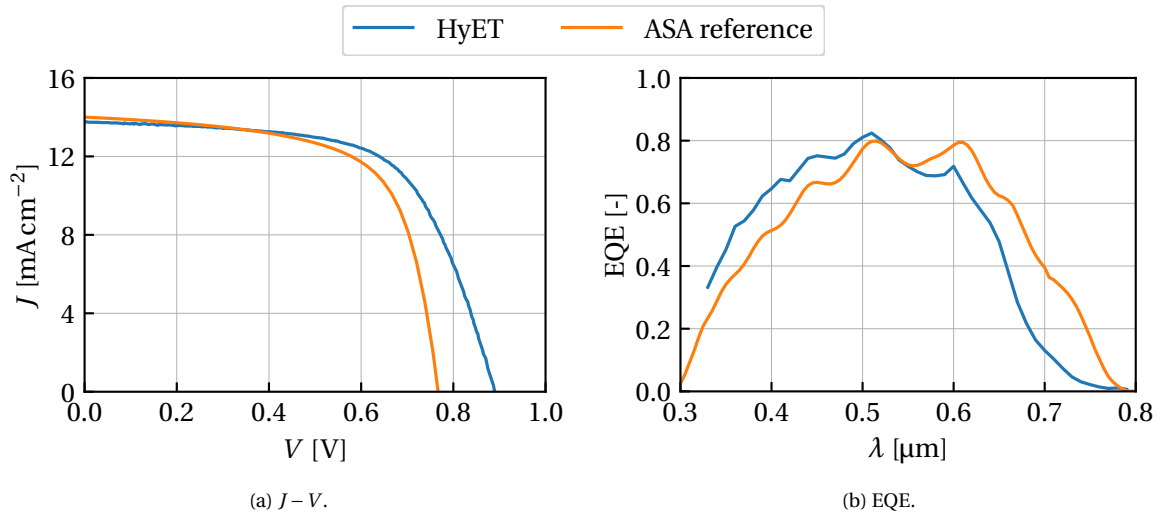


Figure 4.10: Typical performance of a HyET flexible cell and results of the default ASA simulation: a) $J - V$ curve and b) EQE .

Table 4.4: Performance parameters V_{oc} , J_{sc} , FF and η of a typical a-Si:H flexible solar cell produced by HyET Solar, along with the values of the default ASA simulation file.

a-Si:H cell	V_{oc} [V]	J_{sc} [mA cm^{-2}]	FF [-]	η [%]
HyET	0.890	13.76	0.63	7.72
ASA reference	0.767	14.00	0.657	7.05

From these results, it can be seen that the ‘ASA reference’ simulation serves as a good starting point for the calibration of the model. It resembles the J_{sc} and FF of HyET’s cell, but has a V_{oc} far below the required one. All in all, it ends up with an efficiency a bit lower than HyET’s. Even though the J_{sc} is closely matched, it is evident from the EQE plot that there is still some optimisation to be done regarding light management. The response for short wavelengths is still too low, whereas the EQE is overestimated for the higher wavelengths. Despite this, the interference pattern of the simulation seems to follow the fringes of HyET’s cell, which is an indication that the layer thicknesses have been chosen correctly.

Tuning the model

In this section, the steps followed to arrive at a match between the simulated and the experimental cell from HyET is introduced. The changes are split into groups, depending on the intended impact of the variation of those parameters. These groups will be considered one by one, presenting the results cumulatively. The legends in the figures indicate the group it belongs to. The summary of all the changes can be found in Table 4.6.

Change 1: band gap

As a start, realistic band gaps were chosen for the a-SiC:H(p) and a-Si:H(i) layers. For the p -doped layer, it was increased from 1.85 eV to a higher band gap of 1.95 eV, which is more typical for this material. Moreover, the band gap of the absorber layer was chosen to be 1.7 eV instead of 1.75 eV, given the information available about this layer produced at HyET. The results of the mentioned changes are seen in Figure 4.11.

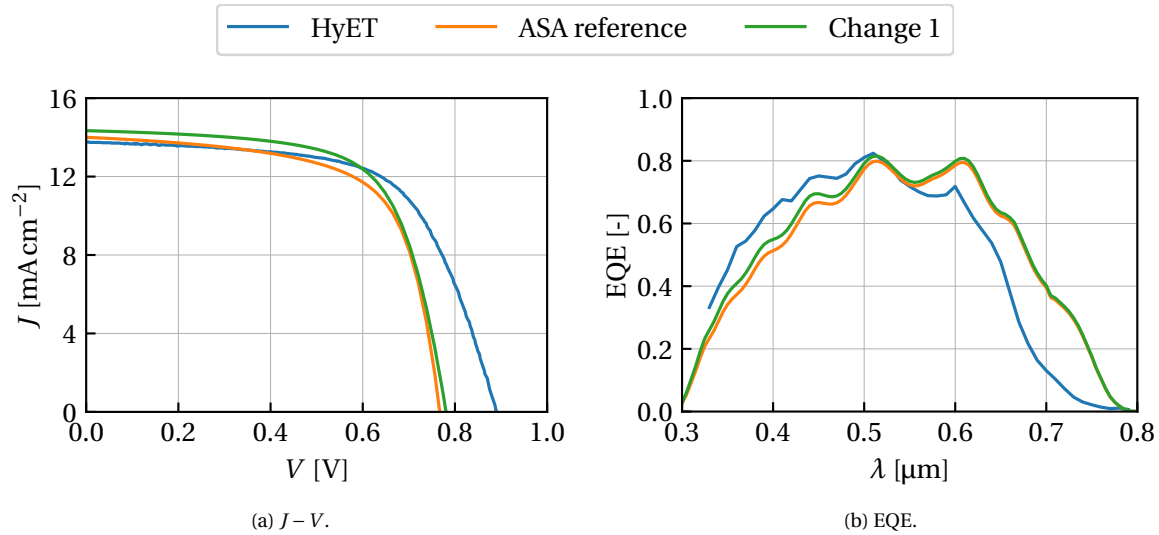


Figure 4.11: Results of the band gap adjustment with respect to the reference ASA simulation.

Change 2: V_{oc}

An increase in the V_{oc} can be experienced without a major change in the other parameters by decreasing the density of states at the edges of the conduction and valence band, N_C and N_V , respectively. For uniformity between the layers, these parameters were decreased from $6 \cdot 10^{26} \text{ m}^{-3}$ to $2 \cdot 10^{26} \text{ m}^{-3}$ for all the a-Si:H layers. The results are seen in Figure 4.12.

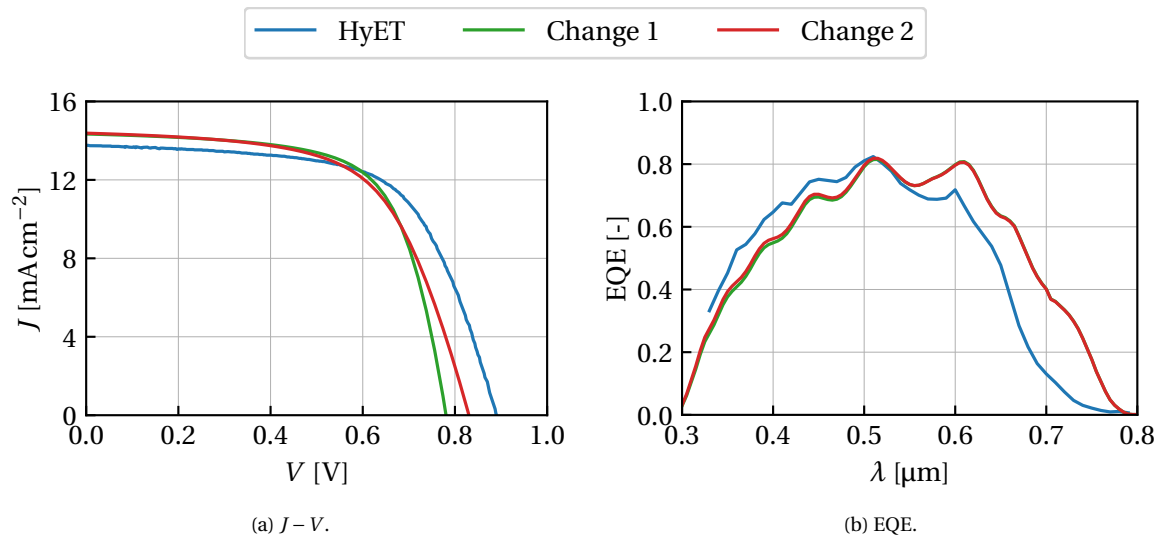


Figure 4.12: Results of the V_{oc} adjustment with respect to 'Change 1'.

Change 3: blue response of EQE

Whereas the change in the red response of the EQE is mostly dependent on the texture properties, the blue response has a major dependence on the electrical properties. This has to do with the fact that short-wavelength photons will be absorbed regardless of the texturing given their high absorption coefficient in this region. Therefore, the dangling bond density of a-Si:H(p) was decreased from $8 \cdot 10^{24} \text{ m}^{-3}$ to $1 \cdot 10^{24} \text{ m}^{-3}$, and the electron capture rate of positively charged dangling bond was decreased from $5 \cdot 10^{-13} \text{ m}^{-3} \text{ s}^{-1}$ to $1 \cdot 10^{-14} \text{ m}^{-3} \text{ s}^{-1}$ for all layers. The impact of the changes is shown in Figure 4.13.

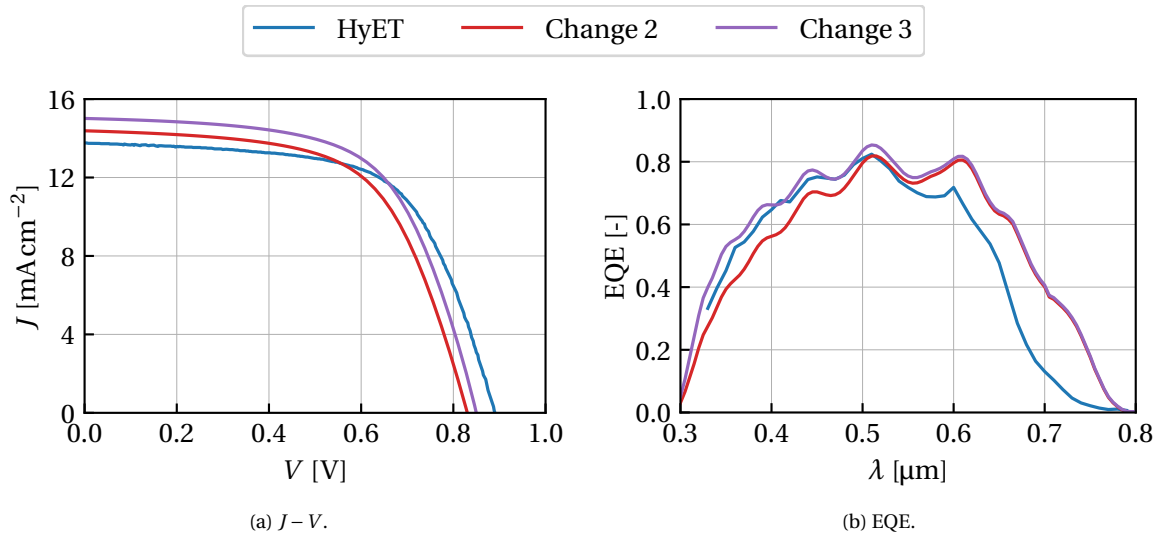


Figure 4.13: Results of the EQE blue response adjustment with respect to 'Change 2'.

Change 4: FF

By decreasing the dangling bond density of the absorber layer from $5 \cdot 10^{21} \text{ m}^{-3}$ to $2 \cdot 10^{21} \text{ m}^{-3}$, the FF was increased to the desired values, accompanied by an increase in the V_{oc} . The results are seen in Figure 4.14.

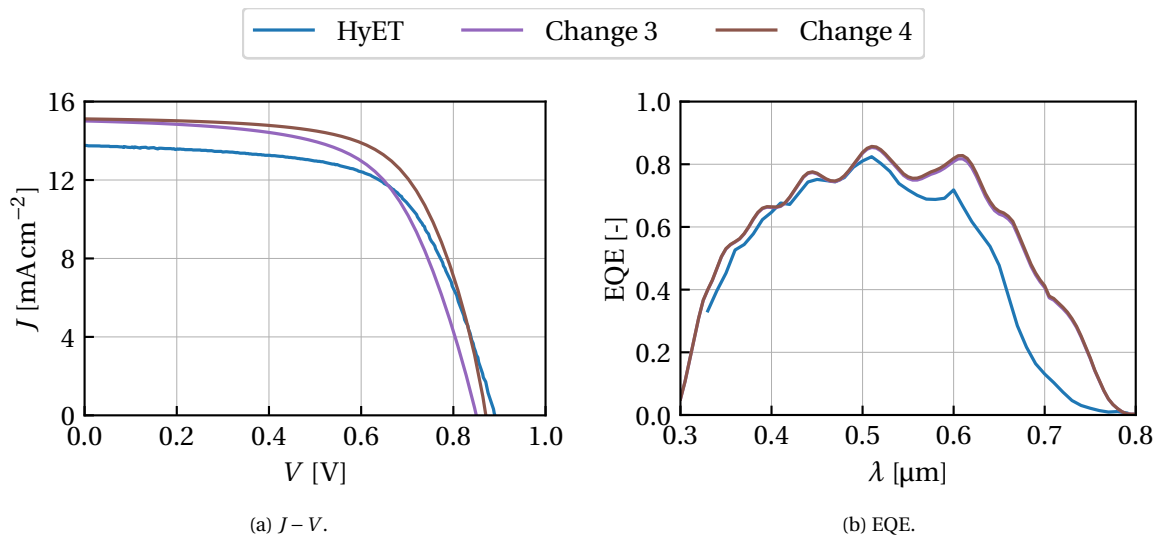


Figure 4.14: Results of the FF adjustment with respect to 'Change 3'.

Change 5: J_{sc}

The red response of the EQE was still too high, and could be adjusted by changing the scattering properties of the interfaces. The haze is computed with the default scattering profile from the ASA simulations, and the angular distribution function (ADF) was chosen such that it matches the J_{sc} . The results are shown in Figure 4.15.

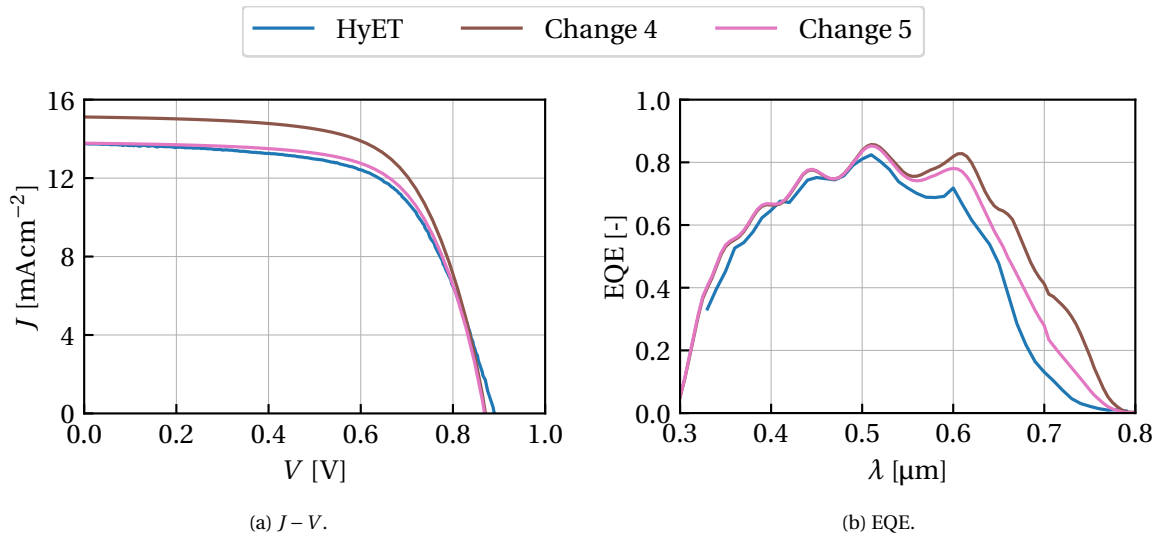


Figure 4.15: Results of the J_{sc} adjustment with respect to 'Change 4'.

Change 6: final adjustments

To reach the desired cell performance, small adjustments were made: increase the band gap slightly from 1.95 eV to 1.98 eV of the p -doped layer, decrease the activation energy of a-Si:H(n) from 0.3 eV to 0.25 eV and increase the characteristic energy of the exponential valence band tail of the intrinsic layer from 0.045 eV to 0.05 eV. With these final adjustments, the resulting $J-V$ curve is identical to the experimental one and the EQE is slightly overestimated around the red, as seen in Figure 4.16.

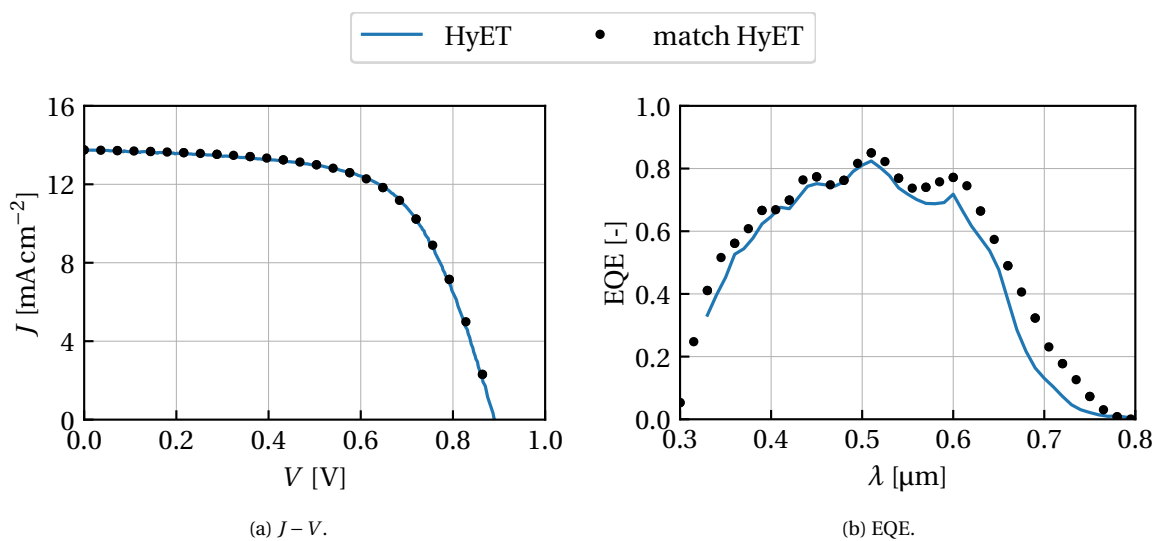


Figure 4.16: Final results of the model calibration of the HyET a-Si:H cell.

The simulated cell performance is shown in Table 4.5. The final calibrated *.cas* file is shown in Appendix A.2.

Table 4.5: Results of the model calibration of HyET's a-Si:H cell.

a-Si:H cell	V_{oc} [V]	J_{sc} [mA cm^{-2}]	FF [-]	η [%]
HyET	0.890	13.76	0.63	7.72
match HyET	0.888	13.75	0.63	7.68

Table 4.6: Overview of the changes of model parameters with respect to the default ASA simulation file to match the solar cell performance of a typical a-Si:H cell from HyET.

Change ID	Desired impact	Changed Parameter		
		Parameter	Old value	New value
Change 1	Start with realistic band gap values	$E_g(\text{i})$ [eV]	1.75	1.70
		$E_g(\text{p})$ [eV]	1.85	1.95
Change 2	Increase V_{oc}	$N_C(\text{pin})$ [m^{-3}]	$6 \cdot 10^{26}$	$2 \cdot 10^{26}$
		$N_V(\text{pin})$ [m^{-3}]	$6 \cdot 10^{26}$	$2 \cdot 10^{26}$
Change 3	Increase blue response of EQE	$n_{DB}(\text{p})$ [m^{-3}]	$8 \cdot 10^{24}$	$1 \cdot 10^{24}$
		$\text{ce.pos}(\text{pin})$ [$\text{m}^{-3} \text{s}^{-1}$]	$5 \cdot 10^{-13}$	$1 \cdot 10^{-14}$
Change 4	Increase FF	$n_{DB}(\text{i})$ [m^{-3}]	$5 \cdot 10^{21}$	$2 \cdot 10^{21}$
Change 5	Decrease J_{sc}	ADF	-	-
Change 6	Obtain a closer match	$E_g(\text{p})$ [eV]	1.95	1.98
		$E_{act}(\text{n})$ [eV]	0.30	0.25
		$\text{e.char}_{VB}(\text{i})$ [eV]	0.045	0.05

4.6.2. Validation of $\mu\text{c-Si:H}$ single-junction solar cell

Reference cell

No reference $\mu\text{c-Si:H}$ cell from HyET Solar was available, since this is still an ongoing study within FlamingoPV. In order to calibrate a model for this absorber material for its use in the micromorph device, a reference $\mu\text{c-Si:H}$ cell developed by H. Tan et al [76] was used. The structure of this reference $\mu\text{c-Si:H}$ cell is presented in Figure 4.17.

The complex refractive indices of the layers used in the simulation are shown in Appendix D.2. It was observed in the simulations that the original thickness of the AZO (800 nm) was too detrimental for the blue response of the EQE. This can be attributed to the refractive index of AZO available for the simulations, which might not match the exact optical data used in the mentioned work. To improve the response for short-wavelength photons, the thickness of this layer was slightly reduced to 600 nm for the simulations.

A reference file from ASA was used as a starting point for the electrical parameters in the simulation of the $\mu\text{c-Si:H}$ cell. The performance and the desired final output from H. Tan et al [76] are shown in Table 4.7, along with the $J - V$ curve and EQE in Figure 4.18. In the remaining of this section, the latter cell will simply be called 'Tan'. The starting value of J_{sc}

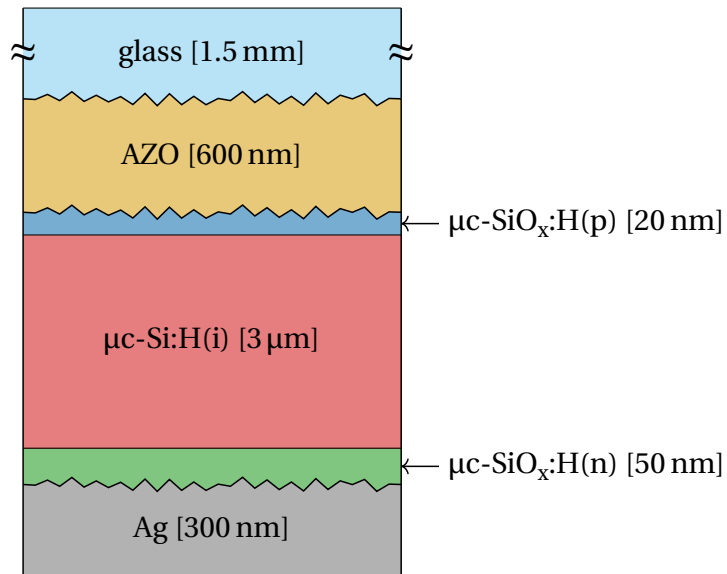


Figure 4.17: Simulation structure of a $\mu\text{c-Si:H}$ solar cell from [76]. The layer thicknesses are not to scale.

is reasonable considering the calibration goal, but the EQE is still underestimated over the majority of the spectrum. Moreover, an interference pattern is present in the default texturing defined in ASA, which can be addressed by increasing the scattering at the textured interfaces. With respect to the V_{oc} , a considerable gain is needed to approach the desired value. Finally, the major deviation of the default simulation file in ASA from the calibration goal is the low FF, which compromises the performance of the cell.

Table 4.7: Performance parameters V_{oc} , J_{sc} , FF and η of the calibration goal of a cell described by H. Tan [76], along with the values of the default ASA simulation file.

$\mu\text{c-Si:H}$ cell	V_{oc} [V]	J_{sc} [mA cm^{-2}]	FF [-]	η [%]
Tan	0.545	24.4	0.707	9.4
ASA reference	0.439	20.9	0.438	4.0

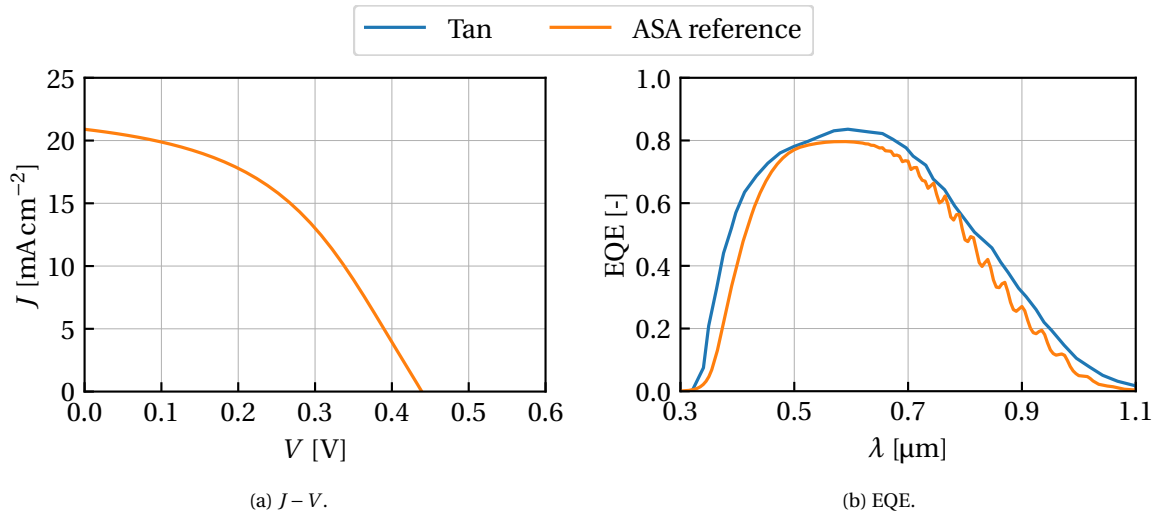


Figure 4.18: Results of the default ASA $\mu\text{c-Si:H}$ simulation and the calibration goal from a cell in H. Tan et al [76]: a) $J-V$ curve and b) EQE. No target $J-V$ curve was provided.

Tuning the model

As with the calibration of the a-Si:H cell, the steps followed to obtain a reasonable match with experimental data of the $\mu\text{c-Si:H}$ cell are described here. The same methodology is followed. The summary of the changes is seen in Table 4.9. To avoid changing model parameters to unrealistic values, many parameters were marginally changed from their default values. Moreover, calibration parameter values described in K. Ding et al [75] were taken as an indication of possible values the model parameters could attain.

Change 1: V_{oc}

To increase the V_{oc} of the simulated cell, the effective density of states of both band edges N_C and N_V of the intrinsic layer was decreased from $3 \cdot 10^{25} \text{ m}^{-3}$ to $2.5 \cdot 10^{25} \text{ m}^{-3}$. Moreover, the density of dangling bonds n of the intrinsic layer was decreased from $2 \cdot 10^{21} \text{ m}^{-3}$ to $3 \cdot 10^{20} \text{ m}^{-3}$, which also gave a boost in the FF. The results are seen in Figure 4.19.

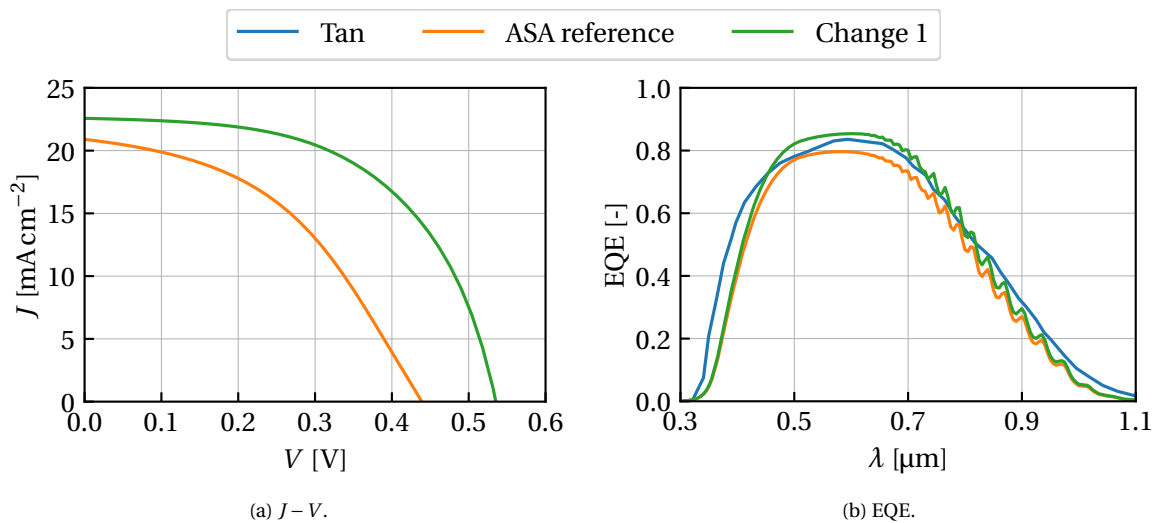


Figure 4.19: Results of the V_{oc} adjustment with respect to the default simulation file in ASA.

Change 2: FF

Even with the V_{oc} adjustment, the FF is seen to be far below the required value. To improve this, the activation energy of the n -doped layer was decreased from 0.25 eV to 0.1 eV, and the mobility of the charge carriers in the intrinsic layer was improved: from $4.5 \cdot 10^{-3} \text{ m}^2 \text{ V}^{-1} \text{ s}^{-1}$ to $7.5 \cdot 10^{-3} \text{ m}^2 \text{ V}^{-1} \text{ s}^{-1}$ and from $5 \cdot 10^{-4} \text{ m}^2 \text{ V}^{-1} \text{ s}^{-1}$ to $30 \cdot 10^{-4} \text{ m}^2 \text{ V}^{-1} \text{ s}^{-1}$ for electrons and holes, respectively.

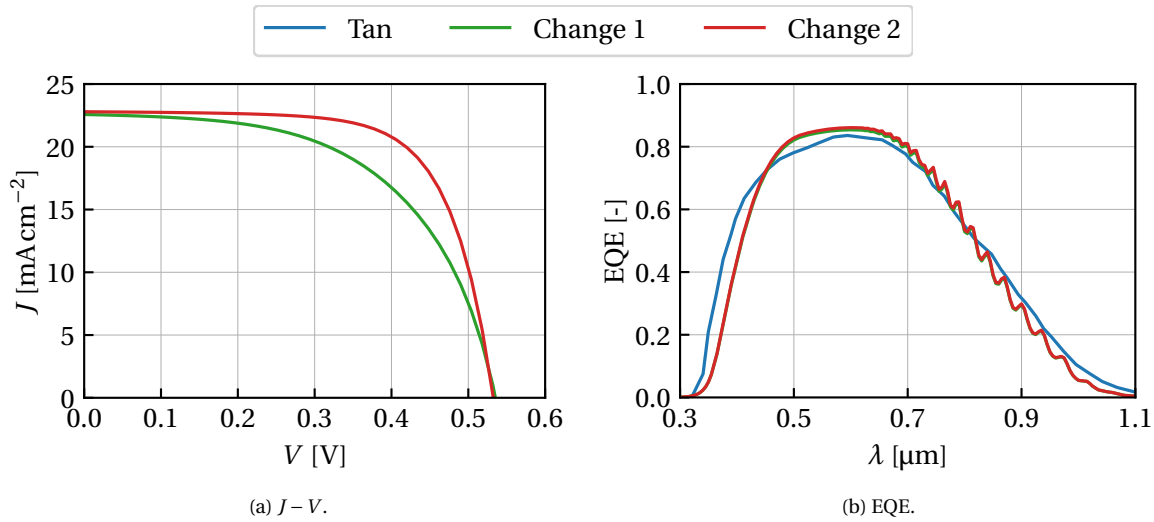


Figure 4.20: Results of the FF adjustment with respect to 'Change 1'.

Change 3: J_{sc}

The interface texturing was changed to improve the J_{sc} as well as to remove the interference effects for high wavelength photons. In the fabrication of the cell, a *modulated surface texture* (MST) was implemented in the front electrode, which enhances the scattering properties. To match this, an AFM scan of a MST developed within the framework of FlamingoPV was used as input for the optical model of the simulation. As seen in Figure 4.21, no interference pattern is present and the J_{sc} is slightly improved.

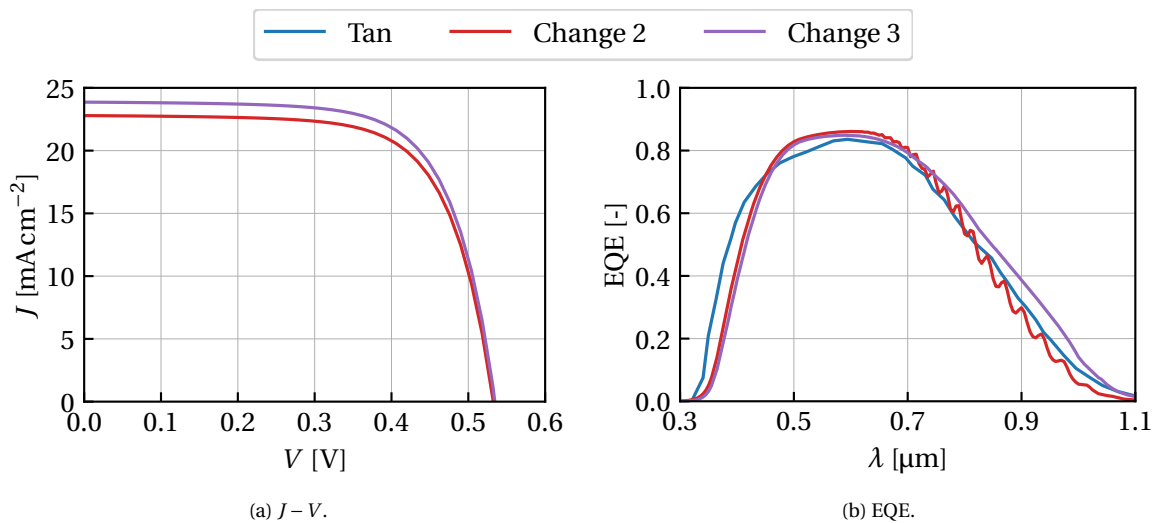


Figure 4.21: Results of the J_{sc} adjustment with respect to 'Change 2'.

Change 4: final adjustments

Final adjustments in the definition of the dangling bonds were made to match the electrical performance of the calibration goal: the concentration of dangling bonds in the p -doped and n -doped layer were decreased from $4 \cdot 10^{25} \text{ m}^{-3}$ to $1 \cdot 10^{23} \text{ m}^{-3}$ and from $4 \cdot 10^{25} \text{ m}^{-3}$ to $1 \cdot 10^{24} \text{ m}^{-3}$, respectively. Finally, the electron capture rate of positively charged dangling bonds and the hole capture rate of negatively charged dangling bonds of all layers were both decreased from $1 \cdot 10^{-13} \text{ m}^3 \text{ s}^{-1}$ to $3 \cdot 10^{-14} \text{ m}^3 \text{ s}^{-1}$. The final results of the calibration is seen in Figure 4.22.

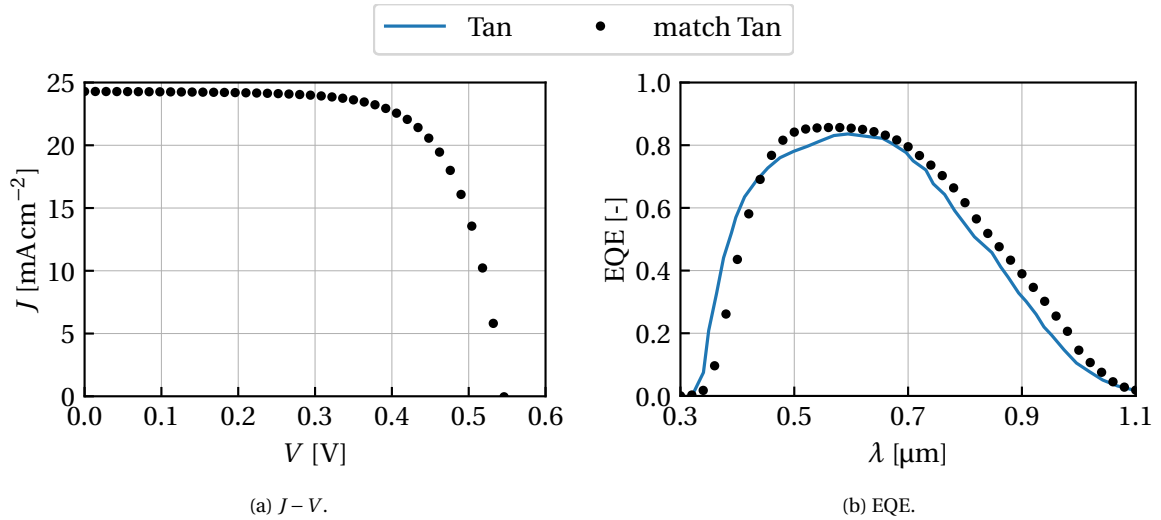


Figure 4.22: Final results of the model calibration of the $\mu\text{c-Si:H}$ cell.

The performance of the matched simulated cell is shown in Table 4.8. The final calibrated *.cas* file is shown in Appendix A.3.

Table 4.8: Results of the model calibration of a $\mu\text{c-Si:H}$ cell from H. Tan et al [76].

$\mu\text{c-Si:H}$ cell	V_{oc} [V]	J_{sc} [mA cm^{-2}]	FF [-]	η [%]
Tan	0.545	24.4	0.707	9.4
match Tan	0.546	24.3	0.701	9.3

Table 4.9: Overview of the changes of model parameters with respect to the default ASA simulation file to match the solar cell performance of the $\mu\text{-Si:H}$ cell.

Change ID	Desired impact	Changed Parameter		
		Parameter	Old value	New value
Change 1	Increase V_{oc}	$N_C(i), N_V(i)$ [m^{-3}]	$3 \cdot 10^{25}$	$2.5 \cdot 10^{25}$
		$n_{DB}(i)$ [m^{-3}]	$2 \cdot 10^{21}$	$3 \cdot 10^{20}$
Change 2	Increase FF	$E_{act}(n)$ [eV]	0.25	0.1
		$\mu_e(i)$ [$\text{m}^2 \text{V}^{-1} \text{s}^{-1}$]	$4.5 \cdot 10^{-3}$	$7.5 \cdot 10^{-3}$
		$\mu_h(i)$ [$\text{m}^2 \text{V}^{-1} \text{s}^{-1}$]	$5 \cdot 10^{-4}$	$30 \cdot 10^{-4}$
Change 3	Adjust J_{sc}	Include MST	-	-
Change 4	Obtain a closer match	$n_{DB}(p)$ [m^{-3}]	$4 \cdot 10^{25}$	$1 \cdot 10^{23}$
		$n_{DB}(n)$ [m^{-3}]	$4 \cdot 10^{25}$	$1 \cdot 10^{24}$
		ce.pos(pin) [$\text{m}^{-3} \text{s}^{-1}$]	$1 \cdot 10^{-13}$	$3 \cdot 10^{-14}$
		ch.neg(pin) [$\text{m}^{-3} \text{s}^{-1}$]	$1 \cdot 10^{-13}$	$3 \cdot 10^{-14}$

5

Performance optimisation of micromorph cell using ASA

5.1. a-Si:H/ μ c-Si:H tandem model in ASA

In order to use ASA for the prediction and optimisation of a micromorph device, it is crucial to properly calibrate the modelling parameters such that it resembles experimental data. This is a difficult task given the vast number of parameters that can be adjusted for each layer in the model. However, the operation of a tandem device can be seen as the series connection of two independent cells connected by means of the tunnel-recombination junction. This gives the possibility of independently calibrating the single-junction cells and then combining them in a multi-junction device. In this section, the calibrated models of the a-Si:H and μ c-Si:H solar cells described in Section 4.6 are used as a starting point for the simulation of a complete micromorph device.

5.1.1. Simulation structure

The simulation of a micromorph device was done by stacking the active layers of the a-Si:H cell on top of the μ c-Si:H cell, with the inclusion of front and back optical layers. The structure of the device is shown in Figure 5.1. Some important considerations with respect to the build up from single-junction structures:

1. *Back reflector*: in contrast to the μ c-Si:H calibration model, the back reflector was changed from Ag to AZO/Al, as with the a-Si:H model. This back reflector is a more realistic scenario for the manufacturing of a low-cost product at HyET Solar and will therefore be used for the rest of this chapter. For an inclusion of Ag as back reflector, refer to Section 5.4.
2. *Interface texturing*: with the single-junction models, texturing was only applied to certain interfaces and default scattering properties defined in ASA were used. This was done in such a way that the EQE of the experimental data was approximated, since the exact interface morphology was not known for those cells. In the interest of the FlamingoPV project, a modulated surface texture was developed, as described in Section 3.2.2. Such a texturing enhances scattering, while at the same time allowing a proper growth substrate for the silicon layers. For this reason, the AFM scan

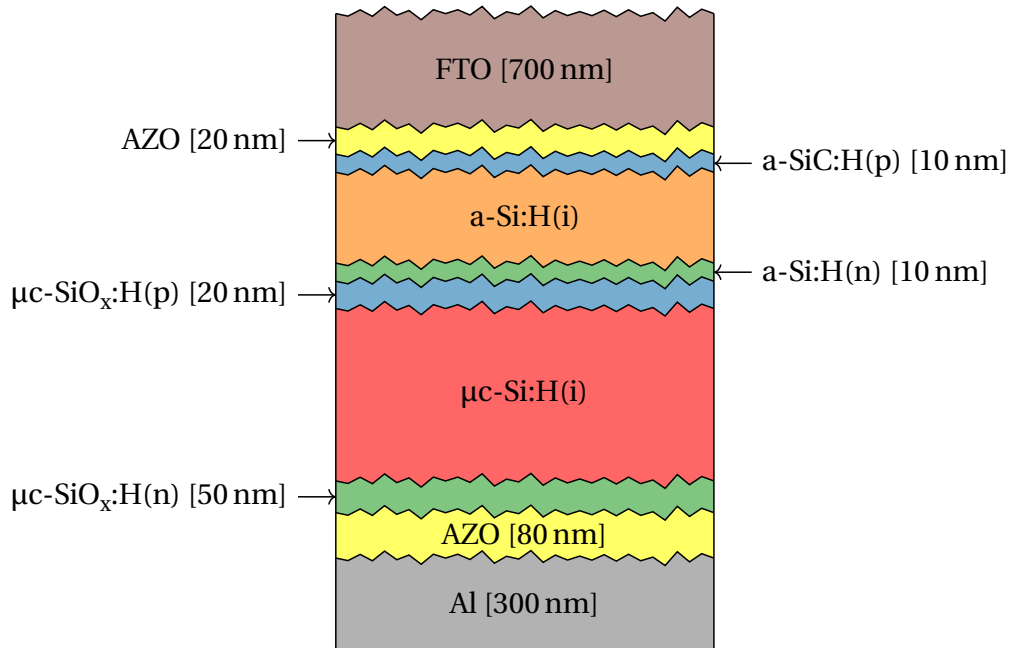


Figure 5.1: Structure used for the simulation of a micromorph solar cell in ASA. The layer thicknesses are not to scale.

of the developed texture on Al foils is used as input for the texturing of the interfaces. Furthermore, it is assumed that all subsequent layers of the cell follow this same texture. It has been reported that this can lead to an overestimation of the EQE at long wavelengths [77], given that the features of the texture are in reality smoothed with increasing thickness. Nevertheless, in the absence of the knowledge of how this smoothing is developed, it serves as a good approximation of the EQE in general. The overestimation is assessed in the final paragraph of Section 5.3.2 for completeness.

3. *TRJ*: in contrast to single-junctions, a tunnel-recombination junction will form at the union of the two subcells. The modelling of such a junction is described in Section 4.2.2.
4. *Absorber layers' thicknesses*: the thicknesses of the intrinsic layers of the top and bottom cells will change with respect to the single-junction cases. Given the new device structure, a redistribution of the light in the layers can be expected. The goal is to find the optimal thicknesses of the intrinsic layers in the remaining of this chapter. For this reason, the thicknesses of the a-Si:H(i) and $\mu\text{c-Si:H(i)}$ layers have not been specified in Figure 5.1 yet.

5.1.2. Device performance

With the device structure defined in Figure 5.1, a simulated thickness series of the top and bottom cells was performed, varying the absorber layers' thicknesses from 100 nm to 500 nm and 500 nm to 4000 nm, respectively. The results of the efficiency, short-circuit current, open-circuit voltage and fill factor of all these possible combinations are plotted in Figure 5.2. From the efficiency plot, it is clear that higher efficiencies can be achieved when compared to the single-junction devices. In the simulated thickness range, a maximum efficiency of 12.1 % is attained, whereas this was limited to 7.7 % and 9.3 % for the a-Si:H and

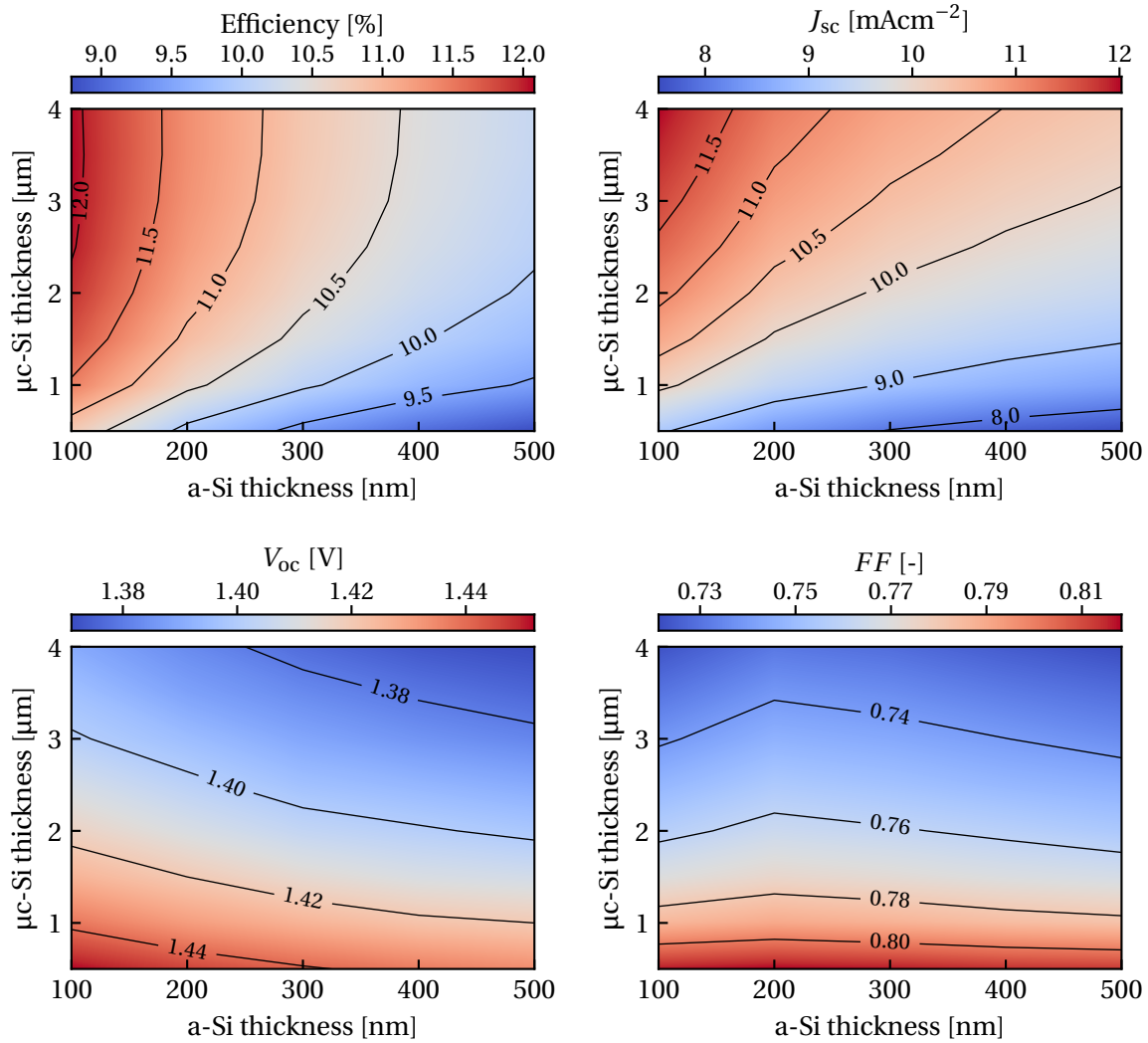


Figure 5.2: Simulated micromorph solar cell parameters for different absorber layer thicknesses of the calibrated a-Si:H and μ c-Si:H single-junction cells.

μ c-Si:H cell, respectively. This is accomplished by delivering a significantly higher voltage with a higher fill factor, which compensates the drop in current given the fact that the two cells need to share the incoming light.

The behaviour of the V_{oc} throughout this thickness range is what can be experimentally expected. In general, thinner layers are beneficial for the V_{oc} given the reduction in recombination losses. The bottom left plot in Figure 5.2 proves this behaviour, where both thin top and bottom cells have a positive impact in the V_{oc} . A total difference of around 80 mV between the maximum and minimum V_{oc} can be expected, which is quite significant and should be taken into account when designing a micromorph device.

The trend in the FF , shown in the bottom right plot in Figure 5.2, indicates that this parameter is mostly dependent on the thickness of the bottom cell, given the nearly horizontal contour lines. Moreover, the high values of the FF in the tandem device evidence that the FF of the bottom cell, with an initially higher value than the top cell, dominates the behaviour of the cell. This is a manifestation of the fact that the bottom cell is limiting the current of the total device. This can also be seen in the plot of the short-circuit current,

since the highest current is achieved at the combination of the thinnest top cell and the thickest bottom cell.

In order to analyse this more thoroughly, it is instructive to look at the short-circuit currents delivered by each subcell during their operation in the tandem device. This analysis provides information on the current-matching condition. The absolute difference in current of each subcell is plotted in Figure 5.3. The way these currents are calculated is explained in Section 5.1.3.

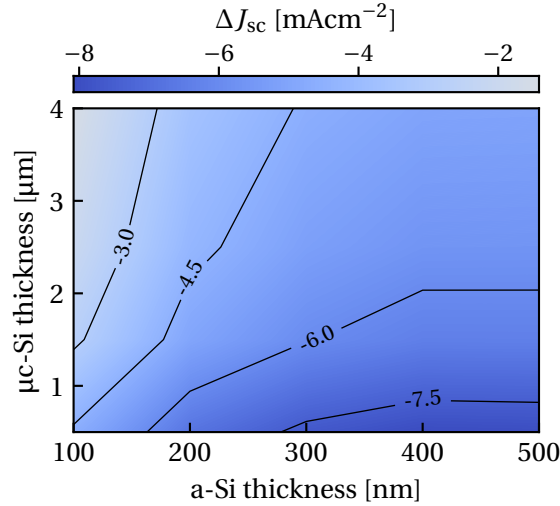


Figure 5.3: Short-circuit current difference between the a-Si:H and $\mu\text{c-Si:H}$ cell in a micromorph device ($\Delta J_{sc} = J_{sc,\mu\text{c-Si}} - J_{sc,\text{a-Si}}$) for different absorber layer thickness combinations.

All the combinations of thicknesses have a negative value, indicating that the current delivered by the top cell is always higher than the current of the bottom cell, in these operational ranges. Such large differences in current shown in Figure 5.3 are generally undesirable for the operation of a tandem device because the excess current will be dissipated in the bottom cell, causing the device to heat up. All in all, given the fact that high efficiencies are only achieved for quite thick bottom cells (around $4\ \mu\text{m}$) and that even at this point there is a high current mismatch, the direct superposition of calibrated single-junction cells is not a guarantee of proper tandem device operation.

This behaviour can be explained by considering the light management around the layers that form the TRJ, which sets a different optical environment compared to the single-junction cases. To this end, the real component of the complex indices of refraction, n , of two layers at each side of the TRJ are plotted in Figure 5.4.

The refractive indices of the non-oxide layers have similar values for all wavelengths, such that it results in low reflections at the interfaces between such layers. This can be seen from the Fresnel coefficients explained in Section 2.1.1. However, the first layer of the bottom cell ($\mu\text{c-SiO}_x\text{:H(p)}$) has a significantly lower refractive index over the whole spectrum. This results in a high reflection at the a-Si:H(n)/ $\mu\text{c-SiO}_x\text{:H(p)}$ and $\mu\text{c-SiO}_x\text{:H(p)}/\mu\text{c-Si:H(i)}$ interfaces and, therefore, less light is available for the intrinsic layer of the bottom cell. For wavelengths below 800 nm, this is beneficial for the current production of the top cell, since the reflected light has another chance to be absorbed in this cell. Nevertheless, higher-wavelength photons are also considerably reflected, which cannot be used by the

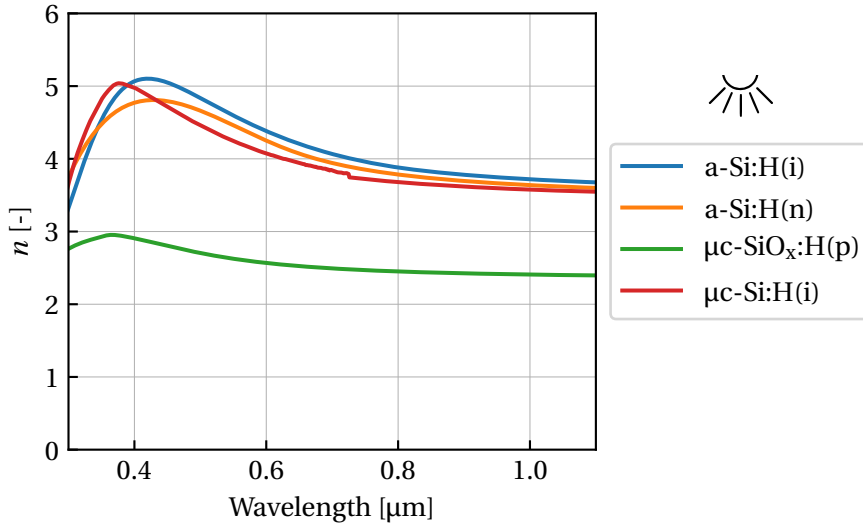


Figure 5.4: Refractive indices n of the layers around the junction between the top and bottom cell. The order of the labels in the legend matches the order of the layers the incoming light passes through.

top cell and are therefore lost to parasitic absorption in other layers or escape the device. Both these contributions results in a reduced current production of the bottom cell, with the consequence of limiting the current of the micromorph device. To tackle this complication, Section 5.2 will consider different solutions to the optical management in the micromorph cell.

5.1.3. Section appendix: simulation of each subcell's J_{sc}

Ideally, the currents produced by each subcell should be the same, given that the total current of the device is limited by the lowest current of the subcells. For this reason, it is also instructive to consider the current difference each cell delivers under short-circuit conditions for each thickness combination. Experimentally, the current of a subcell can be measured by integrating its EQE over the AM1.5 spectrum. As explained in Section 3.3, a bias light of appropriate wavelength should be applied to the device in order to only measure the response of one of the subcells. From a modelling point of view, such a bias light can be chosen in a simulation. However, it was observed that the quality of the resulting EQE was highly dependent on the intensity of the chosen bias light, and often resulted in artefacts. Examples of common errors are shown in Appendix E. Moreover, a bias light should be accompanied by a forward bias voltage in order to ensure a short-circuit operation of the desired subcell, given that the non-targeted subcell will reverse bias the targeted subcell [34]. The choice of this bias voltage is a difficult task and has a large influence on the EQE of the measured subcell [78].

Besides the sensitivity of the bias light and voltage on each subcell's EQE, it was found to be computationally demanding. For this reason, a different approach was adopted to retrieve each subcell's J_{sc} during its operation in the micromorph device. Normally, all the silicon layers are modelled opto-electrically, whereas the front and back layers are only modelled optically. In order to model the electrical behaviour of one of the subcells in the tandem, only this cell is modelled electrically. The layers of the other subcell are added as

purely optical layers. In this way, the light distribution is the same as in the original case, with the difference that the electrical component of only one cell is isolated. To get the J_{sc} of each subcell, two simulations need to be run independently. The short-circuit current densities are then computed from the resulting $J - V$ curves.

This approach was validated by comparing the current delivered by the micromorph device to the currents of the subcells as a function of the absorber layer thickness of the top cell. This was done for a simulation structure where the current of the tandem is first limited by the top cell and becomes bottom cell limited after the top cell has reached a certain thickness. Figure 5.5 shows this comparison for a 1 μm thick bottom cell.

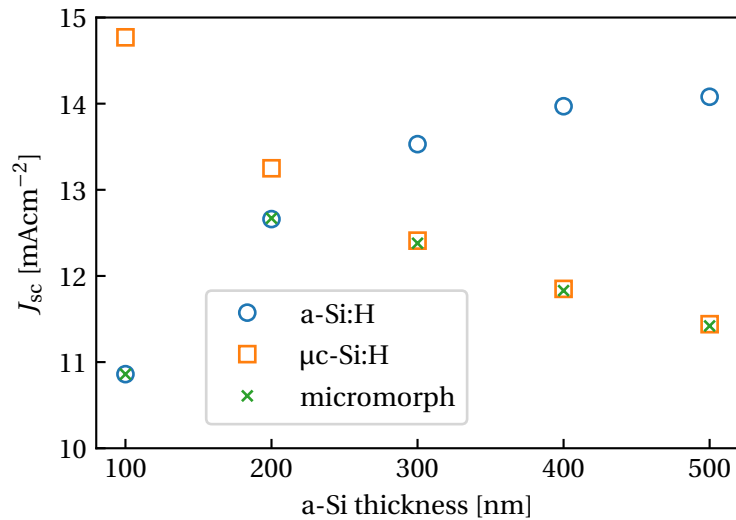


Figure 5.5: Short-circuit current densities of simulations of a micromorph cell and the currents delivered by each subcell as a function of the thickness of the top cell, with a constant bottom cell thickness of 1 μm . The subcells' J_{sc} was computed by only modelling the desired cell electrically.

It is clear that the short-circuit current of the device follows the minimum of the currents of the subcells. This is an indication that the currents delivered by the subcells, computed with the approach described above, are a proper way of circumventing the need of calculating the individual EQEs for an estimation of the current matching conditions.

5.2. Optical considerations at the TRJ layers

In Section 5.1, the micromorph cell was simulated as a direct combination of the layers of each calibrated subcell. This resulted in a poor light management at the TRJ, such that high efficiencies could only be achieved at very thick bottom absorber layers. This section will consider two possible solutions: the adjustment of the refractive index values at the TRJ and the introduction of an intermediate reflector layer.

5.2.1. Sensitivity analysis of refractive indices

In order to demonstrate the principle of the variation of the index of refraction at the layers forming the TRJ, two extra scenarios will be considered:

1. *Scenario 1*: reference simulation structure, including the individually calibrated subcells in the tandem device. Presented in Section 5.1.

2. *Scenario 2*: increase the refractive index of the $\mu\text{c-SiO}_x\text{:H(p)}$ layer to similar values as the neighbouring layers.
3. *Scenario 3*: decrease the refractive index of the a-Si:H(n) layer to similar values as $\mu\text{c-SiO}_x\text{:H(p)}$.

From a modelling perspective, the two new scenarios are implemented by modifying the refractive indices of these layers, while leaving the electrical parameters untouched. To ensure realistic indices of refraction are used, reference optical values of materials that could replace the considered layers are implemented.

Scenario 2: modification of the refractive index of $\mu\text{c-SiO}_x\text{:H(p)}$

In order to test whether the light management in the micromorph cell can be improved by increasing the refractive index of the $\mu\text{c-SiO}_x\text{:H(p)}$ layer, its refractive index was changed to that of $\mu\text{c-Si:H(p)}$, which is predefined in ASA. The refractive indices of the layers that are now around the TRJ are plotted in Figure 5.6.

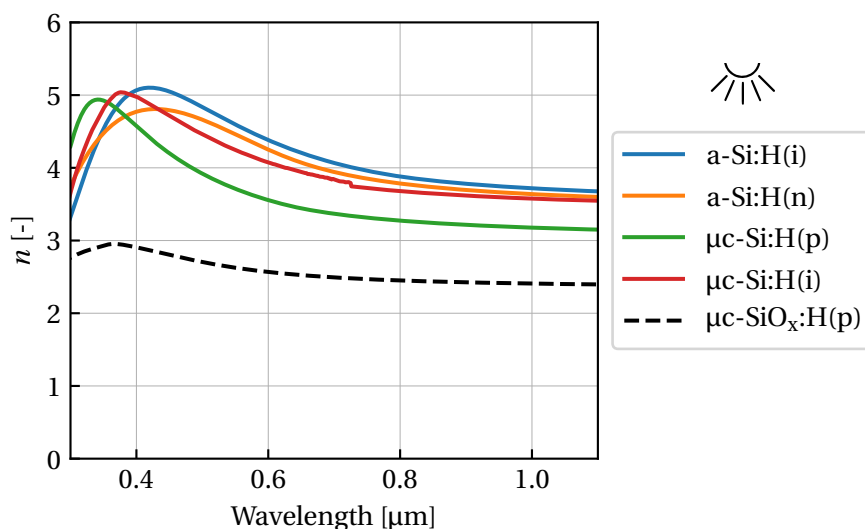


Figure 5.6: Refractive indices n of the layers around the junction between the top and bottom cell of scenario 2. The order of the first four labels in the legend matches the order of the layers the incoming light passes through. The dashed line indicates the previously assigned refractive index values of the p -doped layer of the bottom cell.

Comparing the refractive indices of the $\mu\text{c-Si:H(p)}$ and $\mu\text{c-SiO}_x\text{:H(p)}$ layers, there is a significant increase over the whole spectrum. In this new layer, the refractive index is shifted upwards and the difference between high and low wavelengths increases. The difference with the rest of the layers around the TRJ decreases, so a reduction in the reflection at this interface can be expected. The impact on the performance of the cell is plotted in Figure 5.7, again showing the four performance indicators of the micromorph device.

When considering the efficiency, there are two key factors that result in a better tandem design when compared to scenario 1. Firstly, the maximum efficiency achieved in the considered thickness ranges was increased from 12.1 % to about 13 %. Secondly, the thickness

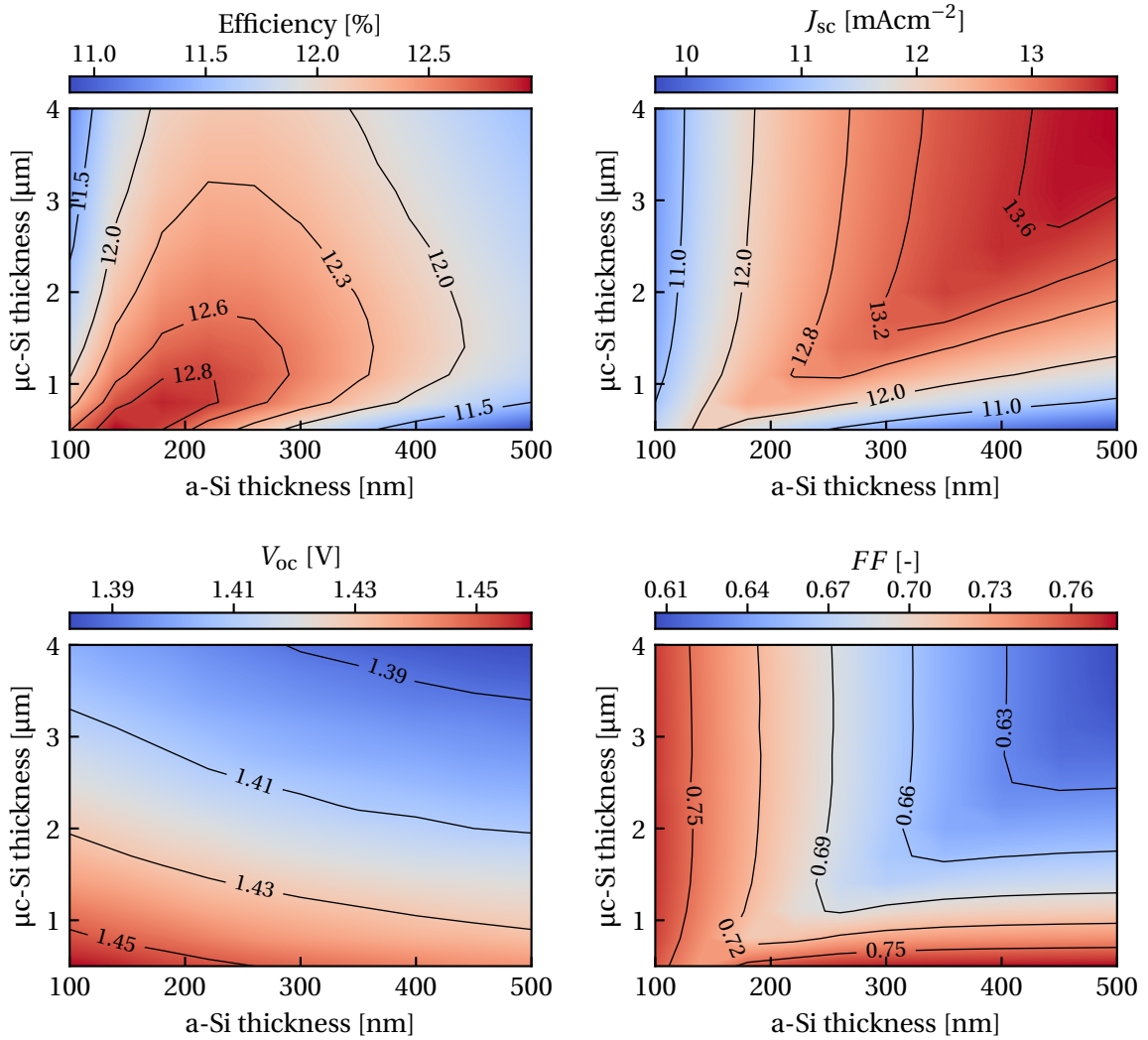


Figure 5.7: Simulated micromorph solar cell parameters for different absorber layer thicknesses for scenario 2.

ranges where this maximum efficiency is reached has shifted to thicker top cells and thinner bottom cells. This is an indication that more light is being delivered to the bottom cell at the expense of less light for the top cell. This is also seen in the J_{sc} plot in the top right, given that the tandem device is delivering higher currents.

A similar behaviour of the V_{oc} is observed as in scenario 1, which is to be expected given that the electrical parameters are left unchanged. However, slightly higher values are observed. This can be attributed to the increased illumination of the bottom cell, which logarithmically increases the open-circuit voltage of this subcell. This increased illumination is greater than the decreased illumination of the top cell, so the combination results in a gain in V_{oc} . Finally, the trend of the FF has drastically changed, given that the bottom cell is not limiting the current for all cases. For a more thorough analysis, the current difference between the subcells is plotted again. This is shown in Figure 5.8.

In contrast to scenario 1, it can be seen now that a current matching between the subcells can be obtained for the simulated thicknesses. The shape of the contour lines of the FF plot in Figure 5.7 change from a vertical orientation to a horizontal orientation when the

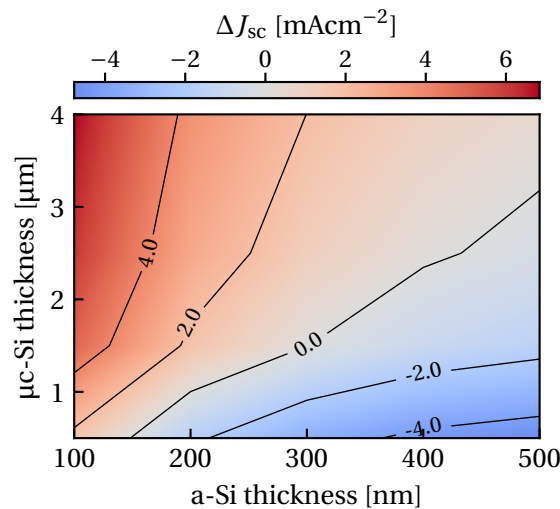


Figure 5.8: Short-circuit current difference for scenario 2 between the a-Si:H and $\mu\text{c-Si:H}$ cell in a micromorph device ($\Delta J_{sc} = J_{sc,\mu\text{c-Si}} - J_{sc,\text{a-Si}}$) for different absorber layer thickness combinations.

current-matching condition is crossed, which evidences the fact that the current-limiting cell has the greatest impact on the overall fill factor of the tandem. A similar behaviour is seen for the J_{sc} plot on the top right. Having a look again at the efficiency in Figure 5.7, the highest values are obtained when the subcells are current-matched.

It can be concluded that the increase of the refractive index of the p -doped layer at the TRJ distributes the light more evenly over the subcells and results in an enhancement of the efficiency of the tandem. In this way, considerably thinner bottom cells ($4\ \mu\text{m}$ vs $<1\ \mu\text{m}$) and slightly thicker top cells ($150\ \text{nm}$ vs $100\ \text{nm}$) can be used.

Scenario 3: modification of the refractive index of a-Si:H(n)

This scenario will consider the decrease of refractive index of the n -doped layer of the top cell to the predefined values of $\text{a-SiO}_x(\text{n})$ in ASA. The relevant refractive indices are plotted in Figure 5.9. In contrast to scenario 1, there is a noticeable difference between the refractive indices of the intrinsic and n -doped layer of the a-Si:H cell. Therefore, significant reflection can be expected at this interface. However, the reflection at the TRJ will be less because these refractive indices are closer together. Finally, a high reflection at the interface between the p -doped and intrinsic layer of the bottom cell can be expected again. The performance of the tandem in scenario 3 is presented in Figure 5.10.

Scenario 3 results in a significant deterioration of the maximum efficiency that can be achieved, dropping from 12.1% in scenario 1 to 10.7%. This maximum efficiency is achieved, again, at the thickest simulated bottom cell, which is an indication that the uneven distribution of light negatively influences the performance of the cell. All the performance indicators in Figure 5.10 follow the same trends as in Figure 5.2, with different absolute values. The J_{sc} and V_{oc} both drop as a consequence of the increased reflection in scenario 3. This has a positive impact on the FF , but it does not compensate for the other losses. For completeness, the current matching condition for this scenario is included in Figure 5.11.

The difference in current between the top and bottom cell has increased even further when compared to scenario 1. This leads to the conclusion that the reduction of the re-

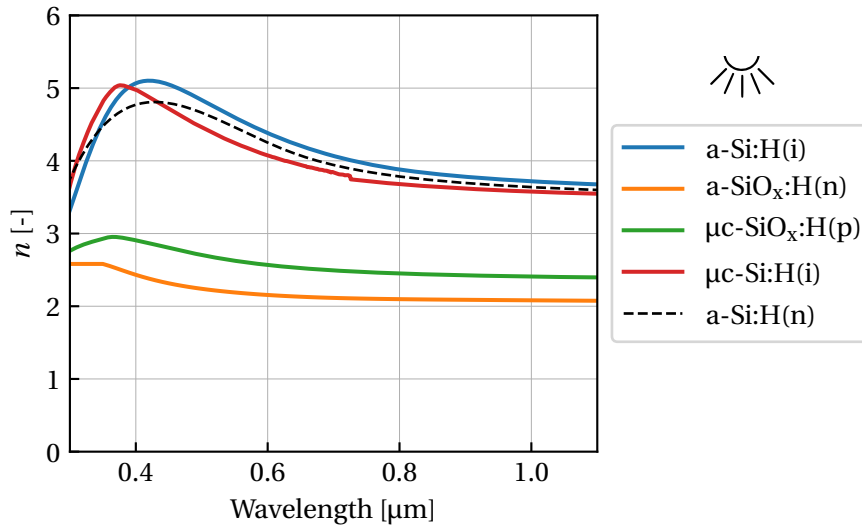


Figure 5.9: Refractive indices n of the layers around the junction between the top and bottom cell of scenario 3. The order of the first four labels in the legend matches the order of the layers the incoming light passes through. The dashed line indicates the previously assigned refractive index values of the n -doped layer of the top cell.

fractive index of the n -doped layer of the top cell to reduce the reflection of the TRJ does not result in a better overall light management the tandem. This is because the reflection is already too high at the intrinsic/ p interface of the top cell.

Overview of the scenarios

To summarise the conclusions to be drawn from the different scenarios, Table 5.1 presents the efficiencies at a typical top/bottom cell thickness combination of 200 nm/2 μm.

Table 5.1: Micromorph efficiency at a top/bottom cell thickness combination of 200 nm/2 μm for the considered scenarios.

Simulation	Efficiency [%]
Scenario 1	11.1
Scenario 2	12.5
Scenario 3	9.6

This remarks the importance of a proper refractive index choice at the layers where the top and bottom cells are united. For the considered simulation structure, the highest efficiency is achieved when the indices of refraction are close to each other (scenario 2), thereby avoiding high reflections at the TRJ over the whole spectrum.

In this scenario, the p -doped layer of the bottom cell was optically modelled as a $\mu\text{c-Si:H(p)}$ layer to obtain a higher refractive index. Experimentally, doped $\mu\text{c-SiO}_x$ layers are often preferred due to an increase in band gap, which results in lower parasitic absorption [79]. These two findings can be combined by creating silicon oxide layers with a high enough refractive index, which is possible by adjusting the deposition conditions (such as

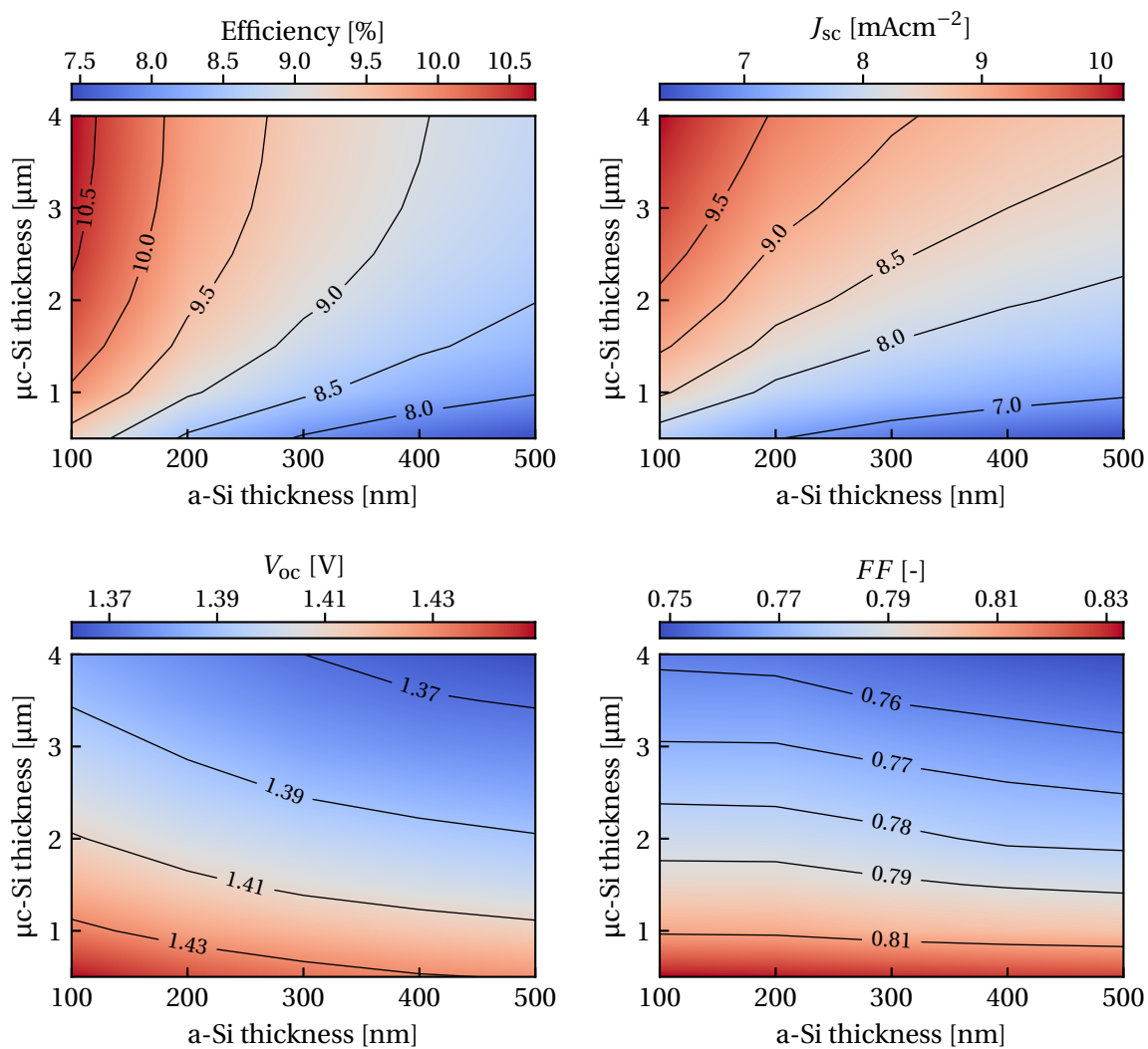


Figure 5.10: Simulated micromorph solar cell parameters for different absorber layer thicknesses for scenario 3.

the increase in deposition pressure for a decrease in the oxygen content [80]). However, careful attention must be paid to ensure the electrical properties of the material are maintained for a proper charge carrier transport.

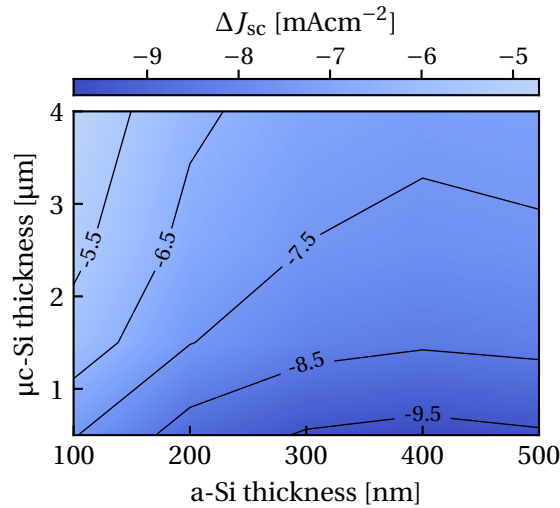


Figure 5.11: Short-circuit current difference for scenario 3 between the a-Si:H and $\mu\text{c-Si:H}$ cell in a micromorph device ($\Delta J_{sc} = J_{sc,\mu\text{c-Si}} - J_{sc,\text{a-Si}}$) for different absorber layer thickness combinations.

5.2.2. Intermediate reflector

The inclusion of an intermediate reflector (IR) in a micromorph device leads to a redistribution of light, which ideally enhances the reflection of low-wavelength and the transmission of high-wavelength photons for an improved spectral utilisation. In this way, the absorber layer of the top cell can be made thinner, since the reflected light boosts the absorbed light in this cell. This results in a cell that is less prone to light-induced degradation.

This section explores the effects of the inclusion of an IR on the scenarios introduced in Section 5.2.1. In order to investigate how much an IR could improve the performance of a micromorph cell, a program was developed to find the ideal complex refractive index such a layer should have in order to provide optimal reflection or transmission properties in the desired part of the spectrum. After having explained the approach to finding this ideal IR, its use in simulations is tested.

Designing an ideal IR

In the search of an ideal IR, the starting point at the junction between the two cells is the one depicted in Figure 5.12.

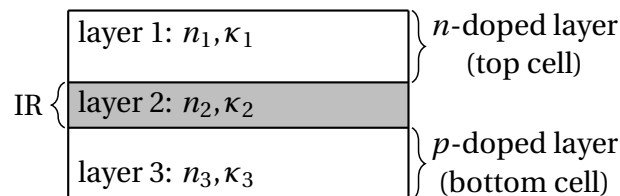


Figure 5.12: Illustration of the inclusion of an IR at the TRJ of a micromorph device.

The refractive indices of the n -doped and p -doped layers of the top and bottom cell, respectively, are determined beforehand. Therefore, n_1 , κ_1 , n_3 and κ_3 are known for a specific simulation structure. The values of the refractive and absorption indices n_2 and κ_2 are variables that will be optimised such that the highest reflection is achieved below a certain

wavelength (hereafter called the transition wavelength λ_t), after which the highest transmission is desired.

Assuming the morphology of the interfaces is such that no interference effects are noticeable, the layers can be treated incoherently, such that the reflection at each interface can be computed using Fresnel's equations. As introduced in Section 2.1.1, these equations depend on the complex indices of refraction at both sides of the interface, the polarisation of light and the angle of incidence. For a general approach, the incoming light is taken to be unpolarised, so the total reflection is computed as the average between parallel and perpendicular polarisation. Moreover, a typical angular intensity distribution (AID) of the textured interfaces is used to account for the distribution of angles of the incident light. The strongest component is the specular, non-scattered light. The decay for angles other than zero is modelled to a good approximation as a Gaussian curve. Figure 5.13 plots the used AID for the computation of the ideal IR.

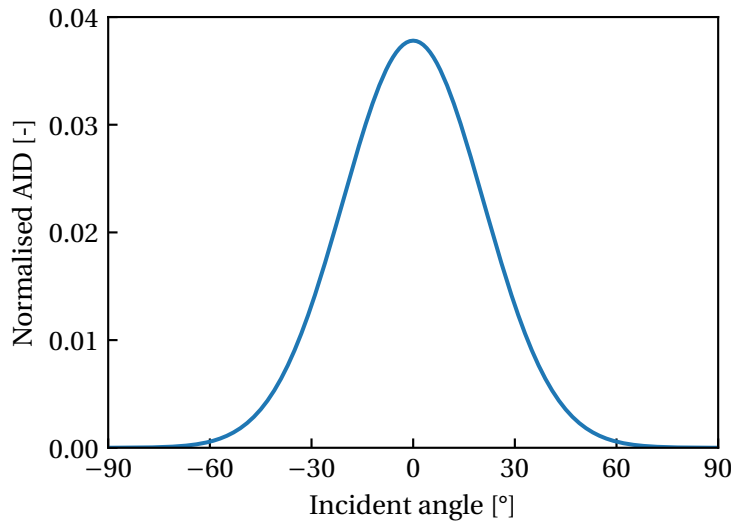


Figure 5.13: Angular intensity distribution of light used to account for the different incidence angles at the IR.

Given the three layers considered in Figure 5.12, the total reflectance and transmittance can be computed with Equations (5.1) and (5.2) [73]:

$$R = R_{12} + \frac{T_{12}R_{23}T_{21}e^{-2\alpha_2d_2}}{1 - R_{23}R_{21}e^{-2\alpha_2d_2}}, \quad (5.1)$$

$$T = \frac{T_{12}T_{23}e^{-\alpha_2d_2}}{1 - R_{23}R_{21}e^{-2\alpha_2d_2}}, \quad (5.2)$$

where R_{xy} and T_{xy} stand for the reflectance and transmittance of light coming from layer x towards layer y , respectively, and α_2 and d_2 the absorption coefficient and thickness of layer 2. These equations result from the consideration of the infinite reflection occurrences as a consequence of introducing the IR. To avoid excessive parasitic absorption in the IR, the thickness was taken to be 5 nm.

In order to find the optimal refractive index of the IR, the total reflectance and transmittance was computed for a set of possible combinations of n_2 and κ_2 . This was done by sampling refractive indices in the range [1, 7] and absorption indices in the range [0, 5].

For each considered wavelength over the spectrum of light, the corresponding refractive indices of layer 1 and 3 are retrieved, which are fixed by the simulation structure. Then, the reflectance and transmittance are computed for all the possible combinations of n_2 and κ_2 and all incidence angles. Afterwards, a weighted average of the angles is performed considering the normalised angular intensity distribution shown in Figure 5.13. This provides the reflectance and transmittance as a function of n_2 and κ_2 . By repeating this calculation for all the relevant wavelengths, a complete map of the reflection and transmission of light over the spectrum is obtained.

To visualise some of the findings, Figure 5.14 plots the reflectance as a function of n_2 and κ_2 for an incidence wavelength of 400 nm and 800 nm for the TRJ in scenario 2. Depending on the wavelength, the indices n_1 , κ_1 , n_3 and κ_3 will have different values, such that the condition for maximum reflectance and transmittance as a function of n_2 and κ_2 changes throughout the spectrum.

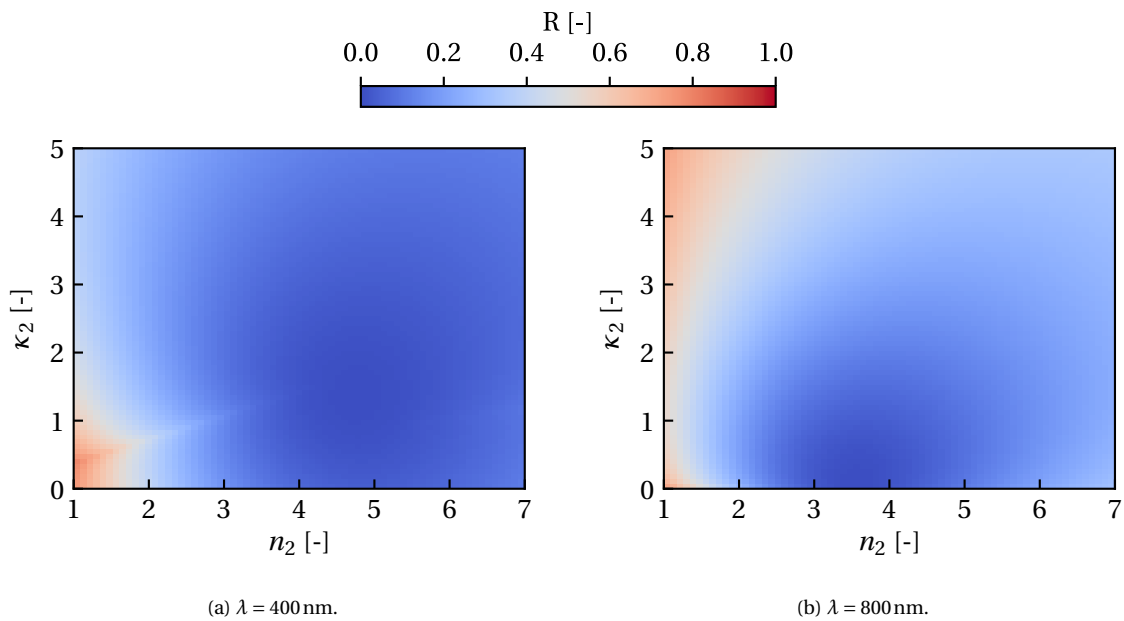


Figure 5.14: Reflectance as a function of the complex refractive index for two wavelengths. n_1 , κ_1 , n_3 and κ_3 are taken from scenario 2.

Once the reflectance and transmittance properties are computed for all wavelengths, the values of n_2 and κ_2 for which a maximum reflectance and transmittance is achieved are computed in all cases. In this way, the ideal values of the refractive index of the intermediate reflector are retrieved. Figure 5.15 plots the refractive index n_2 and absorption index κ_2 that maximise the reflectance and transmittance over the spectrum for scenario 2.

From the figure, it is evident that a low refractive index is desirable for a high reflection at the TRJ. This is accompanied by a varying absorption index. For low wavelengths, it is located around zero, whereas a sudden increase is experienced for around 730 nm onwards. This has to do with a sudden change in the global maximum of the reflectance function. A high reflectance is still achieved for $\kappa_2 = 0$ at high wavelengths, it is only lower in magnitude than the boundary value for $\kappa_2 = 5$. With regards to the conditions for a maximum transmittance, the absorption index should be zero, which ensures no absorption takes place in the IR layer. Moreover, the refractive index of the IR is mainly located in between the

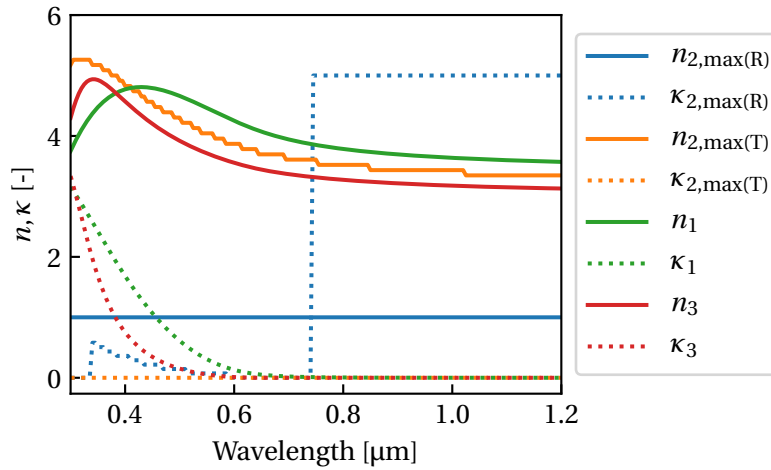


Figure 5.15: Complex refractive index values of the intermediate reflector that maximise the reflectance and transmittance as a function of wavelength. The refractive index data of the adjacent layers are plotted as a reference. The step-like behaviour is a consequence of the discretisation of the domains.

refractive indices of the materials surrounding this layer, which is a known condition that minimises the reflection [8].

The question now is at which wavelength the transition between high reflectance and high transmittance should occur, which was previously defined as λ_t . This depends on the current distribution of the tandem that is being simulated. For a mostly top cell current limiting tandem, a higher value of λ_t is desired than for a bottom cell limiting device, such that a high reflectance is achieved over a larger part of the spectrum. This allows the top cell to generate more current. As an example, Figure 5.16 plots the optical refractive data of an ideal IR for $\lambda_t = 500\text{ nm}$.

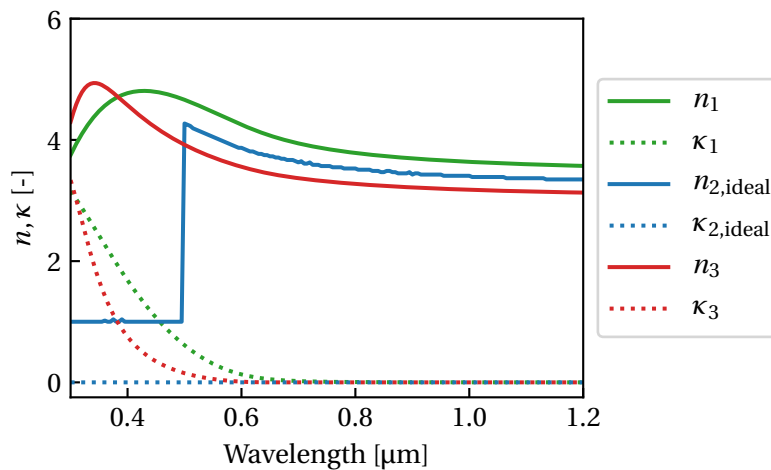


Figure 5.16: Refractive indices of an ideal IR with $\lambda_t = 500\text{ nm}$ and the two layers conforming the TRJ. A finer discretisation of the n and κ domains was done to obtain a more continuous curve.

For simplicity, κ was set to zero. In the next paragraph, the impact of several ideal IRs will be considered for the three scenarios.

Impact of ideal IR on cell performance

This section considers the impact of the inclusion of an ideal IR in the simulations of the different scenarios introduced in Section 5.2.1. To have an idea about the impact of such an IR in the current map of the tandem, Figure 5.17 plots the short-circuit current distribution of scenario 2 with ideal IRs with $\lambda_t \in (650 \text{ nm}, 700 \text{ nm})$.

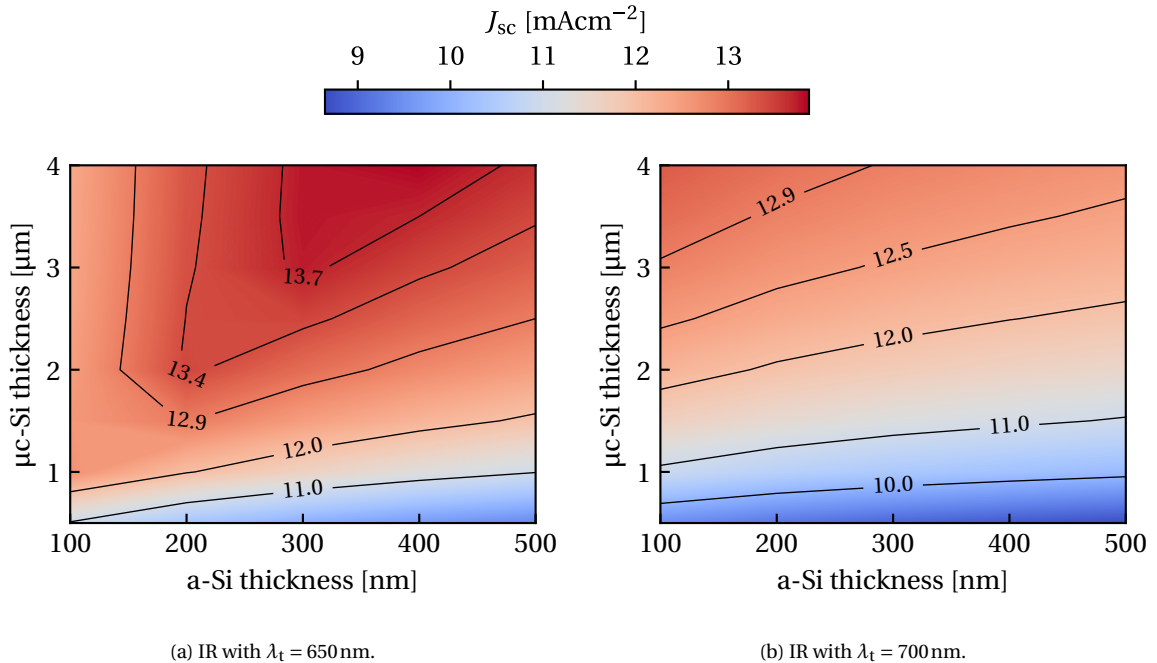


Figure 5.17: Short-circuit currents of a micromorph device in scenario 2 with different choices of IR.

These plots can be directly compared to the top right plot of Figure 5.7, where the same simulation structure is used without an IR (taking into consideration that the colour scale is different). The current matching condition could be found by joining the points where the contour lines change from a vertical to a more horizontal orientation. For $\lambda_t = 650 \text{ nm}$, this line has shifted towards thicker bottom cells and thinner top cells. This is evidence for a gain in the current delivered by the top cell. Moreover, this new light management results in a higher total current of the tandem. For the sake of comparison, at a top cell/bottom cell thickness combination of $200 \text{ nm}/2 \mu\text{m}$, the inclusion of this IR results in a short-circuit current of 13.5 mAcm^{-2} , whereas only 12.3 mAcm^{-2} could be achieved without the IR. For an inappropriate choice of λ_t , the ideal IR will direct too much light to one of the subcells, which is undesirable. This was the case for $\lambda_t = 700 \text{ nm}$, for which it is clear from the orientation of the contour lines that the tandem has become mostly bottom cell limited. At the same thickness combination, $J_{sc} = 11.9 \text{ mAcm}^{-2}$.

To investigate the impact of different ideal IRs on the efficiency of the tandem, λ_t was varied between 450 nm and 700 nm with steps of 50 nm . This was done for all the considered scenarios, keeping track of the maximum efficiencies and the subcells' thicknesses at which this maximum is attained. The simulated thicknesses are again from 100 nm to 500 nm and from $0.5 \mu\text{m}$ to $4 \mu\text{m}$ for the top and bottom cell absorber layers, respectively. Figure 5.18 summarises all the results. In many cases, the maximum efficiency can be improved with the use of an intermediate reflector. This increase is dependent on the choice of λ_t , which shifts the transition from high reflectance to high transmittance. If chosen too

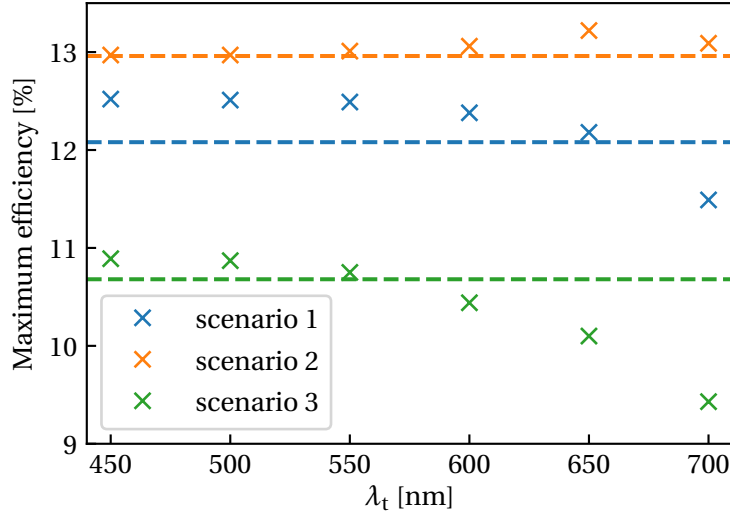


Figure 5.18: Maximum efficiency in the simulated thickness range with the use of different ideal IRs as a function of λ_t . The dashed line represents the maximum efficiency when no IR is used in each scenario.

high, it is seen to decrease the overall efficiency due to the low current production of the bottom cell. Besides the increase in efficiency, thinner top layers can be used, reducing light-induced degradation. However, this should not happen at the expense of very thick bottom layers, which poses problems in the quality of the material and the manufacturing costs. Table 5.2 summarises the thicknesses of the top and bottom cell absorber layers at which the maximum efficiencies shown in Figure 5.18 were attained.

Table 5.2: Thicknesses at which the maximum efficiency for difference scenarios is obtained, considering different ideal IRs.

λ_t [nm]	Scenario 1		Scenario 2		Scenario 3	
	Top [nm]	Bottom [μm]	Top [nm]	Bottom [μm]	Top [nm]	Bottom [μm]
450	100	3	200	1	100	4
500	100	3	200	1	100	4
550	100	3	100	0.5	100	4
600	100	3	100	0.5	100	4
650	100	3.5	100	1	100	4
700	100	4	100	3.5	100	4
No IR	100	3.5	140	0.5	100	4

As analysed in Sections 5.1.2, scenario 1 is a case with non-optimal refractive index choice of the layers at the TRJ. By including an ideal IR, the best efficiency boost was from 12.1 % to 12.5 %, also reducing the bottom cell thickness from 3.5 μm to 3 μm . The light management for scenario 3 was even worse. Here, the best gain in maximum efficiency was from 10.7 % to 10.9 %, for the minimum/maximum thickness combination of top/bottom cell. This has to do with the fact that a lot of reflection is happening in layers outside the TRJ, so the effect of the IR is minimal. Finally, scenario 2 proves what is ideally achieved

with an intermediate reflector. The maximum efficiency increases from 13 % to 13.2 % for a thinner top cell and a similar bottom cells thickness.

It has to be taken into consideration that the improvement of efficiencies with ideal intermediate reflectors cannot be translated directly to measurable data. The IRs introduced in this section present the ideal refractive indices for maximum/minimum reflection for low/high wavelengths. In reality, materials with such optical characteristics do not exist. Therefore, the results obtained indicate the maximum increase in efficiency that can be attained with an intermediate reflector and what the effect on the subcell thicknesses is. This can then serve as the grounds for deciding whether it is worth to include an intermediate reflector in the manufacturing of a device, considering the added production costs and time that can be associated with such an extra layer. If an IR is included, the closeness of its refractive index to the ideal case will determine the degree to which the efficiency will be increased and the subcell thicknesses varied.

5.3. Region of interest for micromorph R2R production

In this section, some aspects relevant to the micromorph module delivered by HyET Solar are discussed. First, the inclusion of the newly developed texture is compared to the baseline texturing currently implemented in their manufacturing process. Second, the encapsulation at the front side of the tandem is incorporated in the modelling, along with an adjustment of cell parameters that can be expected under operation. With this, realistic predictions of the output efficiency can be made. The thickness range of the simulations in this section are focused on the regions of interest of HyET, which considers a maximum bottom cell thickness of 2 μm to ensure a high throughput and limit production costs. Moreover, the optical structure of scenario 2 is used in this section given that it was the best case found in Section 5.2.

5.3.1. Texturing comparison

The current texturing in the roll-to-roll processing at HyET is done with a 0.1 M solution of NaOH at 35 $^{\circ}\text{C}$. This baseline procedure results in less surface roughening of the temporary Al foil than the MST developed within the FlamingoPV project. This can have large effects on the optical path length of light in the cell and therefore the absorption that can take place. Table 5.3 compares the *root mean square* (RMS) roughness R_{rms} and correlation length L_c of the considered textures.

Table 5.3: Parameters describing the baseline texturing at HyET and one developed within the FlamingoPV project.

Texture	R_{rms} [nm]	L_c [μm]	R_{rms}/L_c [-]
HyET baseline	28.4	0.497	0.057
FlamingoPV	418	5.235	0.080

The roughness of the surface features result in a mostly diffractive scattering for the baseline texturing and a refractive one for the FlamingoPV case. To analyse the impact of the texturing on the absorption in the subcells, Figure 5.19 plots the absorption profile for both textures for a sample micromorph cell (top cell/bottom cell thickness of 200 nm/1 μm).

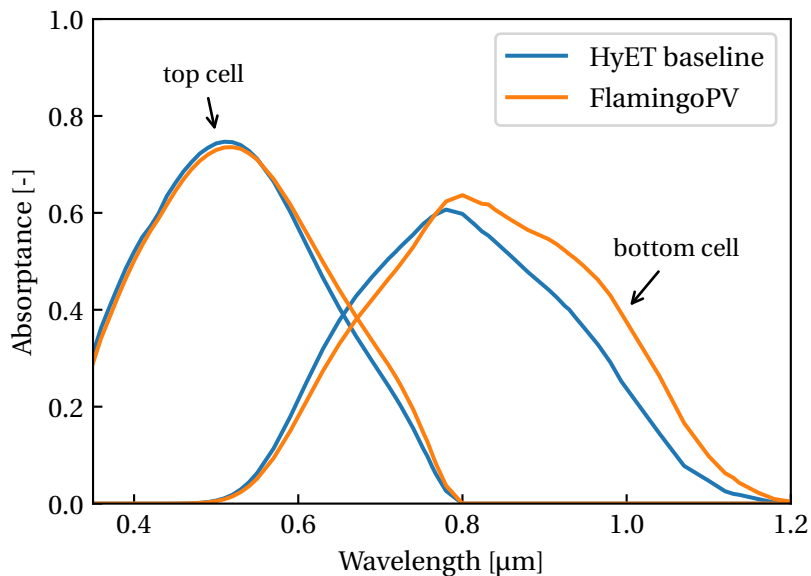


Figure 5.19: Absorbance profiles of the subcells in a micromorph device for different interface textures. Top/bottom cell thicknesses: 200 nm/1 μm .

The increased response of the bottom cell for large wavelengths is remarkable. This has to do with the implementation of a modulated surface texture in the FlamingoPV case, which creates micro-sized craters that enhance scattering for large wavelengths. On the other hand, for small wavelengths the baseline texturing of HyET seems to do a better job. The nano-morphology in this case boosts the response for wavelengths below 550 nm. From this point until 800 nm, scattering in the top cell is better for the FlamingoPV texturing, such that a lower response is seen in its bottom cell. Nevertheless, this decrease is recovered by wavelengths longer than 800 nm.

Besides the enhanced absorption as a consequence of the MST, it is also a more suitable growth substrate, specifically for the $\mu\text{c-Si:H}$ absorber layer. It has been studied that sharp features result in defective filaments in the material that deteriorate both the V_{oc} and FF , whereas a micro surface texture allows the growth of thick, defective-free layers [76]. All in all, the use of MST has a positive effect on the performance of the micromorph cell. Simulated efficiencies for several thickness combinations are plotted in Figure 5.20. The comparison of the other performance indicators of the cell are shown in Appendix F.

As expected, higher efficiencies are achieved with the new texturing when compared to HyET's baseline. For the simulated thicknesses, a maximum efficiency of 13 % is registered for the first case and 12.3 % for the second. These values were obtained at top cell/bottom cell thicknesses of 140 nm/0.5 μm and 180 nm/0.9 μm , respectively. The overall increase of the efficiency is therefore a combination of a boost in short-circuit current as well as the improved electrical properties given the reduction in subcell thicknesses.

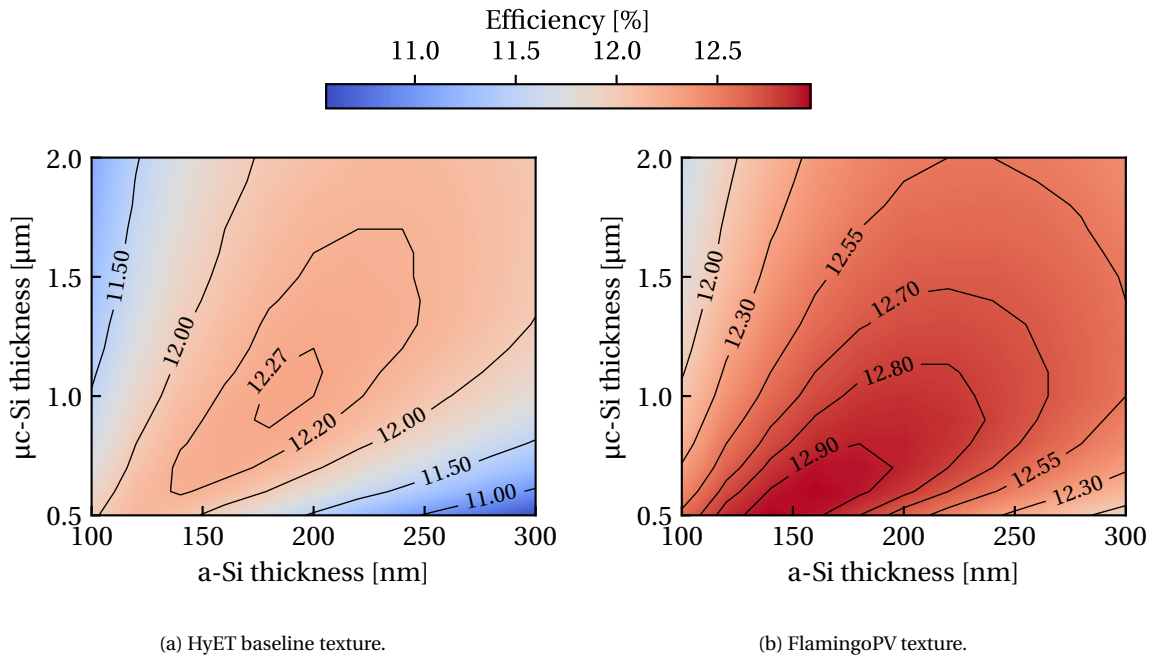


Figure 5.20: Comparison of the efficiencies as a function of the subcell thicknesses for the baseline texturing at HyET and the developed texture for FlamingoPV.

5.3.2. Encapsulated cell performance prediction

The module structure used throughout this chapter, presented in Figure 5.1, has FTO as the front layer. In reality, the final product delivered by HyET is encapsulated. Besides providing protection from the environment, this encapsulation improves light management by reducing the reflection at the front of the cell. This section will include this encapsulation in the modelling of the tandem to provide a realistic prediction of the efficiency of such a cell. Figure 5.21 shows the layers that are added on top of the FTO in the encapsulation process along with an approximation of the thicknesses.

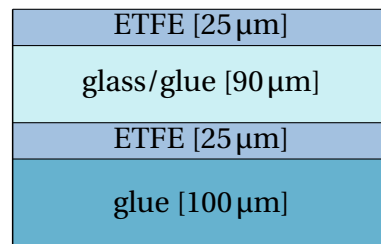


Figure 5.21: Structure of the front encapsulation used by HyET Solar. The layer thicknesses are not to scale.

The ethylene tetrafluoroethylene (ETFE) layers have a refractive index of 1.43, and the glass/glue combination and pure glue layer 1.53. All these layers have a negligible absorption, so they are modelled with an absorption index equal to zero. The full stack of layers is then the one shown in Figure 5.21 on top of the one in Figure 5.1. The performance of this structure is shown in Figure 5.22.

When compared to the cell without encapsulation, a remarkable efficiency increase of 0.8% absolute to 13.8% is experienced, at an optimal thickness combination of 160 nm/0.6 μm for the top/bottom cell. This is mainly a consequence of the increase in light cou-

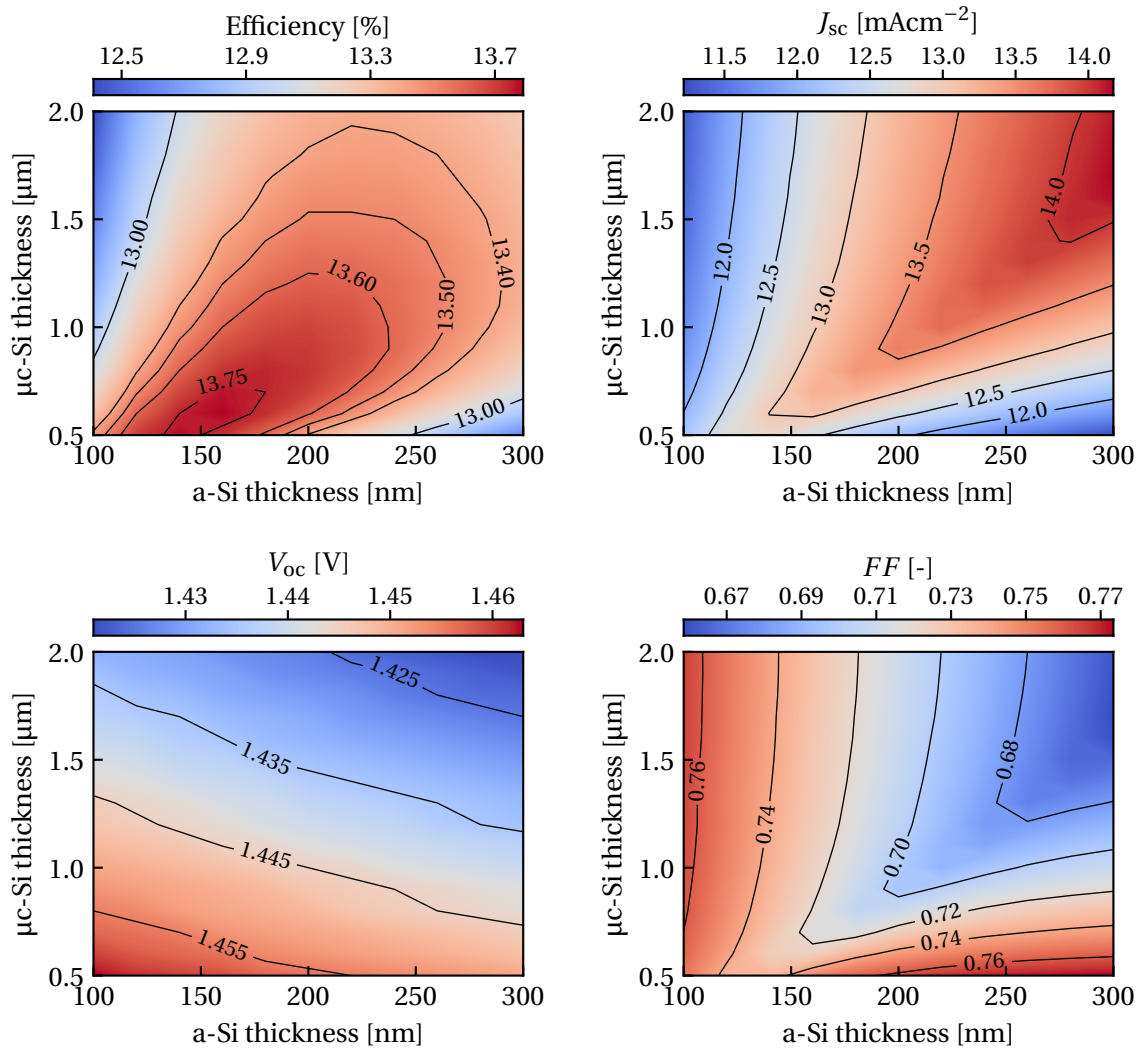


Figure 5.22: Simulated encapsulated micromorph solar cell parameters for different absorber layer thicknesses.

pling, since the encapsulation decreases the reflectance. This effect is shown in Figure 5.23 for a top/bottom cell thickness of 200 nm/1 μm.

Towards a more realistic prediction

It has to be taken into consideration that this high performance is based on some assumptions, as mentioned in Section 5.1.1. First of all, the fact that the initial texturing of the Al foil is adapted perfectly to all the interfaces of the device. This results in an overestimation of mainly the current of the subcells. In order to have an even more realistic performance prediction of the encapsulated micromorph cell, this aspect will be taken into consideration in this paragraph.

Analysis have shown that the J_{sc} of an a-Si:H cell could be overestimated around 1 mAcm⁻¹ [77] for a 700 nm thick absorber layer. Considering that the thickness range in the studied micromorph cell is less than half, this drop is estimated to be 0.5 mAcm⁻¹. For the bottom cell this drop can be expected to be higher, given that the texturing has a larger impact on the absorption of this material. Therefore, a decrease of 1 mAcm⁻¹ is consid-

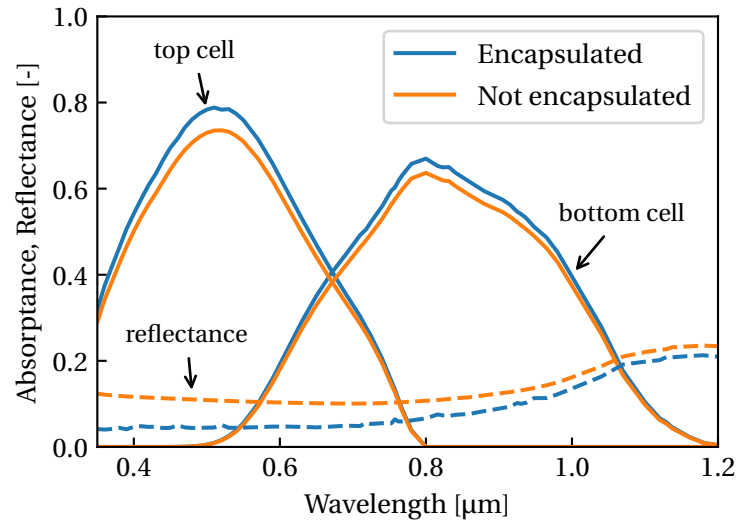


Figure 5.23: Absorbance profiles (continuous lines) of the subcells in a micromorph device and total reflectance (dashed lines) for different interface textures. Top/bottom cell thickness: 200 nm/1 μm .

ered. To include this effect on the performance of the device, the short-circuit currents of the each subcell was computed and shifted accordingly. Then, the efficiency of the total device is taken as the multiplication of the minimum current between the shifted values of the subcells, the V_{oc} and the FF of the tandem, divided by the incoming power. This plot is shown in Figure 5.24.

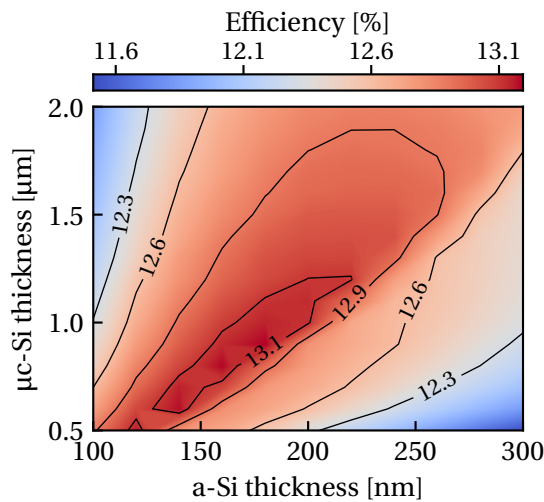


Figure 5.24: A more realistic prediction of the efficiency of the encapsulated cell after considering lower short-circuit currents of the subcells.

The maximum efficiency in this case is 13.2 % at a top/bottom cell thickness of 180 nm/0.9 μm . At this point, $J_{sc} = 12.85 \text{ mAcm}^{-2}$, $V_{oc} = 1.449 \text{ V}$ and $FF = 0.709$. The change in currents has therefore shifted the best operational range to thicker absorber layers. On a final note, the FF and V_{oc} are also expected to change in this new current distribution, but the computation is less straightforward. Therefore, this change is not considered in this approximation. To ultimately obtain a better estimation of the performance, an AFM scan

of the morphology of each interface in the complete stack should be done and included in the simulations. The efficiency predictions in Figure 5.24, however, serve as a good starting point of the achievable efficiency values and the corresponding absorber layers' thicknesses.

5.4. Further optical improvements

AZO/Al is used as a back reflector due to its efficient reflection and the abundance of materials, which makes them affordable for the production chain. Nevertheless, Ag has better optical properties in terms of back reflection. The encapsulation used by HyET provides a reduced reflection at the front of the cell, given that its refractive index is in between that of air and FTO. However, we can think of a perfect optical encapsulation, which has the ideal optical properties such that the condition of minimum reflection is achieved. This is accomplished by following the square root of the product of the refractive index of air and TCO [8]. In this section, this ideal encapsulation, along with Ag as back reflector, are considered as a demonstration of how the product delivered by HyET could be enhanced. The absorbance of the subcells and the total reflectance for the HyET product and the improvements mentioned are plotted in Figure 5.25 for a top/bottom cell thickness combination of 200 nm/1 μm .

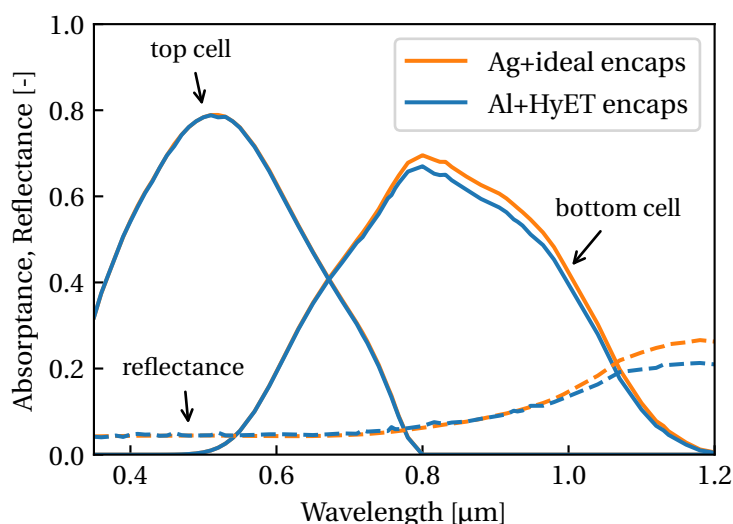


Figure 5.25: Absorbance profiles (continuous lines) of the subcells in a micromorph device and total reflectance (dashed lines) for an ideal encapsulation with Ag as back reflector and the encapsulation used at HyET with AZO/Al as back reflector. Top/bottom cell thickness: 200 nm/1 μm .

From the reflectance curves, it is evident that the encapsulation used at HyET provides a very good light coupling and matches the profile an ideal, single-layer encapsulation would have at low wavelengths. Therefore, the absorption profile of the top cell is unchanged. When including Ag as back reflector, an enhanced absorption of the bottom cell from about 750 nm onwards is experienced given the superior optical properties of this material. The increase in reflectance starting at a wavelength of 1 μm is a consequence of light passing through the stack of layers twice without being absorbed.

Figure 5.26 shows the performance of the cell with Ag as back reflector and ideal encapsulation.

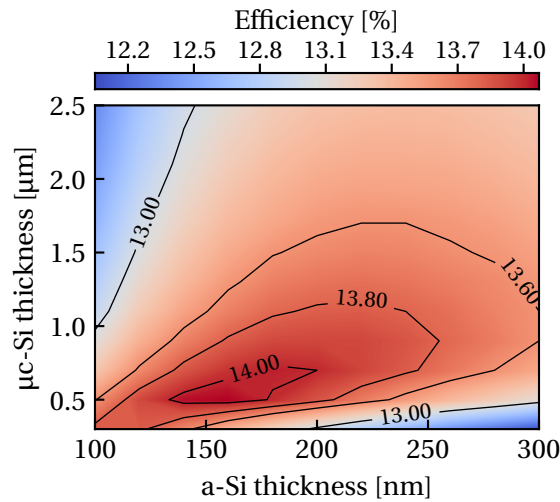


Figure 5.26: Efficiency prediction of a micromorph cell with an ideal encapsulation and Ag as back reflector.

The maximum efficiency of 14.1 % is achieved at a top/bottom cell thickness combination of 160 nm/0.5 μm. When compared to the 13.8 % at similar thicknesses in the original case in Figure 5.22, it can be concluded that the micromorph structure in the original case already presents very good light management. With this in mind, the impact of including this ideal encapsulation and Ag as back reflector is minor and might not justify the production costs related to its implementation.

6

Preliminary experimental results

This chapter presents introductory results regarding the manufacturing of devices on Al foil substrates. In Section 6.1, the material properties and diode characteristics of single-junction a-Si:H cells are verified. Then, some multi-junction devices are visually presented in Section 6.2.

6.1. Amorphous silicon depositions

The PECVD recipe presented in Section 3.2.2 is used for the deposition of *pin* a-Si:H cells on textured Al foil to verify its validity when deposited on such substrates. Due to time constraints, the complete processing of deposited cells, which results in a working solar cell, was not possible. Therefore, the performance of the cells under illumination could not be measured. However, the material quality could be investigated, as well as the diode behaviour of the *pin* structure. These analyses are presented next.

6.1.1. Raman spectra

To ensure the deposition of amorphous silicon material on the Al substrate, Raman measurements were performed. The wavelength of the laser light of the measuring setup was 633 nm at a power of 1 %, with an exposure time of 100 s. The spectra at a thickness of 250 nm and 500 nm are presented in Figure 6.1.

It is clear from the peaks centred at a Raman shift of 480 cm^{-1} that the material is fully amorphous, as there are no enhanced counts at the crystallinity peak at 521 cm^{-1} . This is the case for both thicknesses, giving an indication that the material is amorphous throughout the layer.

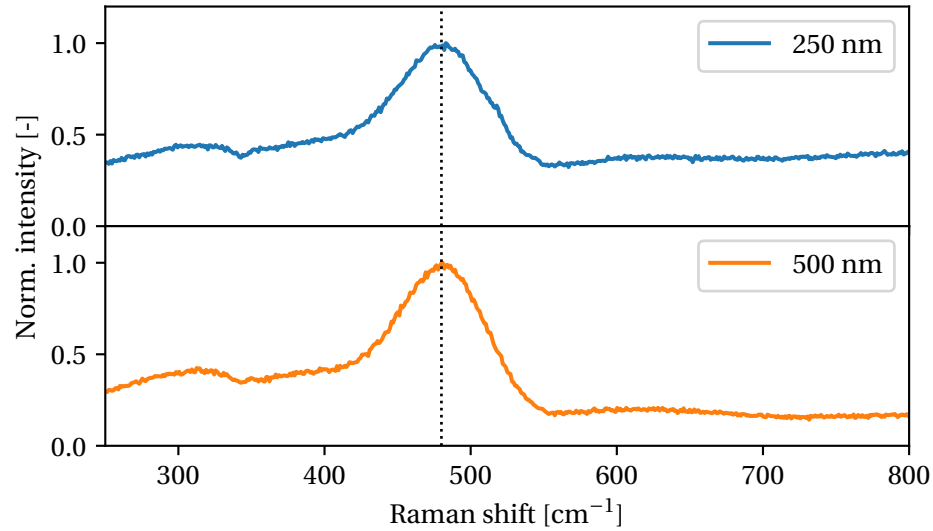


Figure 6.1: Raman spectra of intrinsic a-Si:H with thicknesses of 250 nm and 500 nm. The vertical dotted line is placed at a Raman shift of 480 cm^{-1} .

6.1.2. Dark $I - V$ measurements

To ensure a diode behaviour, the current as a function of voltage of a Al/AZO/a-Si:H(pin)/Al stack was measured under dark conditions. The back Al was evaporated with a mask, such that contact points of 1 cm^2 are formed. Figure 6.2 plots the results for the measurement at three contact points on the same foil.

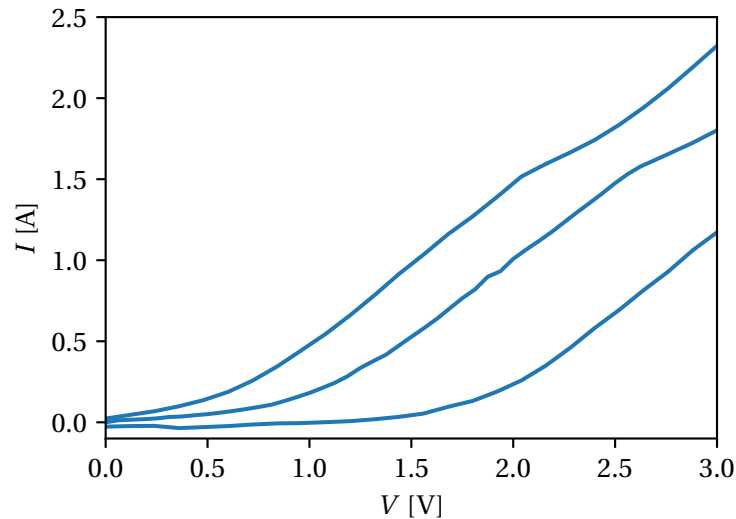


Figure 6.2: Dark $I - V$ characteristic of three *pin* a-Si:H cells.

The behaviour of a diode is clear from the $I - V$ characteristic, but the differences between contact points on the same substrate are notable. This can be attributed to several reasons. To start, it was often the case that the Al foil was not completely clean after the texturing procedure as a consequence of etching residues. Careful wiping was performed to cleanse the surface of the foil before the depositions, but it might not have been sufficient. Moreover, it was a difficult task to maintain the substrates completely flat during the de-

positions, which might have caused material inhomogeneities across the substrate. These factors can manifest themselves as added resistances in the diode, causing the behaviour observed in Figure 6.2.

Despite these limitations, the measured shunt resistance of a-Si:H cells deposited at the facilities of EKL in Delft on textured Al foils were significantly higher than those produced at HyET Solar. This is an indication of high performance cells. Figure 6.3 shows these results in a box plot.

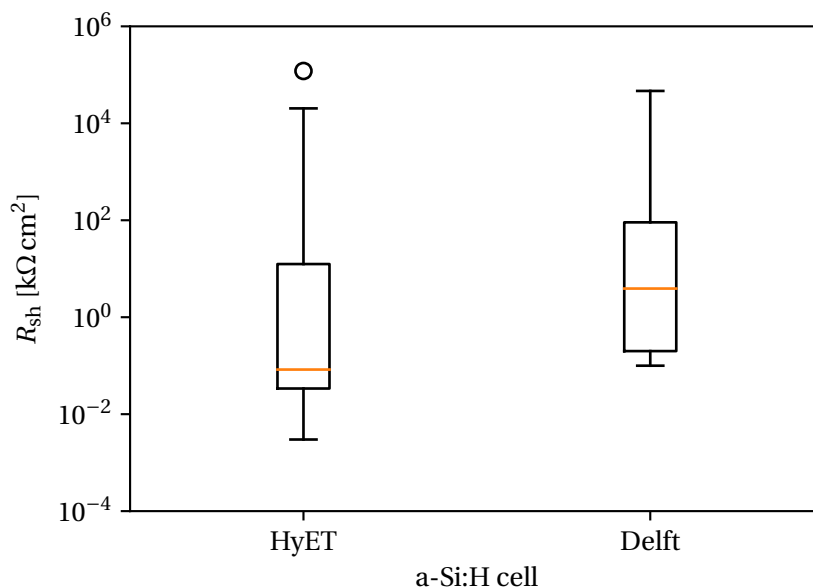


Figure 6.3: Comparison of the measured shunt resistance of a-Si:H cells produced at HyET Solar and at Delft on a textured Al substrate.

The spread of the shunt resistances is similar in both cases, evidencing the inhomogeneities mentioned above. Nevertheless, the cells deposited at Delft have a median that is around two orders of magnitude higher than those deposited at HyET Solar.

6.2. Multi-junction depositions

This section presents SEM cross-section images of an a-Si:H/ μ c-Si:H tandem and an a-Si:H/ μ c-Si:H/ μ c-Si:H triple-junction device, which are both relevant for the FlamingoPV project. With the help of such images, the ability to grow thick μ c-Si:H layers can be inspected by checking the absence of voids in the material, which act as recombination centres and results in a drop in the V_{oc} . The recipe for the deposition of μ c-Si:H cells was optimised by S. Nawaratne [81].

Figures 6.4 and 6.5 show a tandem and triple-junction cell deposited on textured Al foils. Regarding the tandem, the thicknesses of the AZO, a-Si:H and μ c-Si:H layers can be estimated to be 540 nm, 250 nm and 1.83 μ m. For the triple junction, the AZO, a-Si:H, middle μ c-Si:H and bottom μ c-Si:H layers can be estimated to be 650 nm, 200 nm, 1.09 μ m and 1.63 μ m thick from the SEM image. In both cases, a visual inspection gives the conclusion that there are a limited number of voids present in the material, evidencing the potential of the implemented texturing for the growth of thick μ c-Si:H layers.

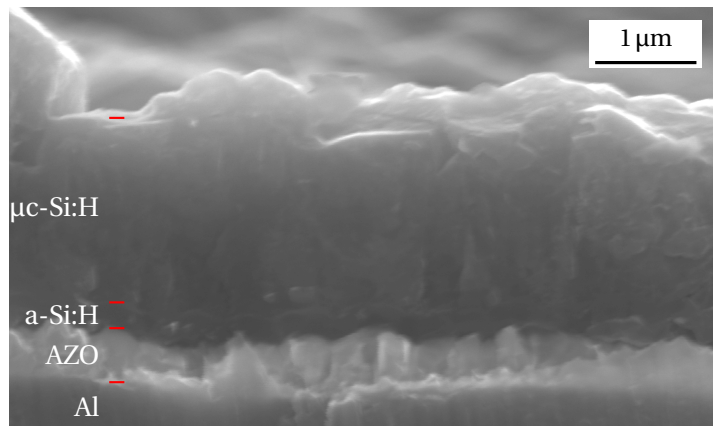


Figure 6.4: SEM cross-section image of a micromorph tandem deposited on a textured Al foil substrate, taken by G. Limodio.

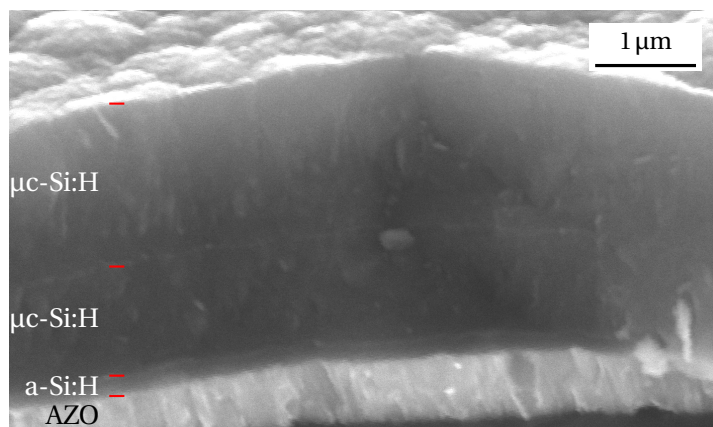


Figure 6.5: SEM cross-section image of an a-Si:H/ $\mu\text{c-Si:H}$ / $\mu\text{c-Si:H}$ triple-junction deposited on a textured Al foil substrate, taken by G. Limodio.

7

Conclusions and outlooks

This thesis investigated the possibility of developing high-efficiency flexible thin-film silicon solar cells. For this, modelling was used for the prediction and optimisation of the operation of an amorphous silicon/microcrystalline silicon tandem device. This chapter discusses the most important conclusions from this work, together with an outlook of future research directions in line with this area of study.

7.1. Conclusions

As a semiconductor modelling software, ASA is valuable for the prediction of the operation of a solar cell under different circumstances. For it to be used efficiently, an understanding of the impact of physical values on the outcome of the simulations is indispensable. To achieve this, a comprehensive study was carried out on the sensitivity of the cell performance on the physical model parameters, which is a valuable tool when calibrating the model to match experimental results. By developing a Python-based automating routine for the web interface of ASA, the execution of new simulations could be processed quickly and autonomously.

The sensitivity analysis provided the proper insights for the calibration of single-junction amorphous silicon and microcrystalline silicon solar cell models, with reference efficiencies of 7.7 % and 9.4 %, respectively. When combining these models for the performance prediction of the multi-junction micromorph cell (top amorphous silicon/bottom microcrystalline silicon tandem), it was found that the choice of optical properties of the layers at the junction between the subcells has a critical effect on the light distribution of the device. If the refractive indices of the layers at the junction vary too much from the values of the absorber layers, the high reflection taking place limits the current production of the bottom cell. This limits the overall performance of the device and increases the thickness of the bottom cell absorber layer, compromising its implementation on a large scale setting. Considering, for instance, a micromorph cell with top and bottom cell thicknesses of 200 nm and 2 μm , respectively: the efficiency can be brought up from 9.6 % to 12.5 % by using layers at the junction with refractive indices closer to that of the absorber layers.

Intermediate reflectors are often used in multi-junction solar cells for an improved light distribution. In this work, the optimal conditions for an ideal intermediate reflector were examined, by analysing the reflectance and transmittance for different combinations of refractive indices. This provided the ideal refractive index an intermediate reflec-

tor should have in order to maximise the reflectance/transmittance below/above a certain wavelength, which mimics the perfect operation of such a reflector. The results can be used to predict the maximum increase in efficiency the inclusion of an intermediate reflector can produce and the influence on the absorber layers' thicknesses. This is a decisive factor when considering the implementation on a large scale facility, because the increase in device performance must justify the added production costs and manufacturing time.

In a scenario with a mismatch of the refractive indices at the junction layers, maximum efficiencies could be improved from 12.1 % to 12.5 % at bottom cell thicknesses of 3.5 μm and 3 μm , respectively. In such a case, including an intermediate reflector could have a considerable benefit. However, for an already high-performing device with an efficiency of 13 %, the inclusion of an ideal intermediate reflector only increased the efficiency to 13.2 %, at similar bottom cell thicknesses. This minor improvement might not be worth the investment. The analysis can be expanded to tandem devices in general, serving as a guideline for predicting the impact of intermediate reflectors.

All these observations provided the necessary information for the determination of the micromorph configuration that maximises the conversion efficiency. For a typical cell structure and encapsulation from HyET Solar, an efficiency of 13.2 % ($J_{\text{sc}} = 12.85 \text{ mA cm}^{-2}$, $V_{\text{oc}} = 1.449 \text{ V}$, $FF = 0.709$) is predicted without an intermediate reflector. This performance is attained at a top cell absorber layer thickness of 180 nm and a bottom cell of 0.9 μm . This prediction takes into account an overestimation of the current from the results of the simulation. Such a high performing device at reasonable thicknesses is attributed to the combination of a modulated surface texture to enhance light absorption, the use of thin layers which result in a high V_{oc} and FF , and the use of proper front encapsulation layers to minimise reflection. The use of an Ag back reflector instead of AZO/Al improved the current of the bottom cell but did not result in a significant efficiency improvement.

The fabrication of amorphous silicon cells on flexible Al substrates proved the possibility of depositing such cells at the facilities in Delft. This was evidenced in the presence of amorphous material from Raman spectroscopy measurements and the achievement of high shunt resistances. A visualisation of manufactured micromorph tandems with SEM cross-sections showed the successful deposition of such devices on a modulated surface texture on flexible Al substrates.

In conclusion, the potential efficiency of over 13 %, combined with the use of flexible, inexpensive substrates, places the investigated thin-film silicon structure in a very good position in the market. The applications for such light tandem devices are numerous and can accelerate the large scale implementation of photovoltaic solar energy for the transition to a sustainable society.

7.2. Outlooks

The conducted research in this work has highlighted the potential of the micromorph cell for its use in flexible Al substrates with the use of simulations. In this regard, some ideas are given for the further optimisation of the device.

First, the impact of the band gap variation of the amorphous silicon absorber layer on the device performance can be considered. By changing the deposition conditions, amorphous silicon layers with band gaps from around 1.7 eV to 1.9 eV can be obtained. This has an impact on the light distribution and voltages of the device and might improve the efficiency and thickness distribution of the top and bottom cell. Since the refractive index

changes for a material with a different band gap, the optical data must be obtained in each case.

Second, a complete characterisation of the interface morphology of the device is needed to accurately estimate the current production of each subcell in a tandem. In this work, an estimation was made of the excess current produced by the subcells as a consequence of using the same texture as the first layer. The information of the texture was provided by an AFM scan. In reality, the features smooth out as the layers are deposited, such that an AFM scan after the deposition of each layer would lead to an improved modelling of the morphology of the interfaces.

Third, an analysis of the tunnel-recombination junction would provide better insights on the impact of the layers forming this junction on the device performance. For instance, the consequence of the thickness variation of these layers could be investigated. Moreover, it might be necessary to adjust the tunnelling parameters of the model to mimic the behaviour of real micromorph devices more accurately.

Ultimately, the power of modelling is only fully taken advantage of when the results can be translated into measurable devices. Time limitations did not allow a full characterisation of deposited single- and multi-junction devices, which is an important step for the development of solar cells. In light of this, device fabrication and characterisation is the next step in proving the possibility of fabricating such high-efficiency devices on flexible Al substrates. During this project, the post-processing of the cells for the characterisation under illuminated conditions was done at the facilities of HyET Solar, given their expertise in these final processing stages. This included the transfer of the cell to a permanent carrier and the etching of the temporary Al foil. It might be worth looking into alternative processing procedures at the Delft facilities to speed up this final processing. Unsuccessful attempts were made within this thesis and proved that the optimisation of the final processing steps are a whole new study on its own.

Acknowledgements

Coming from an Applied Physics background, I knew from the start of my master that I wanted to do a thesis in solar energy, as I have always found it a fascinating way of powering the world. I am very happy I chose to do this at the PVMD group. First of all, I would like to thank Prof. Arno Smets for giving me the opportunity to carry out my thesis under his supervision. Despite coming from a different master programme than usual for the PVMD group, he welcomed me straight away. I would also like to thank Dr. Gianluca Limodio for his guidance on a day-to-day basis and for always being available for discussions and questions. To Sajith Nawaratne and Devika Rajagopal, I had a great time working on FlamingoPV with you. Thank you for the interesting discussions, both scientific and non-scientific.

In general, I would like to thank the whole PVMD group for the support when I needed it. My special gratitude goes to Dr. Carlos Ruiz, who assisted me on many occasions with ASA. Thank you to PhD student Thierry de Vrijer and the team from the DISCO project for sharing information on thin-film processing. Also, to Martijn Tijssen and the team from EKL for their invaluable support during the lab activities. This project would not have been possible without the knowledge provided by HyET Solar, from which I would like to give my special thanks to Dr. Davide Bartesaghi and Dr. Edward Hamers. In addition, I would like to thank Dr. Rudi Santbergen and Dr. Arjan Houtepen for forming part of my examination committee.

Finally, I would like to thank my family, friends and girlfriend for their continuous love and belief in me. I hope this thesis marks the start of my journey towards shaping a sustainable future.

Erik Spaans
May 28, 2020
Delft, The Netherlands



ASA .cas files

A.1. Reference

C Reference ASA simulation file for a-Si:H pin cell;

```
C DEVICE DEFINITION;
layers electrical=3 front=2 back=1;
grid[f.1] d=1.5e-3;
grid[f.2] d=650.0e-9;
grid[1] d=10e-9 spaces=20;
grid[2] d=450e-9 spaces=200;
grid[3] d=20e-9 spaces=40;
grid[b.1] d=300.0e-9;

C OPTICAL PARAMETERS OF LAYERS;
optical[f.1] ext.coeff=0 ref.index=1.5 incoherent; C glass;
optical[f.2] lnk.file=tud_SnO-Asai.in; C tco;
optical[1] lnk.file=tud_p-aSiC.in; C p-layer;
optical[2] lnk.file=tud_i-aSi.in; C i-layer;
optical[3] lnk.file=tud_n-aSi.in; C n-layer;
optical[b.1] lnk.file=tud_ag.in; C back contact;

C INTERFACE TEXTURING;
interface[i.3] adf.s.rf=cossq adf.s.rb=cossq adf.s.tf=cossq adf.s.tb=cossq;
interface[i.3] adf.h.rf=cossq adf.h.rb=cossq
adf.h.tf=cossq adf.h.tb=cossq adf.h.file=sct_t-p.in;
interface[i.6] adf.s.rf=cossq adf.s.rb=cossq adf.s.tf=cossq adf.s.tb=cossq;
interface[i.6] adf.h.rf=user adf.h.rb=user adf.h.tf=user adf.h.tb=user
adf.h.file=sct_n-m.in;

C MATERIAL PARAMETERS OF LAYERS;
bands[1] e.mob=1.85 chi=4.000 nc=6.0E+26 nv=6.0E+26 epsilon=7.2;
bands[2] e.mob=1.75 chi=4.025 nc=6.0E+26 nv=6.0E+26 epsilon=11.9;
bands[3] e.mob=1.75 chi=4.025 nc=6.0E+26 nv=6.0E+26 epsilon=11.9;

mobility[1] mu.e=10.0e-4 mu.h=1.0e-4;
```

```
mobility[2] mu.e=20.0e-4 mu.h=5.0e-4;
mobility[3] mu.e=10.0e-4 mu.h=1.0e-4;

doping[1] e.act.acc=0.50;
doping[3] e.act.don=0.30;

variable SIGMA1=0.7e-15 SIGMA2=SIGMA1/10;

C DENSITY OF STATES PARAMETERS OF LAYERS;
vbtail[all] levels=20 c.neut=SIGMA1 c.pos=SIGMA2 e.range=1.0;
vbtail[1] n.emob=1e28 e.char=0.100;
vbtail[2] n.emob=4e27 e.char=0.045;
vbtail[3] n.emob=1e28 e.char=0.090;

cbtail[all] levels=15 c.neut=SIGMA2 c.neg=SIGMA1 e.range=0.7;
cbtail[1] n.emob=8e27 e.char=0.080;
cbtail[2] n.emob=2e27 e.char=0.027;
cbtail[3] n.emob=1e28 e.char=0.070;

dbond[all] levels=20 e.corr=0.2 d.e=0.2 e.range=4.0 e.rel.mg=0
ce.pos=5e-13 ce.neut=5e-14
ch.neg=5e-13 ch.neut=5e-14;
dbond[1] n=8.0e24;
dbond[2] n=5.0e21;
dbond[3] n=2.0e25;

C GENERAL SETTINGS;
settings newton gummel.starts=2 max.step.reduc=0;
settings damp=6 max.iter=50;
model amorphous;

C CALCULATING GENERATION PROFILE;
opticgen spectrum=am15_350-1200.in gp3;
print opticgen file=opticgen.dat;
print absorption file=absorption.dat;
print absorptance file=absorptance.dat;

C CALCULATING SPECTRAL RESPONSE;
settings sr.flux=1.0e20;
solve equil;
solve sr wl.start=300nm wl.step=5nm wl.end=1200nm;
print sr file=qe_sr.dat gnu;

C CALCULATING ILLUMINATED J-V (AM1.5 simulation);
solve equil;
solve v.start=v_start v.end=v_end n.step=36 illum;
print jv file=jv_illum.dat headers=false;
print solpar file=solpar.dat;
```

A.2. Calibrated a-Si:H cell

```
C ASA simulation file match for HyET's a-Si:H pin cell;
C Calibration by Erik Spaans
```

```
C DEVICE DEFINITION;
layers electrical=3 front=2 back=2;
grid[f.1] d=700.0e-9;
grid[f.2] d=20.0e-9;
grid[1]    d=10e-9 spaces=20;
grid[2] d=300e-9 spaces=200;
grid[3] d=10e-9 spaces=40;
grid[b.1] d=80e-9;
grid[b.2] d=300.0e-9;
```

```
C OPTICAL PARAMETERS OF LAYERS;
optical[f.1] lnk.file=FTO.in; C front TCO;
optical[f.2] lnk.file=AZO.in; C AZO buffer layer;
optical[1] lnk.file=a-SiC(p).in; C p-layer;
optical[2] lnk.file=a-Si(i).in; C i-layer;
optical[3] lnk.file=a-Si(n).in; C n-layer;
optical[b.1] lnk.file=AZO.in; C back TCO;
optical[b.2] lnk.file=Al.in; C back contact;
```

```
C INTERFACE TEXTURING;
interface[i.3] adf.s.rf=linear adf.s.tb=linear;
interface[i.3] adf.h.file=sct_t-p.in;
interface[i.6] adf.s.rf=cossq adf.s.rb=cossq adf.s.tf=cossq;
interface[i.6] adf.h.rf=user adf.h.rb=user adf.h.tf=user
adf.h.tb=user adf.h.file=sct_t-p.in;
```

```
C MATERIAL PARAMETERS OF LAYERS;
bands[1] e.mob=1.98 chi=0.000 nc=2.0E+26 nv=2.0E+26 epsilon=11.9;
bands[2] e.mob=1.70 chi=0.025 nc=2.0E+26 nv=2.0E+26 epsilon=11.9;
bands[3] e.mob=1.75 chi=0.025 nc=2.0E+26 nv=2.0E+26 epsilon=11.9;
```

```
mobility[1] mu.e=10.0e-4 mu.h=1.0e-4;
mobility[2] mu.e=20.0e-4 mu.h=5.0e-4;
mobility[3] mu.e=10.0e-4 mu.h=1.0e-4;
```

```
doping[1] e.act.acc=0.50;
doping[3] e.act.don=0.25;
```

```
variable SIGMA1=0.7e-15 SIGMA2=SIGMA1/10;
```

```
C DENSITY OF STATES PARAMETERS OF LAYERS;
vbtail[all] levels=20 c.neut=SIGMA1 c.pos=SIGMA2 e.range=1.0;
vbtail[1] n.emob=1e28 e.char=0.100;
vbtail[2] n.emob=4e27 e.char=0.05;
vbtail[3] n.emob=1e28 e.char=0.090;
```

```

cbtail[all] levels=15 c.neut=SIGMA2 c.neg=SIGMA1 e.range=0.7;
cbtail[1] n.emob=8e27 e.char=0.080;
cbtail[2] n.emob=2e27 e.char=0.027;
cbtail[3] n.emob=1e28 e.char=0.070;

dbond[all] levels=20 e.corr=0.2 d.e=0.2 e.range=4.0 e.rel.mg=0
ce.pos=1e-14 ce.neut=5e-14
ch.neg=5e-13 ch.neut=5e-14;
dbond[1] n=1.0e24;
dbond[2] n=2.0e21;
dbond[3] n=2.0e25;

C GENERAL SETTINGS;
settings newton gummel.starts=2 max.step.reduc=0;
settings damp=6 max.iter=50;
model amorphous;

C CALCULATING GENERATION PROFILE;
opticgen spectrum=am15_350-1200.in gp3;
print opticgen file=opticgen.dat;
print absorption file=absorption.dat;
print absorptance file=absorptance.dat;

C CALCULATING SPECTRAL RESPONSE;
settings sr.flux=1.0e20;
solve equil;
solve sr wl.start=300nm wl.step=5nm wl.end=1200nm illum;
print sr file=qe_sr.dat;

C CALCULATING ILLUMINATED J-V (AM1.5 simulation);
solve equil;
solve v.start=0 v.end=0.9 n.step=50 illum;
print jv file=jv_illum.dat;
print solpar file=solpar.dat;

```

A.3. Calibrated $\mu\text{c-Si:H}$ cell

```

C ASA simulation file match for H. Tan's nc-Si:H pin cell;
C Calibration by Erik Spaans

C DEVICE DEFINITION;
layers electrical=3 front=2 back=2;
grid[f.1] d=1.5e-3;
grid[f.2] d=600e-9;
grid[1] d=20e-9 dx.t=0.5e-9;
grid[2] d=3000e-9 dx.t=1e-9 dx.c=30e-9 dx.b=1e-9;
grid[3] d=50.0e-9 dx.t=1e-9;
grid[b.1] d=300e-9;

```

```
C OPTICAL PARAMETERS OF LAYERS;
optical[f.1] ext.coeff=0 ref.index=1.5 incoherent; C glass;
optical[f.2] lnk.file=AZO.in; C AZO buffer layer;
optical[1] lnk.file=nc-SiOx(p)_match.in; C p-ncSi;
optical[2] lnk.file=nc-Si(i).in; C i-ncSi;
optical[3] lnk.file=nc-SiOx(n)_match.in; C n-ncSi;
optical[b.1] lnk.file=tud_ag.in; C back contact;

C INTERFACE TEXTURING;
interface[i.2] adf.s.rf=user adf.s.rb=user adf.s.tf=user adf.s.tb=user;
interface[i.2] adf.h.rf=cossq adf.h.rb=cossq adf.h.tf=cossq adf.h.tb=cossq;
interface[i.2] afm.file=AFM_FTO.in afm.size=40e-6;
interface[i.3] adf.s.rf=user adf.s.rb=user adf.s.tf=user adf.s.tb=user;
interface[i.3] adf.h.rf=cossq adf.h.rb=cossq adf.h.tf=cossq adf.h.tb=cossq;
interface[i.3] afm.file=AFM_FTO.in afm.size=40e-6;
interface[i.6] adf.s.rf=user adf.s.rb=user adf.s.tf=user adf.s.tb=user;
interface[i.6] adf.h.rf=cossq adf.h.rb=cossq adf.h.tf=cossq adf.h.tb=cossq;
interface[i.6] afm.file=AFM_FTO.in afm.size=40e-6;

C MATERIAL PARAMETERS OF LAYERS;
bands[1] e.mob=1.90 chi=4.000 nc=4.0e26 nv=4.0e26 epsilon=11.9;
bands[2] e.mob=1.12 chi=4.000 nc=2.5e25 nv=2.5e25 epsilon=11.9;
bands[3] e.mob=1.75 chi=4.275 nc=4.0e26 nv=4.0e26 epsilon=11.9;

mobility[1] mu.e=10.0e-4 mu.h=1.0e-4;
mobility[2] mu.e=75.0e-4 mu.h=30.0e-4;
mobility[3] mu.e=10.0e-4 mu.h=1.0e-4;

doping[1] e.act.acc=0.20;
doping[3] e.act.don=0.10;

C DENSITY OF STATES PARAMETERS OF LAYERS;
vbtail[all] e.range=0.9 levels=50 c.neut=0.7e-15 c.pos=0.7e-15;
vbtail[1] n.emob=1.0e28 e.char=0.085;
vbtail[2] n.emob=2.0e25 e.char=0.015;
vbtail[3] n.emob=1.0e28 e.char=0.090;

cbtail[all] e.range=0.9 levels=50 c.neut=0.7e-15 c.neg=0.7e-15;
cbtail[1] n.emob=1.0e28 e.char=0.080;
cbtail[2] n.emob=1.0e26 e.char=0.010;
cbtail[3] n.emob=1.0e28 e.char=0.080;

dbond[all] levels=40 e.corr=0.2 d.e=0.144 e.range=5.0;
dbond[all] ce.neut=3.0e-15 ch.neut=3.0e-15 ce.pos=3e-14 ch.neg=3e-14;
dbond[1] n=1.0e23 e.neut=-0.65;
dbond[2] n=3e20 e.neut=-0.70;
dbond[3] n=1.0e24 e.neut=-1.25;

C GENERAL SETTINGS;
```

```
settings newton gummel.starts=2 max.step.reduc=0;
settings damp=6 max.iter=50;
model amorphous;
```

```
C CALCULATING GENERATION PROFILE;
opticgen spectrum=am15_350-1200.in gp3;
print opticgen file=opticgen.dat;
print absorption file=absorption.dat;
print absorptance file=absorptance.dat;
```

```
C CALCULATING SPECTRAL RESPONSE;
settings sr.flux=1.0e20;
solve equil;
solve sr wl.start=300nm wl.step=5nm wl.end=1200nm illum;
print sr file=qe_sr.dat;
```

```
C CALCULATING ILLUMINATED J-V (AM1.5 simulation);
solve equil;
solve v.start=0 v.end=0.7 n.step=50 illum;
print jv file=jv_illum.dat;
print solpar file=solpar.dat;
```

B

ASA web automation code: autASA.py

```
1  #!/usr/bin/python3
2  # author: Erik Spaans, 11/12/2019
3
4  from selenium import webdriver
5  import time
6  import os
7  import subprocess
8  import sys
9  import glob
10 import shutil
11
12 # -----Initializing the driver-----
13 def_down_dir = "/home/autASA/zipped_files/"
14 chromeOptions = webdriver.ChromeOptions()
15 prefs = {"download.default_directory": def_down_dir}
16 chromeOptions.add_experimental_option("prefs", prefs)
17 driver = webdriver.Chrome(chrome_options=chromeOptions)
18 # driver.minimize_window()
19 driver.implicitly_wait(5)
20 driver.get("https://asa.ewi.tudelft.nl/login")
21 # -----
22
23 # -----Input definitions-----
24 input_email = "input-26"
25 input_ps = "input-31"
26 input_job_des = "input-160"
27 input_cas = "input-168"
28 input_in = "input-175"
29 wait_time = .5
30 directory_new = "/home/autASA/"
31 login_email = 'netid@student.tudelft.nl'
32 login_ps = '1234'
33 # -----
34
35
36 def newJob(directory, skip_files=[]):
37     # click on 'new job'
38     driver.find_element_by_partial_link_text('New job').click()
39     # list with descriptions
```

```

40 descriptions = []
41 # upload jobs
42 for cas_file in os.listdir(directory+"cas/"):
43     if not cas_file.startswith('.') and cas_file[-4] not in
44         ↪ skip_files:
45         # job description
46         print(cas_file)
47         descriptions.append(cas_file[:-4])
48         driver.find_element_by_id(input_job_des).send_keys(cas_file
49             ↪[:-4])
50         time.sleep(wait_time)
51         # .cas file
52         driver.find_element_by_id(input_cas).send_keys(
53             directory+"cas/"+cas_file)
54         time.sleep(wait_time)
55         # .in files
56         for in_file in os.listdir(directory+"in/"):
57             if not in_file.startswith('.'):
58                 driver.find_element_by_id(input_in).send_keys(
59                     directory+"in/"+in_file)
60                 driver.find_elements_by_xpath(
61                     "/html/body/div/div[1]/div/div/div/main/div/div[3]/div/
62                     ↪div/div/form/div[2]/div[2]/button/span")[0].click
63                     ↪()
64                 time.sleep(1.5)
65 print("All files have been uploaded")
66 return descriptions
67
68 def delete_all():
69     # click on 'completed jobs'
70     driver.find_element_by_partial_link_text('Completed jobs').click()
71     # get table
72     table = driver.find_elements_by_xpath(
73         "//*[@id='app']/div/main/div/div[6]/div/div/div/div/div/table")
74     ↪ [0]
75     # delete all files
76     while True:
77         if table.find_elements_by_xpath("//*[@id='app']/div/main/div/
78             ↪div[6]/div/div/div/div/div/table/tbody/tr/td")[0].text ==
79             ↪ "No data available":
80             break
81         del_symb = table.find_elements_by_xpath(
82             "/html/body/div/div/div/div/div/main/div/div[6]/div[1]/div/
83             ↪div/div/div/table/tbody/tr[1]/td[9]/button[3]") [0]
84         webdriver.ActionChains(driver).move_to_element(
85             del_symb).click(del_symb).perform()
86         confirm = table.find_elements_by_xpath(
87             "/html/body/div/div[3]/div/div/div[2]/div[2]/button")[0]
88         webdriver.ActionChains(driver).move_to_element(
89             confirm).click(confirm).perform()
90         time.sleep(wait_time)
91     print("All files have been deleted from ASA web")
92
93 def download_delete_all(num_files):

```

```

88 # click on 'completed jobs'
89 driver.find_element_by_partial_link_text('Completed jobs').click()
90 # get table
91 table = driver.find_elements_by_xpath(
92     "//*[@id='app']/div/main/div/div[6]/div/div/div/div/div/table")
93     ↪ [0]
94 # download and delete all files
95 counter = 0
96 while True:
97     if table.find_elements_by_xpath("//*[ @id='app']/div/main/div/
98     ↪ div[6]/div/div/div/div/div/div/table/tbody/tr/td") [0].text ==
99     ↪ "No data available":
100         if counter == num_files or num_files == 'all':
101             break
102         else:
103             # download
104             down_sym = table.find_elements_by_xpath(
105                 "/html/body/div/div/div/div/div/main/div/div[6]/div[1]/
106                 ↪ div/div/div/div/table/tbody/tr/td[9]/button[1]")
107                 ↪ [0]
108             webdriver.ActionChains(driver).move_to_element(
109                 down_sym).click(down_sym).perform()
110             # delete
111             del_symb = table.find_elements_by_xpath(
112                 "/html/body/div/div/div/div/div/main/div/div[6]/div[1]/
113                 ↪ div/div/div/div/table/tbody/tr/td[9]/button[3]")
114                 ↪ [0]
115             webdriver.ActionChains(driver).move_to_element(
116                 del_symb).click(del_symb).perform()
117             # confirm delete
118             confirm = table.find_elements_by_xpath(
119                 "/html/body/div/div[3]/div/div/div[2]/div[2]/button")
120                 ↪ [0]
121             webdriver.ActionChains(driver).move_to_element(
122                 confirm).click(confirm).perform()
123             counter += 1
124             time.sleep(wait_time)
125 print("All files have been downloaded and deleted")
126
127 def checkCompleted(descriptions):
128     # click on 'completed jobs'
129     driver.find_element_by_partial_link_text('Completed jobs').click()
130     # get table
131     table = driver.find_elements_by_xpath(
132         "//*[@id='app']/div/main/div/div[6]/div/div/div/div/div/table")
133         ↪ [0]
134     # download all files
135     while True:
136         completed_files = []
137         num_rows = get_row_count(table)
138         for num in range(1, num_rows+1):
139             completed_files.append(table.find_elements_by_xpath(
140                 "//*[ @id='app']/div/main/div/div[6]/div/div/div/div/div
141                 ↪ /table/tbody/tr["+str(num)+"]/td[1]") [0].text)
142         time.sleep(1)

```

```
134         if all(job in completed_files for job in descriptions):
135             break
136
137
138 def get_row_count(table):
139     return len(table.find_elements_by_tag_name("tr"))-1
140
141
142 def get_column_count(table):
143     return len(table.find_elements_by_xpath("//tr[2]/td"))
144
145
146 def validate_bool(question):
147     while True:
148         output = input(question)
149         if output == 'q':
150             sys.exit()
151         try:
152             output = int(output)
153             if output == 0 or output == 1:
154                 return bool(output)
155             else:
156                 print("Please enter a valid bool integer.")
157         except Exception:
158             print("Please enter a valid bool integer.")
159
160
161 def plot():
162     plot = validate_bool("Plot? (1 or 0): ")
163     if plot:
164         key = input("Keyword: ")
165         os.system(
166             "python3 /home/autASA/readSimData.py /home/autASA/
167             ↪ unzipped_files/ "+key)
168     else:
169         pass
170
171 def unzip_all():
172     subprocess.call(
173         "/home/autASA/unzip.sh")
174
175
176 def main():
177     # Login
178     driver.find_element_by_id(input_email).send_keys(login_email)
179     driver.find_element_by_id(input_ps).send_keys(login_ps)
180     driver.find_elements_by_xpath(
181         "//*[@id='app']/div/main/div/div/div/div/div/div/form/div[3]/div
182         ↪ [2]/button")[0].click()
183
184     if 'clean' in sys.argv[1:]:
185         for f in glob.glob("/home/autASA/zipped_files/*"):
186             os.remove(f)
187         for d in glob.glob("/home/autASA/unzipped_files/*"):
188             shutil.rmtree(d)
```

```
188     try:
189         os.remove(
190             "/home/autASA/unzip_names.txt")
191     except:
192         pass
193
194     if 'new' in sys.argv[1:]:
195         skip_files = os.listdir(directory_new+"unzipped_files/")
196     else:
197         skip_files = []
198
199     if 'open' in sys.argv[1:]:
200         pass
201     elif 'downall' in sys.argv[1:]:
202         download_delete_all('all')
203         # unzip all downloaded files
204         unzip_all()
205         # close window
206         driver.quit()
207         driver.stop_client()
208         plot()
209     else:
210         # delete existing jobs
211         delete_all()
212         time.sleep(wait_time)
213         # new job
214         descriptions = newJob(directory_new, skip_files)
215         if 'many' in sys.argv[1:]:
216             # download and delete all jobs when many files are uploaded
217             download_delete_all(len(descriptions))
218         else:
219             # check if all simulations are completed
220             checkCompleted(descriptions)
221             # download and delete all
222             download_delete_all('all')
223             # unzip all downloaded files
224             unzip_all()
225             # close window
226             driver.quit()
227             driver.stop_client()
228             # run the plotting script
229             plot()
230
231
232 if __name__ == "__main__":
233     main()
```




ASA parameter sensitivity

Table C.1: Numerical results of the sensitivity of the open-circuit voltage V_{oc} , short-circuit current density J_{sc} , fill factor FF , efficiency η , EQE for the range 300 nm to 550 nm (labelled as EQE₁) and for 550 nm to 800 nm (labelled as EQE₂) to the variation of model parameters in ASA simulations. The abbreviations are described in Nomenclature.

Parameter	Variation range	Unit	Relative difference Δ					
			V_{oc}	J_{sc}	FF	η	EQE ₁	EQE ₂
Layer thickness		nm						
Front TCO	[500-900]		-0.2	-2.9	0.1	-3.0	-6.0	-3.3
Front AZO	[0-5]		0.0	-0.1	0.0	-0.1	0.0	-0.4
	[5-50]		-0.1	-1.0	0.1	-1.1	-2.5	-2.6
a-Si:H(p)	[5-25]		-0.5	-8.2	-9.5	-17.4	-24.8	-2.3
a-Si:H(i)	[150-450]		-4.8	11.6	-15.3	-10.1	-5.3	25.1
a-Si:H(n)	[5-25]		-0.1	-2.0	0.2	-1.9	-0.2	-3.2
Back AZO	[0-5]		0.3	7.0	-0.8	6.5	0.2	13.1
	[5-100]		0.0	-0.8	0.1	-0.7	0.0	-1.5
Back reflector	[100-500]		0.0	0.0	0.0	0.0	0.0	0.0
Band gap		eV						
a-Si:H(p)	[1.8-2.0]		9.3	3.0	1.2	14.0	7.5	1.2
	[2.0-2.2]		0.8	1.2	-19.3	-17.6	5.3	-0.7
a-Si:H(i)	[1.6-1.9]		27.5	-3.5	5.3	29.6	-7.5	-2.3
a-Si:H(n)	[1.6-1.9]		0.1	1.3	0.5	1.9	0.1	2.2
Mobility		$m^2V^{-1}s^{-1}$						
Electron								
a-Si:H(p)	$[1 \cdot 10^{-4} - 1 \cdot 10^{-2}]$		-1.0	0.9	0.2	0.0	5.3	1.0
a-Si:H(i)	$[1 \cdot 10^{-4} - 2 \cdot 10^{-3}]$		0.6	14.9	16.9	35.2	31.1	7.4
	$[2 \cdot 10^{-3} - 1 \cdot 10^{-2}]$		0.0	1.8	1.5	3.2	3.9	0.8
a-Si:H(n)	$[1 \cdot 10^{-4} - 1 \cdot 10^{-2}]$		0.0	0.0	0.0	0.0	0.0	0.0
Hole								
a-Si:H(p)	$[1 \cdot 10^{-5} - 1 \cdot 10^{-4}]$		0.5	-0.1	38.2	38.7	-3.0	1.7
	$[1 \cdot 10^{-4} - 1 \cdot 10^{-3}]$		0.0	-0.1	4.9	4.7	-1.0	0.0
a-Si:H(i)	$[1 \cdot 10^{-5} - 1 \cdot 10^{-3}]$		-2.2	17.3	30.9	50.1	4.4	34.7

Table C.1: Numerical results of the sensitivity of the open-circuit voltage V_{oc} , short-circuit current density J_{sc} , fill factor FF , efficiency η , EQE for the range 300 nm to 550 nm (labelled as EQE₁) and for 550 nm to 800 nm (labelled as EQE₂) to the variation of model parameters in ASA simulations. The abbreviations are described in Nomenclature.

Parameter	Variation range	Unit	Relative difference Δ					
			V_{oc}	J_{sc}	FF	η	EQE ₁	EQE ₂
a-Si:H(n)	$[1 \cdot 10^{-5} - 1 \cdot 10^{-3}]$		-0.1	-0.3	-0.3	-0.7	0.0	-0.6
Activation energy		eV						
a-Si:H(p)	[0.1-0.45]		-0.4	-0.8	-1.6	-2.6	-1.8	-0.3
	[0.45-0.6]		-5.3	-1.9	-39.9	-44.1	0.5	-3.3
a-Si:H(n)	[0.1-0.3]		-0.8	-0.3	-1.5	-2.6	-0.4	-0.4
	[0.3-0.6]		-5.2	-1.4	-19.6	-24.8	-2.1	-1.6
DOS ext.		m^{-3}						
N_C								
a-Si:H(p)	$[1 \cdot 10^{25} - 1 \cdot 10^{28}]$		-2.0	-5.4	-0.1	-7.5	-14.4	-1.4
a-Si:H(i)	$[1 \cdot 10^{25} - 1 \cdot 10^{28}]$		-16.2	6.9	-2.0	-12.2	22.4	1.2
a-Si:H(n)	$[1 \cdot 10^{25} - 1 \cdot 10^{28}]$		0.0	0.0	0.0	0.1	0.0	0.0
N_V								
a-Si:H(p)	$[5 \cdot 10^{25} - 5 \cdot 10^{26}]$		0.3	-0.1	42.1	42.3	-3.3	2.0
	$[5 \cdot 10^{26} - 1 \cdot 10^{28}]$		0.0	-0.1	6.4	6.1	-1.3	0.0
a-Si:H(i)	$[1 \cdot 10^{25} - 1 \cdot 10^{28}]$		-15.3	1.9	5.8	-8.7	-1.1	6.5
a-Si:H(n)	$[1 \cdot 10^{25} - 1 \cdot 10^{28}]$		-0.1	-1.0	-0.5	-1.7	-0.1	-1.9
DOS loc.								
CB tail								
e.char		eV						
a-Si:H(p)	[0.01-0.1]		0.0	0.0	0.0	0.0	0.0	0.0
a-Si:H(i)	[0.01-0.06]		-2.3	0.2	-0.3	-2.4	-0.8	0.9
	[0.06-0.1]		-2.1	-13.9	-7.3	-22.0	-27.5	-11.3
a-Si:H(n)	[0.01-0.1]		0.1	0.0	0.3	0.4	0.1	0.0
n.emob		$m^{-3} eV^{-1}$						
a-Si:H(p)	$[1 \cdot 10^{26} - 1 \cdot 10^{29}]$		0.0	0.0	0.0	0.0	0.0	0.0
a-Si:H(i)	$[1 \cdot 10^{26} - 1 \cdot 10^{29}]$		-1.1	0.1	0.4	-0.7	-0.1	0.3
a-Si:H(n)	$[1 \cdot 10^{26} - 1 \cdot 10^{29}]$		0.1	0.0	0.3	0.4	0.1	0.0
c.neut (all)	$[1 \cdot 10^{-16} - 1 \cdot 10^{-13}]$	$m^{-3} s^{-1}$	0.0	0.0	0.0	0.0	0.0	0.0
c.neg (all)	$[1 \cdot 10^{-16} - 1 \cdot 10^{-13}]$	$m^{-3} s^{-1}$	0.0	0.0	0.0	-0.1	0.0	0.0
e.range (all)	[0.1-1]	eV	0.0	0.0	0.3	0.4	0.1	0.0
VB tail								
e.char		eV						
a-Si:H(p)	[0.01-0.1]		0.4	0.1	2.1	2.6	-0.3	0.0
a-Si:H(i)	[0.01-0.05]		0.3	2.1	-4.7	-2.3	7.3	-0.2
	[0.05-0.1]		-0.4	-37.4	-6.2	-41.5	-7.6	-60.5
a-Si:H(n)	[0.01-0.1]		0.0	0.0	0.0	0.0	0.0	0.0
n.emob		$m^{-3} eV^{-1}$						
a-Si:H(p)	$[1 \cdot 10^{26} - 1 \cdot 10^{29}]$		0.6	0.0	2.7	3.2	-0.5	0.0
a-Si:H(i)	$[1 \cdot 10^{26} - 1 \cdot 10^{27}]$		-0.3	0.9	0.8	1.3	2.5	0.3

Table C.1: Numerical results of the sensitivity of the open-circuit voltage V_{oc} , short-circuit current density J_{sc} , fill factor FF , efficiency η , EQE for the range 300 nm to 550 nm (labelled as EQE₁) and for 550 nm to 800 nm (labelled as EQE₂) to the variation of model parameters in ASA simulations. The abbreviations are described in Nomenclature.

Parameter	Variation range	Unit	Relative difference Δ					
			V_{oc}	J_{sc}	FF	η	EQE ₁	EQE ₂
a-Si:H(n)	$[1 \cdot 10^{27} - 1 \cdot 10^{29}]$		2.1	-3.9	-16.1	-17.8	5.5	-17.3
	$[1 \cdot 10^{26} - 1 \cdot 10^{29}]$		0.0	0.0	0.0	-0.1	0.0	0.0
c.neut (all)	$[1 \cdot 10^{-16} - 1 \cdot 10^{-13}]$	$m^{-3} s^{-1}$	0.6	0.0	-0.9	-0.4	0.0	-0.1
c.pos (all)	$[1 \cdot 10^{-16} - 1 \cdot 10^{-13}]$	$m^{-3} s^{-1}$	-2.4	-0.9	0.3	-3.1	-2.4	-0.5
e.range (all)	[0.1-1]	eV	-0.2	1.8	-1.5	0.1	5.4	0.3
Dangling bonds								
n		m^{-3}						
a-Si:H(p)	$[1 \cdot 10^{21} - 1 \cdot 10^{24}]$		-0.1	-0.7	0.0	-0.9	-2.5	-0.2
	$[1 \cdot 10^{24} - 1 \cdot 10^{26}]$		-0.9	-4.8	0.1	-5.5	-14.7	-1.6
a-Si:H(i)	$[1 \cdot 10^{18} - 1 \cdot 10^{21}]$		-2.5	-0.3	-7.1	-9.7	-0.3	-0.5
	$[1 \cdot 10^{21} - 1 \cdot 10^{22}]$		-10.6	-3.3	-13.5	-25.2	-2.7	-3.8
a-Si:H(n)	$[1 \cdot 10^{22} - 1 \cdot 10^{23}]$		-14.9	-23.5	-33.0	-56.3	-21.1	-27.1
	$[1 \cdot 10^{21} - 1 \cdot 10^{26}]$		-0.1	-1.3	-0.3	-1.7	-0.1	-2.2
ce.neut (all)	$[1 \cdot 10^{-16} - 1 \cdot 10^{-13}]$	$m^{-3} s^{-1}$	-6.3	-1.1	-6.0	-12.8	-1.0	-1.3
ce.pos (all)	$[1 \cdot 10^{-16} - 1 \cdot 10^{-13}]$	$m^{-3} s^{-1}$	-5.2	-1.6	-1.8	-8.4	-4.3	-0.9
ch.neut (all)	$[1 \cdot 10^{-16} - 1 \cdot 10^{-13}]$	$m^{-3} s^{-1}$	-6.3	-1.1	-6.0	-12.8	-1.0	-1.3
ch.neg (all)	$[1 \cdot 10^{-16} - 1 \cdot 10^{-13}]$	$m^{-3} s^{-1}$	-7.7	-1.5	-8.2	-16.5	-0.5	-2.3

D

Simulations: complex refractive indices

D.1. a-Si:H cell

The refractive index n and the absorption index κ of the materials used in the simulation of the a-Si:H cell, depicted in Figure 4.9, are plotted in Figure D.1.

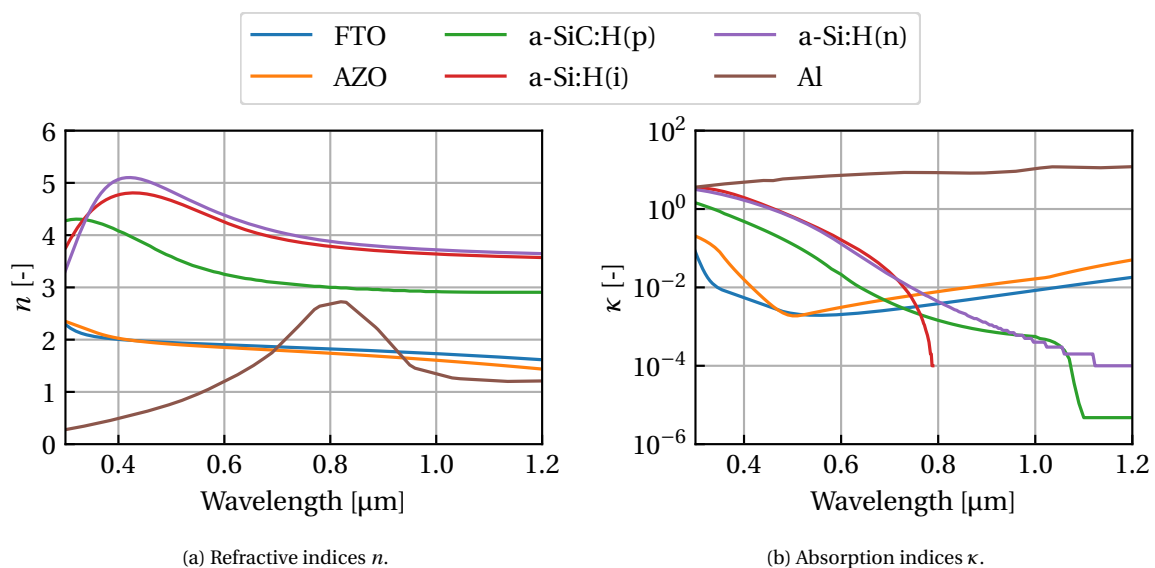


Figure D.1: Complex refractive indices of the materials used in the simulations of a-Si:H.

D.2. $\mu\text{c-Si:H}$ cell

The complex refractive indices of the materials used in the simulation of the $\mu\text{c-Si:H}$ cell, shown in Figure 4.17, are plotted in Figure D.2.

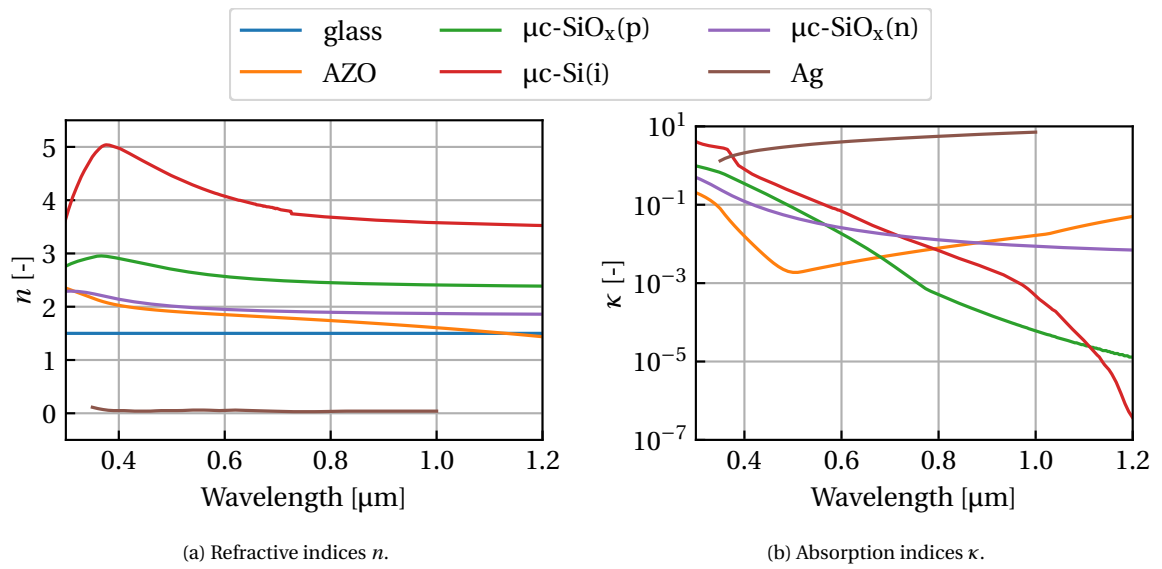


Figure D.2: Complex refractive indices of the materials used in the simulations of $\mu\text{c-Si:H}$. The absorption index of glass is 0 over the full spectrum.

E

EQE artefacts

The computation of the subcell's EQE in a micromorph device proved to be a complicated task from a modelling perspective. In this appendix, some of the experienced complications are shown.

If the photon flux of the bias light is chosen too low, the computation of the EQE fails to give the right results for low wavelengths. This is shown in Figure E.1 for the EQE of the top subcell.

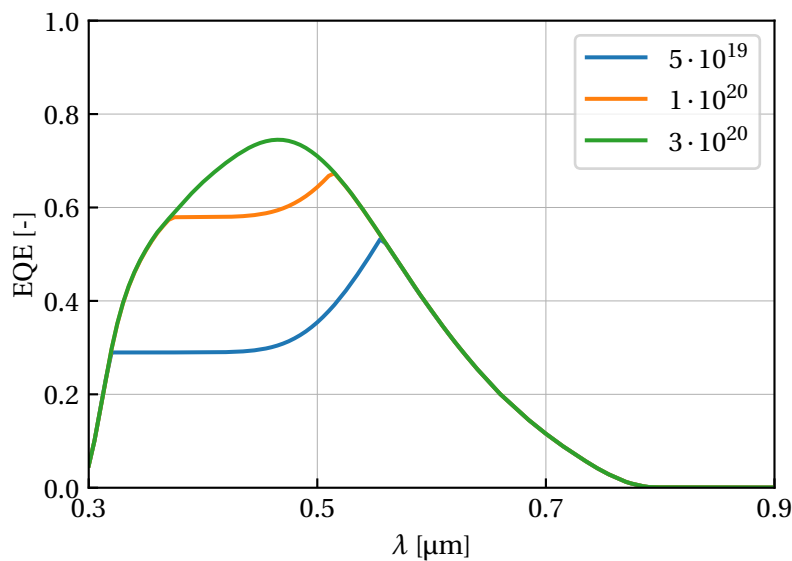


Figure E.1: Simulated EQE of the a-Si:H cell in a micromorph device, measured with different fluxes of the 800 nm bias light. The legend indicates the photon flux density in units of $\text{m}^{-2} \text{s}^{-1}$.

Besides this artefact, the computation of the EQE was seen to completely fail for specific photon fluxes. An example is shown in Figure E.2, where decreasing the flux from $3 \cdot 10^{20} \text{ m}^{-2} \text{ s}^{-1}$ to $2 \cdot 10^{20} \text{ m}^{-2} \text{ s}^{-1}$ resulted in an erroneous EQE.

These failures support the use of the adapted approach for computing the subcell's EQE shown in Section 5.1.3, where only the targeted subcell was modelled electrically.

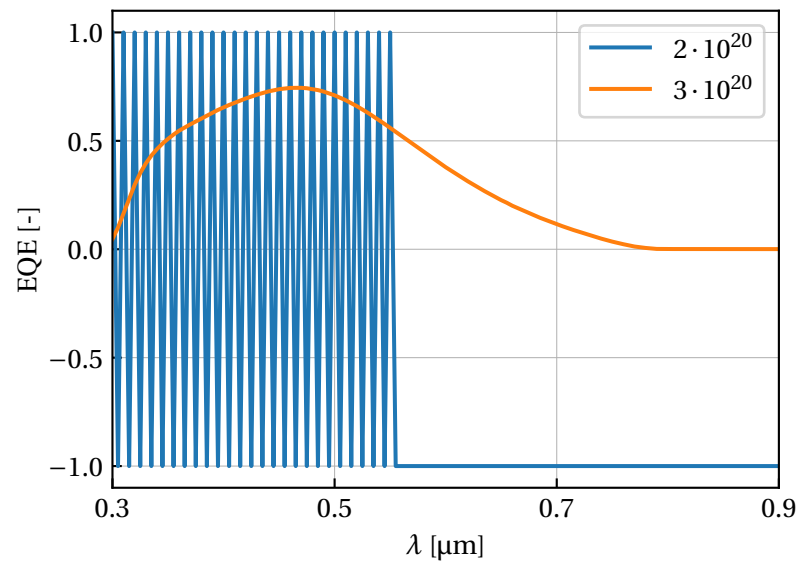


Figure E.2: Failure of a simulated EQE of the a-Si:H cell in a micromorph device, measured with different fluxes of the 800 nm bias light. The legend indicates the photon flux density in units of $\text{m}^{-2} \text{s}^{-1}$.

F

Texture comparison: micromorph cell performance parameters

In Section 5.3.1, the micromorph efficiency was presented for the baseline texturing from HyET Solar and the MST developed within FlamingoPV. Here, the rest of the performance indicators, J_{sc} , V_{oc} and FF , are presented.

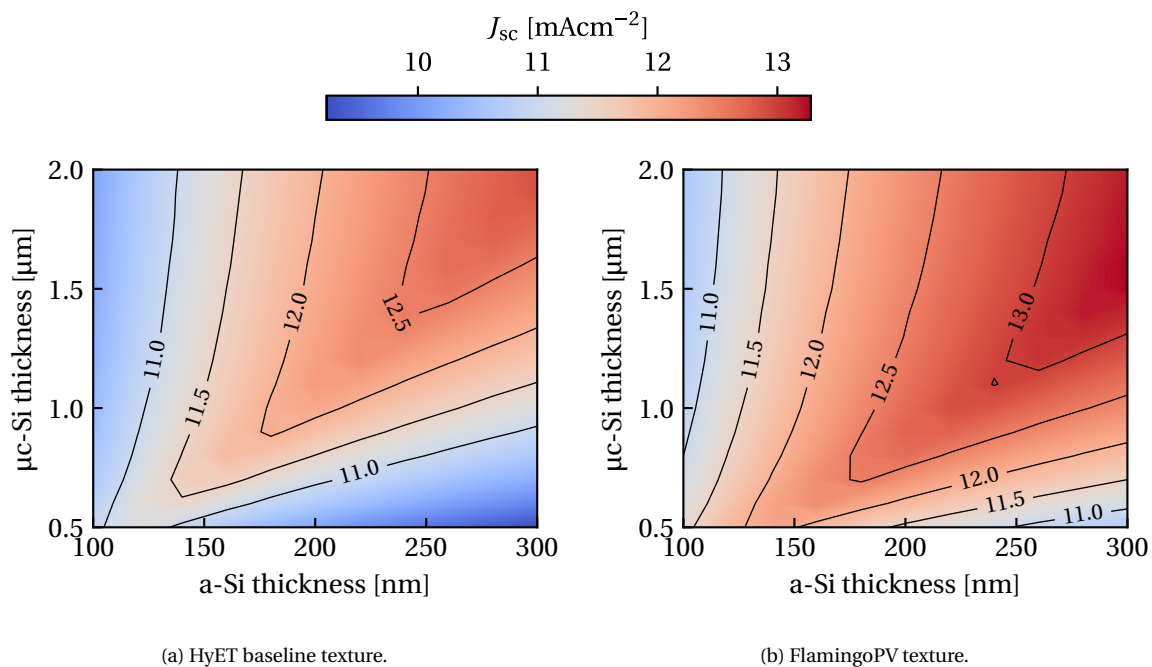


Figure F.1: Comparison of the short-circuit currents as a function of the subcell thicknesses for the baseline texturing at HyET and the developed texture for FlamingoPV.

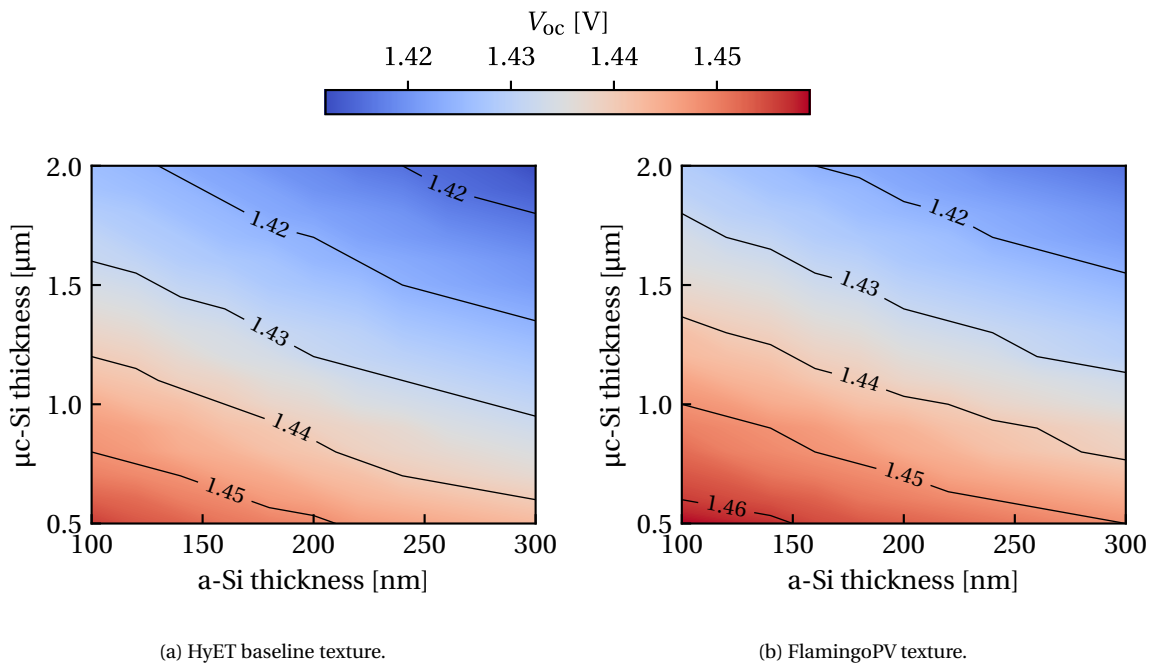


Figure F2: Comparison of the open-circuit voltages as a function of the subcell thicknesses for the baseline texturing at HyET and the developed texture for FlamingoPV.

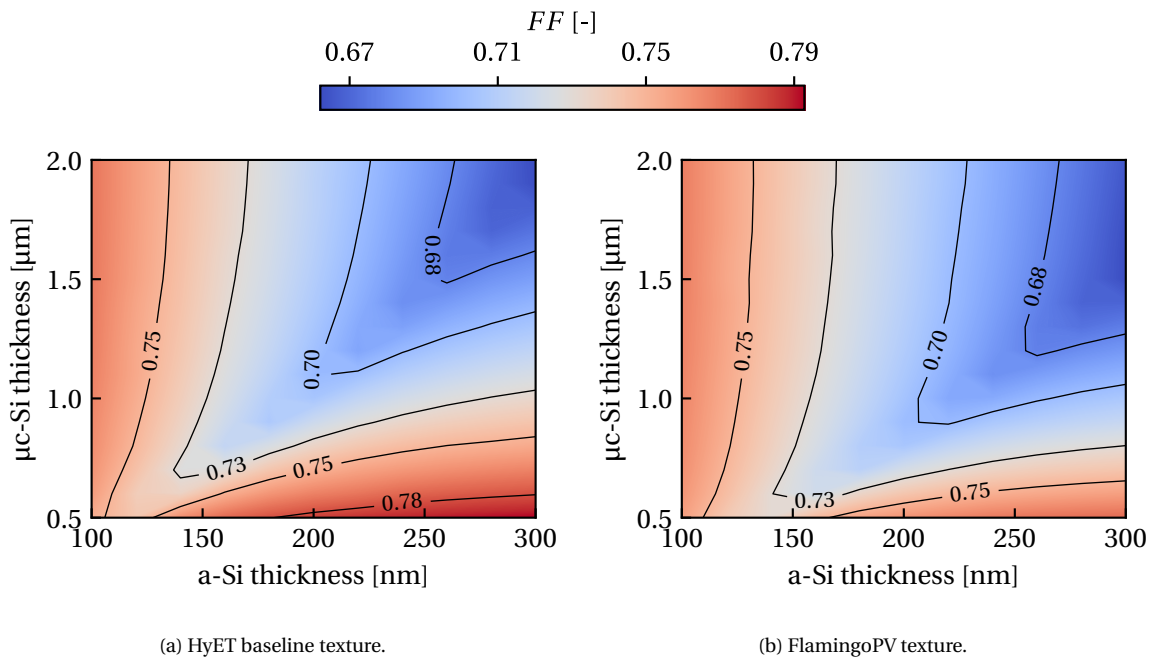


Figure E3: Comparison of the fill factors as a function of the subcell thicknesses for the baseline texturing at HyET and the developed texture for FlamingoPV.

Bibliography

- [1] Rebecca Lindsey. *Climate Change: Atmospheric Carbon Dioxide*. Feb. 20, 2020. URL: <https://www.climate.gov/news-features/understanding-climate/climate-change-atmospheric-carbon-dioxide>. Accessed 19/05/2020.
- [2] LuAnn Dahlman. *Climate Change: Annual greenhouse gas index*. Sept. 26, 2020. URL: <https://www.climate.gov/news-features/understanding-climate/climate-change-annual-greenhouse-gas-index>. Accessed 19/05/2020.
- [3] Nerilie J Abram et al. “Early onset of industrial-era warming across the oceans and continents”. In: *Nature* 536.7617 (2016), pp. 411–418.
- [4] IPCC. “Summary for Policymakers”. In: *Global Warming of 1.5°C. An IPCC Special Report on the impacts of global warming of 1.5°C above pre-industrial levels and related global greenhouse gas emission pathways, in the context of strengthening the global response to the threat of climate change, sustainable development, and efforts to eradicate poverty*. Ed. by P. Zhai H.-O. Pörtner D. Roberts J. Skea P.R. Shukla A. Pirani W. Moufouma-Okia C. Péan R. Pidcock S. Connors J.B.R. Matthews Y. Chen X. Zhou M.I. Gomis E. Lonnoy T. Maycock M. Tignor Masson-Delmotte V. and T. Waterfield. Geneva, Switzerland: World Meteorological Organization, 2018. URL: <https://www.ipcc.ch/sr15/chapter/spm/>.
- [5] United Nations. *Paris Agreement*. 2015. URL: <https://unfccc.int/process-and-meetings/the-paris-agreement/the-paris-agreement>.
- [6] BP. *Statistical Review of World Energy*. 2019. URL: <https://www.bp.com/en/global/corporate/energy-economics/statistical-review-of-world-energy.html>.
- [7] IRENA. *Renewable Power Generation Costs in 2018*. 2019. URL: <https://www.irena.org/publications/2019/May/Renewable-power-generation-costs-in-2018>.
- [8] A. Smets et al. *Solar Energy: The Physics and Engineering of Photovoltaic Conversion, Technologies and Systems*. UIT Cambridge Ltd, 2016. ISBN: 9781906860325.
- [9] F. Meillaud et al. “Recent advances and remaining challenges in thin-film silicon photovoltaic technology”. In: *Materials Today* 18.7 (2015), pp. 378–384. ISSN: 1369-7021. DOI: <https://doi.org/10.1016/j.mattod.2015.03.002>.
- [10] IRENA. *The Power to Change: Solar and Wind Cost Reduction Potential to 2025*. 2016. URL: <https://www.irena.org/publications/2016/Jun/The-Power-to-Change-Solar-and-Wind-Cost-Reduction-Potential-to-2025>.
- [11] A. V. Shah et al. “Thin-film silicon solar cell technology”. In: *Progress in Photovoltaics: Research and Applications* 12.2-3 (2004), pp. 113–142. DOI: 10.1002/pip.533.
- [12] HyET Group. *HyET Solar: flexible light weight solar modules*. URL: <https://www.hyetsolar.com> (visited on 04/05/2020).

- [13] *Flexible Lightweight Advanced Materials In Next Generation Of PV: FlamingoPV*. Project description. Delft University of Technology and HyET Solar. August, 2018.
- [14] A. Reinders et al. *Photovoltaic Solar Energy: From Fundamentals to Applications*. Wiley, 2017. ISBN: 9781118927465.
- [15] D.A. Neamen. *Semiconductor Physics and Devices: Basic Principles*. McGraw-Hill international edition. McGraw-Hill, 2012. ISBN: 9780071089029.
- [16] E. Boeker and R. van Grondelle. *Environmental Physics: Sustainable Energy and Climate Change*. Wiley, 2011. ISBN: 9781119975199.
- [17] American Society for Testing, Materials. Committee G03 on Weathering, and Durability. *Standard tables for reference solar spectral irradiances: direct normal and hemispherical on 37° tilted surface*. ASTM international, 2003.
- [18] C.B.Honsberg and S.G.Bowden. *Absorption Coefficient*. URL: <https://www.pveducation.org/pvcdrom/pn-junctions/absorption-coefficient> (visited on 10/02/2020).
- [19] Peter C.Y. Chang, J.G. Walker, and K.I. Hopcraft. "Ray tracing in absorbing media". In: *Journal of Quantitative Spectroscopy and Radiative Transfer* 96.3 (2005), pp. 327–341. ISSN: 0022-4073. DOI: <https://doi.org/10.1016/j.jqsrt.2005.01.001>.
- [20] Pietro Altermatt. *Fresnel equations in absorptive incoming media*. URL: <https://www.pvlighthouse.com.au/cms/lectures/altermatt/optics/fresnel-equations-in-absorptive-incoming-media> (visited on 10/02/2020).
- [21] S.H. Simon. *The Oxford Solid State Basics*. Oxford University Press, 2013. ISBN: 9780191502101.
- [22] Khuram Ali, Sohail A Khan, and MZ Mat Jafri. "Effect of double layer (SiO₂/TiO₂) anti-reflective coating on silicon solar cells". In: *Int. J. Electrochem. Sci* 9.12 (2014), pp. 7865–7874.
- [23] Mei-Ling Kuo et al. "Realization of a near-perfect antireflection coating for silicon solar energy utilization". In: *Opt. Lett.* 33.21 (Nov. 2008), pp. 2527–2529. DOI: 10.1364/OL.33.002527.
- [24] J. A. Willemen. "Modelling of Amorphous Silicon Single- and Multi-Junction Solar Cells". PhD thesis. Delft: Delft University of Technology, Oct. 1998.
- [25] M. Fortes et al. "Impact of series and shunt resistances in amorphous silicon thin film solar cells". In: *Solar Energy* 100 (2014), pp. 114–123. ISSN: 0038-092X. DOI: <https://doi.org/10.1016/j.solener.2013.11.022>.
- [26] S. Kasap and P. Capper. *Springer Handbook of Electronic and Photonic Materials*. Springer Handbooks. Springer International Publishing, 2017. ISBN: 9783319489339.
- [27] K. L. Chopra, P. D. Paulson, and V. Dutta. "Thin-film solar cells: an overview". In: *Progress in Photovoltaics: Research and Applications* 12.2-3 (2004), pp. 69–92. DOI: 10.1002/pip.541.
- [28] R. C. Chittick, J. H. Alexander, and H. F. Sterling. "The Preparation and Properties of Amorphous Silicon". In: *Journal of The Electrochemical Society* 116.1 (1969), p. 77. DOI: 10.1149/1.2411779.
- [29] W.E. Spear and P.G. Le Comber. "Substitutional doping of amorphous silicon". In: *Solid State Communications* 17.9 (1975), pp. 1193–1196. ISSN: 0038-1098. DOI: [https://doi.org/10.1016/0038-1098\(75\)90284-7](https://doi.org/10.1016/0038-1098(75)90284-7).

- [30] D. E. Carlson and C. R. Wronski. “Amorphous silicon solar cell”. In: *Applied Physics Letters* 28.11 (1976), pp. 671–673. DOI: 10.1063/1.88617.
- [31] Martin A. Green et al. “Solar cell efficiency tables (Version 55)”. In: *Progress in Photovoltaics: Research and Applications* 28.1 (2020), pp. 3–15. DOI: 10.1002/pip.3228.
- [32] Takuya Matsui et al. “High-efficiency amorphous silicon solar cells: Impact of deposition rate on metastability”. In: *Applied Physics Letters* 106.5 (2015), p. 053901. DOI: 10.1063/1.4907001.
- [33] Arvind Shah. “Thin-Film Silicon Solar Cells”. In: *Practical Handbook of Photovoltaics (Second Edition)*. Second Edition. Boston: Academic Press, 2012, pp. 209–281. ISBN: 978-0-12-385934-1. DOI: <https://doi.org/10.1016/B978-0-12-385934-1.00008-8>.
- [34] A. Shah. *Thin-Film Silicon Solar Cells*. Engineering sciences. EPFL Press, 2010. ISBN: 9781420066746.
- [35] N Mott. “The mobility edge since 1967”. In: *Journal of Physics C: Solid State Physics* 20.21 (July 1987), pp. 3075–3102. DOI: 10.1088/0022-3719/20/21/008.
- [36] D. L. Staebler and C. R. Wronski. “Reversible conductivity changes in discharge-produced amorphous Si”. In: *Applied Physics Letters* 31.4 (1977), pp. 292–294. DOI: 10.1063/1.89674.
- [37] Hellmut Fritzsche. “Development in Understanding and Controlling the Staebler-Wronski Effect in a-Si:H”. In: *Annual Review of Materials Research* 31.1 (2001), pp. 47–79. DOI: 10.1146/annurev.matsci.31.1.47.
- [38] R. Platz et al. “Influence of excitation frequency, temperature, and hydrogen dilution on the stability of plasma enhanced chemical vapor deposited a-Si:H”. In: *Journal of Applied Physics* 84.7 (1998), pp. 3949–3953. DOI: 10.1063/1.368592.
- [39] M. Zeman et al. “Computer modelling of current matching in a-Si:H/a-Si:H tandem solar cells on textured TCO substrates”. In: *Solar Energy Materials and Solar Cells* 46.2 (1997), pp. 81–99. ISSN: 0927-0248. DOI: [https://doi.org/10.1016/S0927-0248\(96\)00094-3](https://doi.org/10.1016/S0927-0248(96)00094-3).
- [40] S. Vepřek and V. Mareček. “The preparation of thin layers of Ge and Si by chemical hydrogen plasma transport”. In: *Solid-State Electronics* 11.7 (1968), pp. 683–684. ISSN: 0038-1101. DOI: [https://doi.org/10.1016/0038-1101\(68\)90071-3](https://doi.org/10.1016/0038-1101(68)90071-3).
- [41] A. Wang and G. Lucovsky. “Intrinsic microcrystalline silicon deposited by remote PECVD: a new thin-film photovoltaic material”. In: *IEEE Conference on Photovoltaic Specialists*. May 1990, 1614–1618 vol.2. DOI: 10.1109/PVSC.1990.111882.
- [42] J. Meier et al. “Complete microcrystalline p-i-n solar cell—Crystalline or amorphous cell behavior?” In: *Applied Physics Letters* 65.7 (1994), pp. 860–862. DOI: 10.1063/1.112183.
- [43] Hitoshi Sai et al. “Thin-film microcrystalline silicon solar cells: 11.9% efficiency and beyond”. In: *Applied Physics Express* 11.2 (Jan. 2018), p. 022301. DOI: 10.7567/apex.11.022301.

- [44] O Vetterl et al. "Intrinsic microcrystalline silicon: A new material for photovoltaics". In: *Solar Energy Materials and Solar Cells* 62.1 (2000), pp. 97–108. ISSN: 0927-0248. DOI: [https://doi.org/10.1016/S0927-0248\(99\)00140-3](https://doi.org/10.1016/S0927-0248(99)00140-3).
- [45] Yoshiyuki Nasuno, Michio Kondo, and Akihisa Matsuda. "Effects of Substrate Surface Morphology on Microcrystalline Silicon Solar Cells". In: *Japanese Journal of Applied Physics* 40.Part 2, No. 4A (Apr. 2001), pp. L303–L305. DOI: [10.1143/jjap.40.L303](https://doi.org/10.1143/jjap.40.L303).
- [46] M. Python et al. "Influence of the substrate geometrical parameters on microcrystalline silicon growth for thin-film solar cells". In: *Solar Energy Materials and Solar Cells* 93.10 (2009), pp. 1714–1720. ISSN: 0927-0248. DOI: <https://doi.org/10.1016/j.solmat.2009.05.025>.
- [47] J.P. Kleider et al. "Electronic and topographic properties of amorphous and microcrystalline silicon thin films". In: *Thin Solid Films* 383.1 (2001), pp. 57–60. ISSN: 0040-6090. DOI: [https://doi.org/10.1016/S0040-6090\(00\)01614-X](https://doi.org/10.1016/S0040-6090(00)01614-X).
- [48] Hairen Tan et al. "Micro-textures for efficient light trapping and improved electrical performance in thin-film nanocrystalline silicon solar cells". In: *Applied Physics Letters* 103.17 (2013), p. 173905. DOI: [10.1063/1.4826639](https://doi.org/10.1063/1.4826639).
- [49] F. Meillaud et al. "Efficiency limits for single-junction and tandem solar cells". In: *Solar Energy Materials and Solar Cells* 90.18 (2006). 14th International Photovoltaic Science and Engineering Conference, pp. 2952–2959. ISSN: 0927-0248. DOI: <https://doi.org/10.1016/j.solmat.2006.06.002>.
- [50] J. Meier et al. "Intrinsic microcrystalline silicon ($\mu\text{-c-Si:H}$)-a promising new thin film solar cell material". In: *Proceedings of 1994 IEEE 1st World Conference on Photovoltaic Energy Conversion - WCPEC (A Joint Conference of PVSC, PVSEC and PSEC)*. Vol. 1. Dec. 1994, 409–412 vol.1. DOI: [10.1109/WCPEC.1994.519985](https://doi.org/10.1109/WCPEC.1994.519985).
- [51] Takuya Matsui et al. "High-efficiency thin-film silicon solar cells realized by integrating stable $\mu\text{-Si:H}$ absorbers into improved device design". In: *Japanese Journal of Applied Physics* 54.8S1 (July 2015), 08KB10. DOI: [10.7567/jjap.54.08kb10](https://doi.org/10.7567/jjap.54.08kb10).
- [52] J Meier et al. "Microcrystalline silicon and the impact on micromorph tandem solar cells". In: *Solar Energy Materials and Solar Cells* 74.1 (2002). PVSEC 12 Part I, pp. 457–467. ISSN: 0927-0248. DOI: [https://doi.org/10.1016/S0927-0248\(02\)00111-3](https://doi.org/10.1016/S0927-0248(02)00111-3).
- [53] F. A. Rubinelli, J. K. Rath, and R. E. I. Schropp. "Microcrystalline n-i-p tunnel junction in $\mu\text{-Si:H}/\mu\text{-Si:H}$ tandem cells". In: *Journal of Applied Physics* 89.7 (2001), pp. 4010–4018. DOI: [10.1063/1.1352032](https://doi.org/10.1063/1.1352032).
- [54] Ping-Kuan Chang et al. "High efficiency $\mu\text{-Si:H}/\mu\text{-Si:H}$ solar cell with a tunnel recombination junction and a n-type $\mu\text{-Si:H}$ layer". In: *Thin Solid Films* 520.9 (2012), pp. 3684–3687. ISSN: 0040-6090. DOI: <https://doi.org/10.1016/j.tsf.2011.12.083>.
- [55] Li Gui-Jun et al. "The study of a new n/p tunnel recombination junction and its application in $\mu\text{-Si:H}/\mu\text{-Si:H}$ tandem solar cells". In: *Chinese Physics B* 18.4 (Mar. 2009), pp. 1674–1678. DOI: [10.1088/1674-1056/18/4/066](https://doi.org/10.1088/1674-1056/18/4/066).
- [56] Wen-Jie Yao et al. "The p recombination layer in tunnel junctions for micromorph tandem solar cells". In: *Chinese Physics B* 20.7 (July 2011), p. 078402. DOI: [10.1088/1674-1056/20/7/078402](https://doi.org/10.1088/1674-1056/20/7/078402).

- [57] D. Fischer et al. "The "micromorph" solar cell: extending a-Si:H technology towards thin film crystalline silicon". In: *Conference Record of the Twenty Fifth IEEE Photovoltaic Specialists Conference - 1996*. May 1996, pp. 1053–1056. DOI: 10.1109/PVSC.1996.564311.
- [58] P. Buehlmann et al. "In situ silicon oxide based intermediate reflector for thin-film silicon micromorph solar cells". In: *Applied Physics Letters* 91.14 (2007), p. 143505. DOI: 10.1063/1.2794423.
- [59] A. Lambertz, T. Grundler, and F. Finger. "Hydrogenated amorphous silicon oxide containing a microcrystalline silicon phase and usage as an intermediate reflector in thin-film silicon solar cells". In: *Journal of Applied Physics* 109.11 (2011), p. 113109. DOI: 10.1063/1.3592208.
- [60] Pere Roca i Cabarrocas. "Deposition Techniques and Processes Involved in the Growth of Amorphous and Microcrystalline Silicon Thin Films". In: *Physics and Technology of Amorphous-Crystalline Heterostructure Silicon Solar Cells*. Ed. by Wilfried G. J. H. M. van Sark, Lars Korte, and Francesco Roca. Berlin, Heidelberg: Springer Berlin Heidelberg, 2012, pp. 131–160. ISBN: 978-3-642-22275-7. DOI: 10.1007/978-3-642-22275-7_5.
- [61] Akihisa Matsuda. "Amorphous and Microcrystalline Silicon". In: *Springer Handbook of Electronic and Photonic Materials*. Ed. by Safa Kasap and Peter Capper. Springer International Publishing, 2017. ISBN: 978-3-319-48933-9. DOI: 10.1007/978-3-319-48933-9_25.
- [62] Klaus Ellmer. "Magnetron sputtering of transparent conductive zinc oxide: relation between the sputtering parameters and the electronic properties". In: *Journal of Physics D: Applied Physics* 33.4 (Feb. 2000), R17–R32. DOI: 10.1088/0022-3727/33/4/201.
- [63] K. Jäger et al. "Large-Area Production of Highly Efficient Flexible Light-Weight Thin-Film Silicon PV Modules". In: *Proceedings of 28th European Photovoltaic Solar Energy Conference and Exhibition*. Oct. 2013, pp. 2164–2169. DOI: 10.4229/28thEUPVSEC2013-3B0.5.5.
- [64] HyET Solar. *PowerFoil 115 datasheet*. URL: https://www.hyetsolar.com/upload_directory/files/HyET-Single-junction.pdf.
- [65] HyET Solar. *PowerFoil 165 datasheet*. URL: https://www.hyetsolar.com/upload_directory/files/HyET-tandem-junction.pdf.
- [66] Sami Iqbal et al. "Highly-efficient low cost anisotropic wet etching of silicon wafers for solar cells application". In: *AIP Advances* 8.2 (2018), p. 025223. DOI: 10.1063/1.5012125.
- [67] Hyeongsik Park et al. "A review of wet chemical etching of glasses in hydrofluoric acid based solution for thin film silicon solar cell application". In: *Current Photovoltaic Research* 5.3 (2017), pp. 75–82.
- [68] D. Rajagopal. Expected completion: July 2020. MSc Thesis. Delft, The Netherlands: Delft University of Technology.
- [69] Reinshaw. *Raman spectroscopy explained*. English. Sept. 2018.

- [70] Tim Deschaines, Joe Hodkiewicz, and Pat Henson. *Characterization of Amorphous and Microcrystalline Silicon using Raman Spectroscopy*. Thermo Fisher Scientific. URL: <https://assets.thermofisher.com/TFS-Assets/CAD/Application-Notes/D16998~.pdf>.
- [71] C. Smit et al. "Determining the material structure of microcrystalline silicon from Raman spectra". In: *Journal of Applied Physics* 94.5 (2003), pp. 3582–3588. DOI: 10.1063/1.1596364.
- [72] J. Krc and M. Topic. *Optical Modeling and Simulation of Thin-Film Photovoltaic Devices*. CRC Press, 2016. ISBN: 9781439818503.
- [73] Miro Zeman et al. *Advanced Semiconductor Analysis Manual*. English. Version 6.0. Delft University of Technology. Mar. 12, 2013.
- [74] Ruud EI Schropp and Miro Zeman. *Amorphous and microcrystalline silicon solar cells: modeling, materials and device technology*. Vol. 8. Kluwer Academic, 1998.
- [75] Kaining Ding et al. "Characterization and simulation of a-Si:H/uc-Si:H tandem solar cells". In: *Solar Energy Materials and Solar Cells* 95.12 (2011), pp. 3318–3327. ISSN: 0927-0248. DOI: <https://doi.org/10.1016/j.solmat.2011.07.023>.
- [76] Hairen Tan et al. "Highly transparent modulated surface textured front electrodes for high-efficiency multijunction thin-film silicon solar cells". In: *Progress in Photovoltaics: Research and Applications* 23.8 (2015), pp. 949–963. DOI: 10.1002/pip.2639.
- [77] K. Jäger et al. "A scattering model for nano-textured interfaces and its application in opto-electrical simulations of thin-film silicon solar cells". In: *Journal of Applied Physics* 111.8 (2012), p. 083108. DOI: 10.1063/1.4704372.
- [78] Fai Tong Si, Olindo Isabella, and Miro Zeman. "Artifact Interpretation of Spectral Response Measurements on Two-Terminal Multijunction Solar Cells". In: *Advanced Energy Materials* 7.6 (2017), p. 1601930. DOI: 10.1002/aenm.201601930.
- [79] P. Babal. "Doped nanocrystalline silicon oxide for use as (intermediate) reflecting layers in thin-film silicon solar cells". PhD thesis. Delft, The Netherlands: Delft University of Technology, Oct. 2014.
- [80] T de Vrijer. "Stability and Performance of Doped Silicon Oxide Layers for Use in Thin Film Silicon Solar Cells". MSc Thesis. Delft, The Netherlands: Delft University of Technology, Nov. 2015.
- [81] S. Nawaratne. "Nanocrystalline Silicon Solar Cells on Flexible Al Substrates". MSc Thesis. Delft, The Netherlands: Delft University of Technology, May 2020.